Universidad Industrial de Santander
Escuela de Física

Doctoral Dissertation

Multifunctional Properties Induced by Chirality in Crystalline Materials

by

Daniel David Torres Amaris MSc.

Advisor: **Ilia Davidovich Mikhailov PhD.**
Co-Advisor: **Andrés C. García C. PhD**
Doctorado en Física

Bucaramanga, Colombia
October 2023

Abstract

In condensed matter and materials sciences, a compound in which multiple and coupled physical properties coexist is known as multifunctional material. Much attention has been dedicated to such compounds due to the possibility of precisely controlling one property by interacting with another that they pose. Therefore, such materials integrating and coupling two, or more, properties related to ferroelectricity, magnetism, spin-control, and optical response, among others, are potential candidates for modern applications. Some areas where multifunctional materials have the biggest impact are energy harvesting, transmission, and storage devices. An important area that is actively investigated is related to efficiency improvement and device size reduction, along with reducing their impact on the environment. For example, light control devices capable of spin-control, based on Ferroelectric Rashba Semiconductors (FERSC), are being actively investigated due to their potential on spintronics and spin-orbitronics.

The symmetries of the system, as well as their electronic structure, are key to the development of physical properties in materials. More precisely, the absence of certain symmetries allows for certain properties; for example, ferroelectricity is allowed by breaking Inversion Symmetry (IS), while breaking of Time-Reversal Symmetry (TRS) is the source of ferromagnetism. Furthermore, chiral structures with linear dispersion, known as Weyl nodes, are allowed within the electronic band structure whenever one of these symmetries is broken. Such structures are solutions of the Weyl equation and resemble the massless chiral Weyl quasiparticles. BiSb and TaAs are examples of crystals where Weyl fermions are achieved by breaking the IS in a system with strong spin-orbit coupling. On the other hand, noncollinear magnetic orderings related to TRS breaking in antiferromagnets, such as $YbMnBi_2$, can also trigger the existence of Weyl nodes. Notably, breaking IS and TRS simultaneously permits, along with the Weyl nodes, a multiferroic/magnetoelectric behavior where ferroelectric and magnetic properties coexist. Thus, breaking IS, TRS, or both sets the required conditions for the existence of Weyl fermions and useful physical properties.

Besides existing in the Weyl nodes, chirality is observed in several ambits. The chiral asymmetry is found from subatomic particles to galaxies, passing through molecules, crystals, and everyday objects such as shoes; Chiral objects are recognized by the impossibility of superimposing them on their mirror image. Chiral molecules (enantiomers) show different manifestations on properties like their flavor, odor, drug effectiveness, and drug safety, among others, depending on their handedness. Another example of chirality is observed in noncollinear antiferromagnets, which can be scalar or vectorial for non-coplanar and coplanar orderings. Moreover, there are crystals with chiral symmetry space groups, such as the chiral Telluride crystals, which crystalize in right and left-handed chiral symmetry groups, each displaying a characteristic spin structure. In such a case, the chirality is strongly entangled with the electronic and ionic structure, resulting in unique and interesting properties such as the anomalous Hall conductivity, the photogalvanic effect, the anomalous Nernst effect, giant magnetoresistance, and superconductivity, among others; precise control of polarization and light propagation in the enantioselective chiral matter and chiral light interaction has been demonstrated in weakly interacting randomly oriented magnetic enantiomers. Thus, chiral symmetry conditions appear as an attractive candidate to be the key to unlocking and discovering new physical properties in solid-state systems.

This work concerned the effect of chirality in two different scenarios: first, in chiral noncollinear antiferromagnets, and second, in crystals with chiral space groups. In the first part, the interplay between the magnetism and chirality was studied in antiferromagnetic manganese-based nitride antiperovskites, Mn_3BN (with B a transition metal). Because of the triangular frustrated magnetic ordering over their kagome lattice formed by the Mn atoms along the (111)-plane, these compounds were the ideal platform for studying chirality and magnetism. In this case, vector chirality is induced by the noncollinear magnetic configuration, and the spin-orbit coupling is enhanced by the transition metal B. The data obtained after the successive substitutions B = Ni, Pd, Pt suggested a dependence of the anomalous Hall conductivity on the spin-orbit coupling. The phonon dispersion of Mn_3NiN indicated a sensitivity of the

compound to the volume of the structure. Thus, highlighting compression and tension strain deformations as a control mechanism over the physical properties present in the compound. The anomalous Hall conductivity, characterized as a function of the strain in Mn_3NiN, gave a nonlinear and nonmonotonic relation. Moreover, in the short range deformations, an improvement of the anomalous Hall conductivity was found with compression, while a rapid reduction of this transport property occurred under tensile strain. Finally, the anomalous Hall conductivity was found to arise from the Berry curvature in the (111)-plane. The second part consisted of the search for a chiral space group crystal with magnetism. During this phase, the ternary chiral compound $LaBPt_2$ was found to become ferromagnetic under the substitution of the lanthanum site for the magnetic lanthanide neodymium, giving $NdBPt_2$ as a result. The results indicated a strong dominance of the magnetism on the anomalous Hall conductivity, almost neglecting the effect of the chirality.

Resumen

En física de la materia condensada y ciencia de los materiales, un compuesto en el que coexisten múltiples propiedades físicas acopladas se conoce como un material multifuncional. Este tipo de compuestos ha llamado mucho la atención debido a la posibilidad que plantean de controlar con precisión una propiedad mediante la interacción con otra. Por lo tanto, dichos materiales que integran y acoplan dos o más propiedades relacionadas con la ferroelectricidad, el magnetismo, el control de espín y la respuesta óptica, entre otras, son candidatos potenciales para aplicaciones modernas. Algunas de las áreas donde los materiales multifuncionales tienen el mayor impacto son los dispositivos de recolección, transmisión y almacenamiento de energía. Un área importante que se investiga activamente está relacionada con la mejora de la eficiencia y la reducción del tamaño de dispositivos electrónicos, junto con la reducción de su impacto en el medio ambiente. Por ejemplo, los dispositivos de control de luz capaces de control de espín, basados en semiconductores ferroeléctricos Rashba (FERSC), se están investigando activamente debido a su potencial en espintrónica y espín-orbitrónica.

Las simetrías del sistema, así como su estructura electrónica, son claves para el desarrollo de las propiedades físicas de los materiales. Más precisamente, la ausencia de ciertas simetrías permite ciertas propiedades; por ejemplo, la ferroelectricidad se permite al romper la simetría de inversión (IS, por sus siglas en inglés), mientras que la ruptura de la simetría de inversión temporal (TRS, por sus siglas en inglés) es la fuente del ferromagnetismo. Además, siempre que se rompa una de estas simetrías se permiten estructuras quirales, conocidas como nodos de Weyl, dentro de la estructura de bandas electrónicas. Tales estructuras son soluciones de la ecuación de Weyl y se asemejan a las cuasipartículas quirales sin masa de Weyl. Los compuestos BiSb y TaAs son ejemplos de cristales en los que se obtienen fermiones de Weyl al romper el IS en un sistema con un fuerte acoplamiento espín-órbita. Por otro lado, los ordenamientos magnéticos no colineales relacionados con la ruptura de TRS en antiferromagnetos, como $YbMnBi_2$, también pueden desencadenar la existencia de nodos de Weyl. En particular, romper IS

y TRS simultáneamente permite, junto con los nodos de Weyl, un comportamiento multiferroico/magnetoeléctrico donde coexisten propiedades ferroeléctricas y magnéticas. Por lo tanto, romper IS, TRS o ambos establece las condiciones requeridas para la existencia de fermiones de Weyl y propiedades físicas útiles.

Además de existir en los nodos de Weyl, la quiralidad se observa en varios ámbitos. La asimetría quiral se encuentra desde partículas subatómicas hasta galaxias, pasando por moléculas, cristales y objetos cotidianos como zapatos. Una forma de reconocer objetos quirales es mediante la imposibilidad de superponerlos en su imagen especular. Un ejemplo del efecto de quiralidad se observa en las moléculas quirales (enantiómeros), que muestran diferentes manifestaciones en propiedades como su sabor, olor, efectividad y seguridad de los medicamentos, entre otras, dependiendo de su lateralidad. Otro ejemplo de quiralidad se observa en antiferromagnetos no colineales, cuya quiralidad puede ser escalar o vectorial, dependiendo de la naturaleza coplanar o no coplanar de los momentos magnéticos que estos presenten. Adicionalmente, existen cristales con grupos espaciales de simetría quiral, como los cristales quirales de teluro puro, que cristalizan en grupos de simetría quiral a derecha e izquierda; Cada uno de los cuales muestra una estructura de espín característica. En tal caso, la quiralidad está fuertemente entrelazada con la estructura electrónica e iónica, dando como resultado propiedades únicas e interesantes como la conductividad anómala de Hall, el efecto fotogalvánico, el efecto anómalo de Nernst, la magnetorresistencia gigante y la superconductividad, entre otras. Se ha demostrado un control preciso de la polarización y la propagación de la luz en la materia quiral enantioselectiva y la interacción de la luz quiral en enantiómeros magnéticos orientados aleatoriamente débilmente interactúantes. Por lo tanto, las condiciones de simetría quiral aparecen como un candidato atractivo para ser la clave para desbloquear y descubrir nuevas propiedades físicas en los sistemas de estado sólido.

Este trabajo se concentra en el efecto de la quiralidad en dos escenarios diferentes: primero, en antiferromagnetos quirales no colineales y segundo, en cristales con grupo espacial quiral. En la primera parte, se estudió la interacción entre el magnetismo

y la quiralidad en antiperovskitas antiferromagneticas no colineales a base de manganeso y nitruro, Mn_3BN (con B un metal de transición). Debido al ordenamiento magnético triangular frustrado sobre su red de kagome formada por los átomos de Mn a lo largo del plano (111), estos compuestos son la plataforma ideal para estudiar el magnetismo y la quiralidad. En este caso, la quiralidad vectorial es inducida por la configuración magnética no colineal, y el acoplamiento espín-órbita es mejorado por el metal de transición B. Los datos obtenidos tras las sustituciones sucesivas B = Ni, Pd, Pt sugirieron una dependencia entre la conductividad anómala de Hall y el acoplamiento espín-órbita. Adicionalmente, resaltaron la importancia de un correcto modelado de las correlaciones electrónicas de la mano de la propiedades estructurales. La dispersión de fonones de Mn_3NiN indicó una sensibilidad del compuesto al volumen de la estructura. Señalando así las deformaciones de compresión y tensión como mecanismo de control sobre las propiedades físicas presentes en este compuesto. La caracterización de la conductividad anómala de Hall en función de la deformación en Mn_3NiN, dio como resultado una relación no lineal y no monótona. Adicionalmente, se encontró una mejora de la conductividad anómala de Hall con la compresión, mientras que se produjo una rápida reducción de esta propiedad de transporte bajo tensión de tracción; lo anterior, en el rango de pequeñas deformaciones. Finalmente, se concluyó que la conductividad anómala de Hall surge de la curvatura de Berry en el plano (111). La segunda parte consistió en la búsqueda de un cristal de grupo espacial quiral con magnetismo. Durante esta fase, se encontró el compuesto ternario $LaBPt_2$, el cual se vuelve ferromagnético al sustituir el sitio de lantano por el lantánido magnético neodimio, dando como resultado $NdBPt_2$. Los resultados indicaron un fuerte dominio del magnetismo quiral sobre la conductividad anómala de Hall, mientras que el efecto de la quiralidad cristalina mostró poca inferencia en dicha propiedad.

Para:

Cinthia

Acknowledgement

It has been a very long journey from my first steps into physics as a young boy in Santa Marta, Colombia. I remember trying to understand the mysterious language of quantum mechanics from the notes of my brothers Emanuel and Rafael; back then, it looked so inexpugnable. Little I knew about the adventure awaiting me on the path to achieving the dream of becoming a scientist. Now, stomping on the last steps of my formal education and prompting into a more individual path, I find myself in the urge to acknowledge all the support that forever will make me feel in debt.

I want to especially thank my wife, Cinthia, whose invaluable support fueled this Ph.D. Without her patience and kind words, I would perhaps have surrendered. She is the best listener of all my past, present, and future adventures, theories, and discoveries.

I want to thank my kids for always bringing me joy, no matter the hurry of the moment. They helped me to see the bright side of life at all times.

To my parents, Olga and Rafael, I can't thank you enough. For allowing me to prove myself no being wrong. For having the most inexhaustible patience and resilience, even when everything I did seemed unfruitful.

I want to thank my brothers, Rafael and Edmanuel for showing me this amazing world called physics.

I want to thank my advisor, Andrés García at Universidad Industrial de Santander in Bucaramanga, Colombia, for introducing me to density functional theory and topological properties. During this time, I have learned more than I have ever thought I could.

I want to thank Professor Aldo Romero and his group at West Virginia University in the USA for their immensely helpful comments and suggestions throughout the research

work. Also, thanks for the chiral compounds database that you kindly provided.

I want to thank Professor Rafael González at Universidad del Norte in Barranquilla, Colombia. His support on the anomalous hall transport properties calculations was lifesaving.

I want to thank Professor Eric Bousquet at Université de Liège in Belgium, for his words of wisdom during his visit here in Colombia.

To GridUIS-2 experimental testbed of the Universidad Industrial de Santander (SC3-UIS) High Performance and Scientific Computing Centre. Where I did my first DFT calculations.

To the XSEDE complex and the Texas Advanced Computing Center (TACC) at The University of Texas at Austin. Where I performed most of my hard work in atomistic modeling and calculations in the STAMPEDE2 Bridges-2 supercomputers.

To the computational support extended to us by Laboratorio de Supercomputo del Sureste (LNS), Benemérita Universidad Autónoma de Puebla, BUAP, for performing heavy theoretical calculations.

To grant No. 2811: "Diseño de nuevos dispositivos de corriente de espín-polarizada controlada por campos magnéticos y eléctricos externos basados en las propiedades magnéticas y electrónicas de nuevos materiales 2D del tipo CrX3 (X = Cl, Br, I)." supported by Estampilla ProUIS.

To grant No. 2677: "Quiralidad y Ordenamiento Magnético en Sistemas Cristalinos: Estudio Teórico desde Primeros Principios" supported by the VIE – UIS.

The work by A.H.R. was supported by the grant DE-SC0021375 funded by the U.S. Department of Energy, Office of Science.

Contents

List of Figures

List of Tables

Abbreviations

List of Acronyms

DFT	Density functional theory
LDA	Local density approximation
GGA	Generalized gradient approximation
PBE	Perdew-Burke-Ernzerhof
SCAN	Strongly constrained and appropriately normed semilocal functional
SG	Space group
IS	Inversion symmetry
TRS	Time-reversal symmetry
FE	Ferroelectric
FM	Ferromagnetic
AFM	Antiferromagnetic
STA	stacked triangular antiferromagnets
MWS	Magnetic Weyl Semimetals
DM	Dzyaloshinskii–Moriya
BC	Berry curvature
AHC	Anomalous Hall effect
ANC	Anomalous Nernst effect

SOC	Spin-orbit coupling
SOT	Spin orbit torque
MLWFs	Maximally localized Wannier functions
RMS	Root mean square
FERSC	Ferroelectricity and spin-control in ferroelectric Rashba semiconductor
ARPES	Angle-resolved photoemission spectroscopy
CD	Circular dichroism

List of Symbols

$\mathcal{T}$	Time-reversal symmetry
$\mathcal{M}$	Mirror symmetry
Ω_{111}	Berry curvature in the 111 plane
σ^{AHC}	Anomalous Hall conductivity
η	strain in the crystal

Chapter 1

Introduction

Solid-state systems able to hold multiple functionalities such as the ferroelectric (FE), magnetic, and optical activity behavior are potential candidates for next-generation technological applications [1, 2, 3, 4, 5, 6, 7, 8, 9, 10]. Certain topological features are common to these functionalities, which in turn induce topological functionalities such as the anomalous Hall conductivity (AHC) [11, 12, 13] and the Berry curvature (BC) [14]; currently the source of much research work and scientific discussion in the field of solid-state physics and materials design. Because the topology of a system is rooted in its symmetries and asymmetries, the topological properties necessarily arise from them. In crystals, symmetry results from the way ions and electrons organize in the structure, which determines the phenomena allowed; chiral solid-state quasiparticles, known as Weyl nodes, can be observed in crystals with breaking of inversion symmetry (IS) or time-reversal symmetry (TRS) [15, 16]. Furthermore, besides the Weyl nodes, the lack of IS allows a FE behavior [17], while the breaking of TRS, triggers the AHC along with the chiral quasiparticles [18]. Moreover, when both IS and TRS are broken, multifunctional behavior is observed [19, 20, 21]. Therefore chirality is expected to play a key role in bounding the electronic and structural properties to the topological phenomena. Many objects display the property of chiral asymmetry, making them not superimposable over their mirror image. Gloves and shoes are good examples of chiral objects in our daily life, however, chirality is found in subatomic particles and

galaxies as well. In chemistry, chiral molecules are known as enantiomers [22], in which a chiral center is bounded to four different groups; each enantiomer has specific and different chemical and physical properties and technological applications. The chiral asymmetry is also present in the case of crystals, derivating a crystal with a given formula into pairs of left and right enantiomeric possibilities [1]. Thus, as in the case of molecules, showing different physical properties. The lack of mirror symmetry of the chiral crystal makes them naturally IS broken, which in turn allows the existence of Weyl nodes. An example of such are telluride crystals, which crystallize in right-handed and left-handed enantiomeric forms [23], each displaying inwards and outwards radial spin textures in momentum space depending on the handedness of the structure. Furthermore, the magnetic sublattice of a crystal can have a defined chirality. Noncollinear frustrated magnetic systems [24] are an example of chiral magnetism [25], where topological properties and chiral structures can be observed [26].

Antiperovskites, A_3BX [27], present the perfect scenario to study the entanglement of the chiral magnetic orderings to many functional properties [1, 26, 28, 29, 30, 31, 32, 33, 34, 35, 36, 37, 38]. The magnetic frustration present in the A_3 triangular coordination gives rise to chiral asymmetry and other interesting properties in this family of compounds; the anomalous Hall effect [39, 40], negative thermal expansion [41], giant piezomagnetism [42], magnetic frustration [43, 44], are good examples.

Therefore, aiming to understand the role of chirality over physical phenomena, we have established two goals in this thesis. The first goal attains to determine the importance of chiral magnetic orderings in noncollinear materials among the A_3BX family of antiperovskites, and more precisely, the manganese nitride members Mn_3BN where the electronic and ionic structure couple to the anomalous Hall conductivity. The second goal is to characterize magnetic and nonmagnetic crystals with chiral space groups, and there we intend to differentiate the contribution of the chirality and that of the magnetism. Particularly, the ternary compounds $LaBPt_2$ and $NdBPt_2$ will be characterized and compared in this part. All the mentioned characterization performed

[1] The same formula unit could crystallize in more than one enantiomeric pair as is the case.

in Density Functional Theory (DFT) calculations through the VASP (*i.e.* Vienna Ab-initio Simulation Package) code [45, 46] to characterize and study the properties of chiral crystals both from the electronic structure and the space group (SG) Symmetry. Electronic density, band structure, phonons, Berry curvature, and anomalous Hall effect, are some of the properties to calculate and the possible entanglement between them.

Chapter 2

Theoretical and Computational Background

The confluence of multiple physical properties in a single material has been the goal of many research works in the last decades [2, 6, 7, 8, 9, 47, 48, 49]. Multifunctional materials combine ferroelectric and magnetic behavior in multiferroics, and/or magnetoelectrics [1, 2], ferroelectricity and spin-control in ferroelectric Rashba semiconductor (FERSC) devices [3, 4], optical and magnetic ordering in magneto-optical compounds[5] and more. Among the most exciting physical properties currently investigated in the field of solid state physics and materials design, the topological properties such as the Anomalous Hall conductivity [11, 12, 13] and the Berry curvature [14] are in the center of the discussion. Because the connection that the crystallographic symmetry holds to the electronic structure imposes a well-defined topology, such properties are expected to find a source and explanation. Interestingly, it is not the present symmetries but the absent ones which ignite a given property. Particularly, the breaking of inversion symmetry (IS) in crystals can give rise to ferroelectric (FE) behavior. In contrast, time-reversal symmetry (TRS) breaking is the key ingredient to magnetic ordering. Such scenarios can be exemplified by BiSb [17] where Weyl nodes result from IS symmetry breaking and noncolinear antiferromagnets [18] such as Mn_3PdN where the broken

TRS is the source of the solid-state chiral quasiparticles. In the case of systems with both IS and TRS broken, the multiferroic/multifunctional behavior is observed along with the chiral quasiparticles. The presence of Weyl nodes can be confirmed by angle-resolved photoemission spectroscopy (ARPES) [20], X-ray scattering [16], and neutron scattering [21] among other techniques.

Chiral phenomena such as noncollinear magnetism, Weyl nodes, and certain crystallographic space groups are often accompanied by topological phenomena in crystals, and molecules [10]. Therefore a link between the electronic and structural properties to such interesting topological properties is expected to relay up to a given grade on the chirality. Chiral asymmetry is observed in many areas of science; even several objects in our surroundings, such as gloves, shoes, and wristwatches, are chiral. Despite having a very similar shape, chiral objects such as human hands can not be perfectly superimposed on each other. Thus, the chirality, often regarded as a handedness, can be assimilated as the lack of mirror symmetry. In physics, chirality is a fundamental property of some subatomic particles, galaxies, and quasiparticles, one that lies at the same level as the charge, mass, and spin. Remarkably, only left-handed particles can interact via weak interaction with right-handed antiparticles. In chemistry, there is a subgroup of the organic molecules that ostent the property of chirality; such molecules are known as enantiomers [22]. Two enantiomers with the same chemical formula, show different chemical and physical properties with specific medical and technological applications. Apart from particles and molecules, some crystals can also be chiral; the arrangement of their electronic and ionic structure and the possible magnetic ordering of that configuration imposes the chiral asymmetry condition on the system. Frustrated magnetic systems [24] are an example of noncollinear spin structures where chirality plays an important role in the magnetic ordering [25], ultimately affecting the physical properties of the system. Another case of chirality in crystals is observed in the pure chiral telluride crystals, which crystallize in the $P3_121$ (152, right-handed) and $P3_2$ 21 (154, left-handed) space groups [23]. Notably, chiral Te crystals display radial spin textures in momentum space whose orientation depends on chirality.

Another field where chirality plays a main role is related to the light-matter interaction [10], where precise control of the electric polarization can be performed by means of chiral light. The chiral matter can only absorb light with a polarization of the same chirality. Therefore, enantioselective synthesis and characterization can be performed under the adequate condition. Thus, chirality is a very useful property, with still much room for exploration and understanding of its implications.

2.1 Generalities of chirality

Chirality, derived from the Greek word *cheir* which means *a hand*, is a property exhibited by many familiar objects in our surroundings and nature going from fundamental particles [50] to galaxies [51]. An object is called chiral when it cannot be superimposed on its mirror image object by applying translation and rotation symmetry operations; in other words, a chiral object is prevented from having mirror symmetry. In this sense, a chiral object can only be transformed into its counterpart by destroying it into its fundamental blocks and constructing it again to make it superimposable on its mirror image. Hands and gloves are the most recognizable chiral objects. Still, the chiral asymmetry is also present in many more objects of daily use, such as cars, musical instruments, and shoes also display chirality symmetry operation. Besides the macroscopic world objects, the definition of chirality also permeates the microscopic world. Objects like molecules (called enantiomers), atoms, and even fundamental particles can display a chiral behavior. Enantiomers, for example, share the same chemical formula, but a different chirality as is the case of 1Bromo-1Fluoroethane which comes in a clockwise *(R) 1Bromo-1Fluoroethane* and counterclockwise *(S) 1Bromo-1Fluoroethane* configurations (see Figure 2.1). Louis Pasteur first noticed chirality in crystals in 1848, who was studying the optical properties, observed previously by Jean Baptiste Biot in 1832, on the optically active *tartaric acid* with chemical formula $C_4H_6O_6$ and the optically inactive *racemic acid* [52, 53]. Pasteur later discovered that racemic acid was composed by an equal mixture of two enantiomers of tartaric acid, one of them with

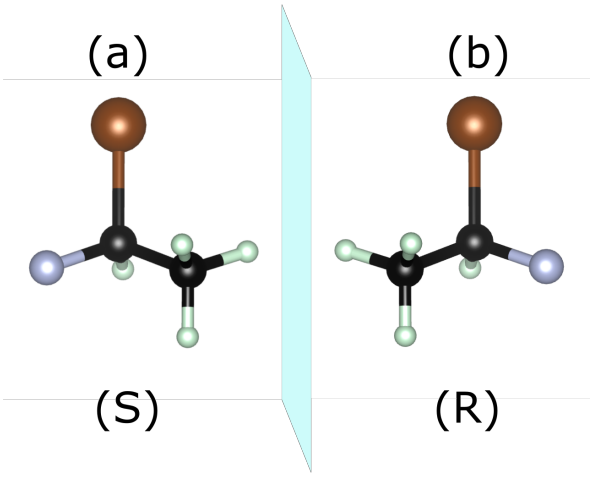

Figure 2.1: *Enantiomers of 1Bromo-1Fluoroethane. (a) Left-, and (b) Right-chiral configurations.*

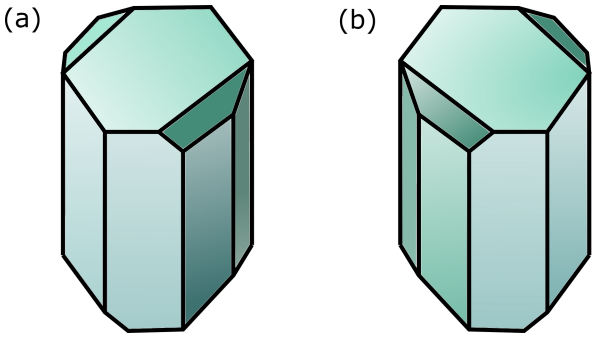

Figure 2.2: *Enantiopure crystals of tartaric acid. A Right-chiral crystal of tartaric acid is shown in part (a), and its enantiomer, left-chiral, is shown in part (b).*

a *dextrorotatory* (counterclockwise) and the other one with the opposed, *levorotatory* (clockwise) rotational (see figure 2.2). The latter was measured on experiments of transmittance of linearly polarized light [54, 55] on the enantiopure (chiral) crystals as well as the equal mixture of them. Nowadays, an equal mixture of two enantiomers is called a racemic mixture. All of them are known to be optically inactive due to the equal rotatory power in both directions, which cancel out each other. There are two symmetry operations concerning chirality in crystals, the glade plane, and the screw axis. The glide plane, regarded as the homonymous operation to the mirror plane, is the combination of a reflection and a translation of one-half the unit cell with respect

to a plane of symmetry. The screw axis is an axis of rotation and translation, designated by n_m (a rotation of $360/n$ and a translation of a fraction m/n of the unit cell). As in the case of molecules and other chiral objects, the glide plane is not allowed in chiral crystals. The screw axis, on the other hand, is mandatory, being the most recognizable characteristic of a chiral crystal. Notably, a chiral crystal can be composed out of chiral molecules and achiral ones, inheriting the symmetries of the constituent molecules on top of the symmetry of the space group, which can be chiral or not. This work will concentrate on chiral crystals with chiral SG. Thus, crystals without roto-inversion symmetries in its lattice and SG have a well defined handedness and are called chiral crystals [56]. Examples of chiral crystalline structures with achiral SG are $AlPS_4$ [56] and Ag_2Se [57], both of them, orthorhombic crystalline structures, but the first have the SG symmetry 16 ($P222$) and the later holds the SG symmetry 19 ($P2_12_12_1$). As expected, the mentioned crystalline structures have SG symmetries lacking roto-inversion. On the other hand, the chiral SG crystal of quartz, a SiO_2-based crystal composed out of SiO_4 tetrahedrons arranged in a double-helix belongs to the chiral SG $P3_221$; its structure resembles one of the most famous chiral structures, the Deoxyribonucleic acid (DNA). Quartz crystals constituents are achiral, but their arrangement in the space belongs to a chiral SG; in this case, the chirality arises from the SG and not from the building block [58].

Finally, it is worth mentioning that while it is possible to obtain the crystal structure via X-Ray diffraction, it is impossible to discern its chirality, a measurement that must be carried out through circular dichroism (CD). Another way to reveal chirality in a sample is by means of ionizing circularly-polarized light, a method that produces a current of photo-electrons whose direction is enantiosensitive[10].

2.2 Chirality in solid-state systems

As have been already discussed, chirality is present in crystals. However, there are two different sources of this property in crystals; one arises from magnetism, and the other

does it from the crystalline structure itself. The chirality of the crystalline structure will be treated in more detail later in the text. Magnetism is a complex property that can be found in many different configurations. The magnetic ordering is maintained by means of the exchange interaction, and its structure can exhibit a complexity beyond the collinear structures known as ferromagnetic, antiferromagnetic, and ferrimagnetic. In fact, the boundary between two antiparallel magnetic domains is composed of magnetic moments pointing in a wide variety of angles other than 0 and π. In this regard, the antiperovskite carbide family of compounds X_3BC (where C is carbon) have shown interesting physical properties related to their magnetic ordering, such as thermal expansion, giant magnetoresistance, topological electronic states, and superconductivity among others [59]. Particularly, the cubic perovskite structure Mn_3ZnC, studied with neutron diffraction in the 1950s [60, 61, 43] due to its interesting first and second order phase transitions induced by cooling has been getting more attention recently due to the possibility of Weyl nodes [59]. The Mn_3ZnC goes from paramagnetic at high temperature to ferromagnetic below the Curie temperature $T_C \approx 420K$ while keeping its cubic structure. For temperatures below the Néel temperature $T_N \approx 219K$, a first-order phase transition occurs, where the structure becomes tetragonal with a non-collinear ferrimagnetic ordering [60, 43, 62]. According to the work of Fruchart and Bertaut [43], the phase transitions are governed by the electronic structure around the metallic atom of Zinc, thus influencing the magnetic order-disorder transition temperature. Teicher *et al.*[59] invokes the connection between the Weyl nodal lines present in the cubic ferromagnetic phase and their destruction by the structural and magnetic ordering in the non-collinear ferrimagnetic tetragonal phase as an important factor in the magnetostructurally coupled materials. The strong coupling of the crystalline structure to the electronic structure is the source of many different behaviors associated with the disposition of magnetic moments; chiral behavior is one of them.

2.2.1 Chiral magnetic phases

The study of chirality from the electronic viewpoint is an active area of work, and there is much to figure out. Furthermore, the chirality from the magnetic ordering viewpoint is a feature of some solid-state compounds that allows a peculiar behavior. Crystals with a well-defined handedness in their spin structure can interact in a special manner with light and show unique charge transport phenomena. In some low symmetry multilayered crystals, more exactly metals lacking inversion symmetry, a homochiral (enantiopure) spin structure is allowed [63]. Chirality on the magnetic order of the spin structure has been observed in an atomic monolayer of Manganese deposited on a Tungsten substrate [64]. In fact, antiferromagnets in the presence of a strong external magnetic field aligned perpendicularly to the easy axis, often develop a chiral spin texture. Such conditions, induce a second-order phase transition, in which the spin structure goes from the antiferromagnetic ordering to the spin flop state, and finally becomes a spin spiral.

The explanation for this transition is found in the exchange interaction and, more precisely, the asymmetry Dzyaloshinskii–Moriya (DM) interaction which is a source of weak ferromagnetic behavior in an antiferromagnet that induces canting in the otherwise anti-parallel spins [65]. As such, the external magnetic field breaks the equilibrium between the symmetric exchange interaction and the asymmetric DM interaction. The transport phenomena of charge carriers with a defined spin and the control of such spin through the local spin structure are the main concern of spintronics. Thus the collective chiral behavior of the spin structure in the antiferromagnets can be a very relevant subject to the application in the area.

In Fig. 2.3, different lattices with different coordinations are shown for an antiferromagnetic configuration. In Fig. 2.3(a), the most simple case of a 1-dimensional antiferromagnet is shown; accommodating magnetic moments is a straightforward task. The case is the same for the 2-dimensional squared lattice shown in figure 2.3(b), where, each spin lies antiferromagnetically aligned with each neighbor. However, a

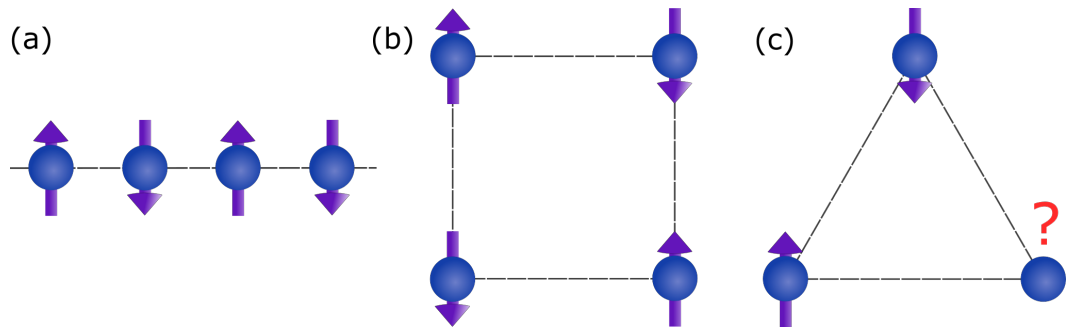

Figure 2.3: *(a) One Dimensional AFM lattice. (b) Square AFM lattice, and (c) triangular AFM lattice.*

2-dimensional triangular lattice, shown in Fig. 2.3(c), poses a challenging problem. In this case, because of a favored antiferromagnetic interaction among the first neighbors, there is no way to set the third spin antiferromagnetically with respect to the remaining spins, then the system gets frustrated. Here, the equilibrium between symmetric and asymmetric interactions can only be reached in a special orientation of the spins. Thus, frustration commands a noncollinear accommodation of all three spins to minimize the energy of the system.

Spin-frustrated structures, such as stacked triangular antiferromagnets (STA), can not have a trivial magnetic ordering such as 1-dimensional or square lattices (see Fig. 2.3). Frustration often results in noncollinear and/or noncoplanar magnetic ordering. In this case, the system acquires a higher degree of freedom which traduces in multiple chiral configurations with the same ground state level. In a noncollinear coplanar triangular antiferromagnetic structure, the lowest energy configuration that minimizes the spin interaction energy given by the Hamiltonian Eq. 2.1

$$\hat{H}_s = \sum_{i \neq j} J_{ij} \mathbf{S}_i \cdot \mathbf{S}_j, \tag{2.1}$$

is achieved when the spins are all making a 120° angle to each other. Degenerated magnetic ordering with minimal energy configuration possible in a frustrated triangular antiferromagnet can be seen in Fig. 2.4. Some configurations are right-handed, and others are left-handed. Examples of triangular frustrated antiferromagnets with all the

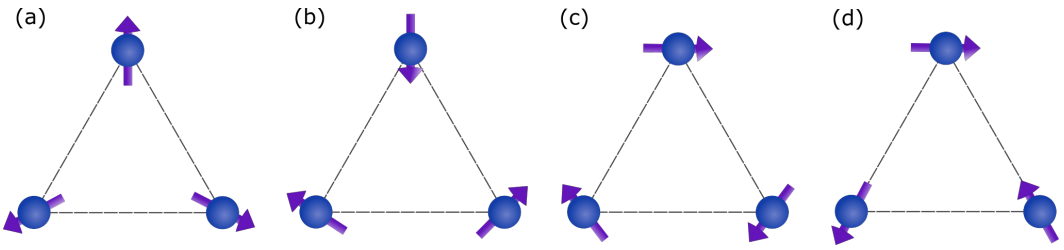

Figure 2.4: *Noncollinear coplanar antiferromagnetic triangular spin structure. Parts (a,b) show the right-chiral ordering. Parts (c,d) show the left-chiral configurations.*

spins in the XY plane are $CsMnBr_3$ and VBr_2. For this coplanar configuration a vector chirality can be defined in terms of the sum of the vector product of the spins

$$k = \frac{2}{3\sqrt{3}} \sum_{ij} [\vec{S}_i \times \vec{S}_j]_z, \tag{2.2}$$

where $\vec{S}_i$ is the spin. The presence of chirality in these systems favors a nontrivial behavior of the magnetic moments along with very interesting properties [25].

Apart from triangular stacked antiferromagnets, there are other chiral systems called Heisenberg spin glasses. Compounds such as CuMn, AgMn, and AuFe, that possess both, antiferromagnetic and ferromagnetic coupling due to frustration and randomness are expected to show a chiral magnetic ordering [66, 67]. Contrary to STA, the spins in these compounds are noncollinear and noncoplanar. Thus, the definition of chirality in the $i-th$ site along the axis μ is given as

$$\chi_\mu = \vec{S}_{i+\hat{\delta}} \cdot \vec{S}_i \times \vec{S}_{i-\hat{\delta}}, \tag{2.3}$$

where $\hat{\delta}$ is a unit vector in the direction of the μ axis. Chirality, defined this way is a pseudoscalar quantity that changes sign under a parity transformation. The kind of glassy behavior of the spin in this type of material is still an open question with no consensus. Chirality has been proposed as a candidate to explain the source of the observed magnetic ordering in Heisenberg spin glasses for a while [68], and it has been tested in modern research works [67, 66], still holding as a good prospect.

The fact that a not chiral crystalline structure can give rise to a chiral behavior from the spin structure point reveals a new path to further study the significance

of chirality and its repercussions on the physical properties of crystals. It is worth mentioning that this singular magnetic ordering is intimately related to the lack of inversion symmetry of the ionic structure, so the source of handedness in the spin structure is still connected to the crystalline structure and its symmetries. Chiral media can support new and unforeseen phenomena like strong magneto–chiral dichroism, which has been observed in systems where chirality and ferromagnetism coexist [69]. Various novel chirality-related properties are still to be found in magneto-chiral and chiral crystalline structures.

2.2.1.1 Kagome lattices

Geometrical frustration in solid-state systems grants access to higher degrees of freedom and, with them, an increase of the possible ground-state configurations. Interestingly, a wider view of the 111-plane in Mn_3BN antiperovskites shows a triangular frustrated structure, in which a very interesting lattice structure known as kagome lattice is revealed. Among the triangular frustrated 2-dimensional lattices, kagome lattices, named after the Japanese bamboo basket, which is a sixfold chiral structure, are systems of interest due to the phenomena they can hold [24]. Instead of sharing the edges, in this lattice, triangles share their vertices. In Fig. 2.5, you can see the kagome lattice present in the (111) plane of the Mn_3NiN antiperovkite. Thanks to the non-trivial magnetic ordering in such systems, remarkable phenomena such as quantum spin liquids [70], spin ice [24], magnon Hall effect [71], and magnetic Weyl semimetals [72] are permitted. Spin liquids are a result of the fluctuations of the spin $\frac{1}{2}$ lattice, induced by the frustration of the antiferromagnetic interaction that inhibits the formation of a preferred ordered state, the spins behave as a liquid at low temperatures, in which the correlations are high, but short-ranged [24]. In this case, spin can easily propagate even in the case of charge insulators [70]. Spin ice, which has been observed in holmium titanate $Ho_2Ti_2O_7$, is a behavior of the spin which resembles the behavior of hydrogen atoms in common water ice [24]. The magnon Hall effect consists of a transverse heat current when a temperature gradient is applied. Magnetic Weyl Semimetals

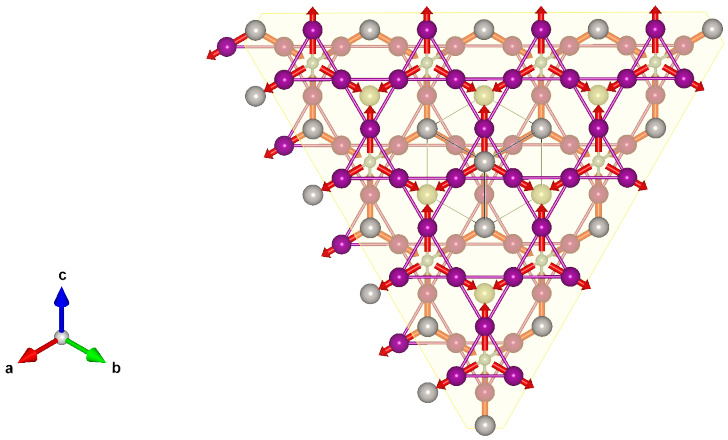

Figure 2.5: *View of the (111)-plane, highlighted in yellow, of the frustrated noncollinear antiperovskite Mn_3NiN where the kagome lattice can be observed (marked by the purple lines).*

(MWS) are crystalline 3D structures with broken TRS; in them, the formation of Weyl point and its corresponding surface Fermi arcs [72] are allowed. A prototype material with these properties is $Co_3Sn_2S_2$. This material is composed of stacked ferromagnetic kagome lattices [73] along the z-axis; this compound suffers a phase transition from PM to FM below T_c=175. The importance of MWS lies in the possibility of the interplay between chiral phenomena and magnetism, a relationship that may be crucial to unveil ways to interact and control the chiral fermions magnetically.

2.3 Chirality-derived physical properties

Chirality has shown a strong effect on the properties of advanced materials. For example, in ferroelectric compounds, *i.e.*, materials capable of electrical polarization switching as a function of an applied electric field, the effects of chiral phases have been explored[74] showing the possibility of electric control of bulk Rashba effect and the realization of topological insulator phases. Also, noncentrosymmetric three-dimensional topological insulators have been proven to have a Weyl semimetal phase at some point

during its phase transition to a normal insulator [75]. Materials such as $SnTe$, a centrosymmetric topological insulator at room temperature, display ferroelectricity due to the breaking of inversion symmetry present in a noncentrosymmetric phase at low temperatures, feature a clear interplay between ferroelectricity and chirality. The antiferromagnet $BiFeO_3$ is the most known room temperature multiferroic, in which, a ferroelectric chiral behavior has been demonstrated and tested by CD [76] close to $0K$. This kind of material opens the opportunity to gain further understanding of the chirality effect in crystalline systems where additionally, other degrees of freedom can be achieved. Then, more precise control on the properties entangled to Weyl or Dirac fermions is possible while profiting from their topological protection to make robust applications to spintronics[74].

Recently, a magnetic Weyl semimetal has been realized in the antiferromagnet $YbMnBi_2$, a compound with a locked perfect collinear spin structure above $T = 50K$. Below the mentioned temperature, the spins suffer a canting, and noncollinearity is established along with the consequence of breaking TRS. The calculated band structure of this material and its experimental measurements reveals the existence of Weyl states, and the noncollinearity of the magnetic moments was probed by means of magneto-optical microscopy[77]. This TRS-breaking Weyl semimetal is key to linking chirality and magnetism, and the mechanism that induces this behavior is still a matter of study. Strong magneto chiral dichroism has been found in an enantiopure chiral ferromagnet ($[N(CH_3)(n-C_3H_7)_2(s-C_4H_9)][MnCr(ox)_3]$ where (ox) is an oxalate, *e.g.*, $C_2O_4^{2-}$) [69, 78], this phenomena consists in a difference in the intensity of unpolarized light absorbed in the parallel and the antiparallel propagation with respect to an external field.

Superconductivity has been theoretically studied [79] and spotted in Weyl semimetals [80]. Materials such as WTe_2 and $MoTe_2$ are superconductors at $0.10K$. Still, they have an additional property called pressure-driven superconductivity[80], which makes them rise that temperature up to $8.2K$ when exposed to a pressure of $11.7GPa$. The effect of pressure is due to the structural phase transition that it induces, driving the

structure from a monoclinic to an orthorhombic configuration, and there, topology generates superconductivity.

Chirality, and therefore topology, evidently has a deep impact on the physical properties of materials. There is still a long way to travel to get a sufficient understanding of the interplay of chirality and physics. However, this is an exciting area with many phenomena waiting for an explanation and a vast richness of novel effects with potential applications to cutting-edge technology.

2.4 Topological phenomena

Topology is an area of mathematics that has permeates many other fields, such as physics, chemistry, biology, and quantum computing. In physics, and more precisely in solid-state physics, the theory of band topology has revolutionized our understanding of physical properties. Examples of such novelty are the semimetallic phases and the topological defects; the first are systems able to hold chiral single-point degeneracies known as Weyl nodes, and the second attempts to understand the effect of impurities on the topology of an otherwise perfect crystal. Given our interest in the anomalous transport phenomena in perfect crystals and the mechanisms driven by the topology enabling such behaviors, in what follows, Weyl crossings, Berry curvature, and the anomalous Hall effect will be the only subjects of discussion.

2.4.1 Weyl crossings

Solid-state systems can hold various quasiparticles such as Dirac, and Weyl points as well as the predicted and not yet confirmed Majorana fermions. Being both solutions to the Dirac equation, Dirac and Weyl points are related. In fact, a Dirac point, which is a band crossing of doubly degenerated electronic bands, can be dissolved into two Weyl points. Weyl point [1] are points where singly degenerated band crossings

[1] Also referred to as Weyl nodes

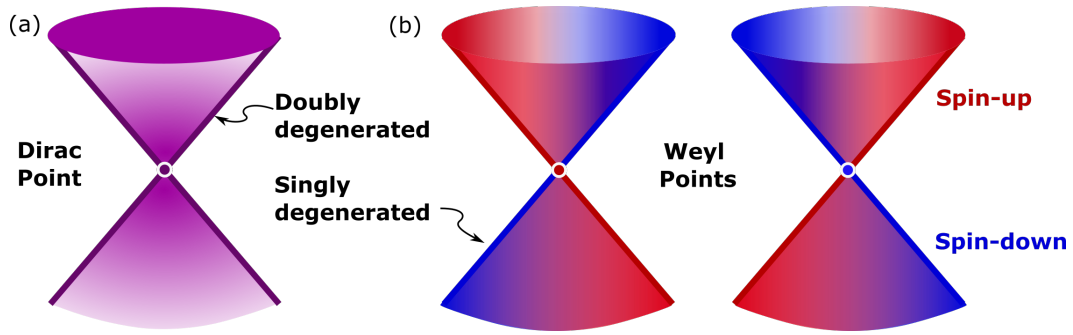

Figure 2.6: *(a) a Dirac point and (b) two Weyl points resulting from the dissolved Dirac point.*

occur. Therefore, for such structures to exist, a Dirac point must be separated into two Weyl points as shown in Fig. 2.6, either by relieving the band degeneracy by breaking of IS or TRS, or both of them. When TRS is broken, the Weyl nodes are separated in energy, while the breaking of IS separates them in the momentum space. Additionally, due to the degeneration relief, bands are now differentiated by spin; therefore, a spin inversion occurs at the Weyl node. Thus a spin-up band becomes a spin-down band after the node and vice-versa. Interestingly, Weyl nodes are protected by the nonsymmorphic symmetries of the system and, therefore, are protected by the topology. Hence its topological nature, which allows them to participate in anomalous transport phenomena.

Although Weyl nodes come in different fashions other than linear, in this work, we concentrate on linear dispersing Weyl nodes, principally, those arising from the TRS breaking in noncollinear antiperovskites.

2.4.2 Berry curvature

The Berry curvature is a gauge field associated with the Berry phase, a geometric phase [81] accumulated during an adiabatic process. This phase was thought to always vanish until the work of Berry [82], which explained the Aharonov-Bohm effect as a geometrical phase factor. According to the adiabatic theorem, the eigenstate of a slowly varying system, depending on a parameter $\lambda(t)$, can be expressed in terms of

the initial state $|n, \lambda\rangle$ through a dynamical phase as follows:

$$|\Psi_{n\lambda}(t)\rangle = e^{-\frac{i}{\hbar}\int_0^t dt' \epsilon_{n\lambda(t)}} |n, \lambda(t)\rangle. \tag{2.4}$$

On top of that, an additional phase depending on λ can be added without perturbing the Schrödinger equation, resulting in

$$|\Psi_{n\lambda}(t)\rangle = e^{i\gamma_n(t)} e^{-\frac{i}{\hbar}\int_0^t dt' \epsilon_{n\lambda(t)}} |n, \lambda(t)\rangle. \tag{2.5}$$

Substituting Eq. 2.5 in the time-dependent Schrödinger equation for a cyclic change such that $\lambda(T) = \lambda(0)$ the Berry phase is obtained as

$$\gamma_n(T) = i \oint_C d\lambda \langle n, \lambda(t)| \frac{\partial}{\partial \lambda} |n, \lambda(t)\rangle. \tag{2.6}$$

The integrand in Eq. 2.6 is known as the Berry connection

$$A_n(\lambda) = i\langle n, \lambda(t)| \frac{\partial}{\partial \lambda} |n, \lambda(t)\rangle. \tag{2.7}$$

The Berry connection behaves as a vector potential, and it is impossible to remove it by any gauge transformation. Therefore, in 3-dimensions, and in virtue of the Stokes theorem, the berry phase can be written as

$$\gamma_n(C) = \int_S d^2\mathbf{a} \cdot \nabla_\lambda \times A_n = \int_S d^2\mathbf{a} \cdot \Omega_n, \tag{2.8}$$

Where Ω_n is known as the Berry curvature, this topological field has a direct impact on the charge mobility, and it induces the same behavior in charge carriers as would a net magnetization in a ferromagnet. Thus, an antiferromagnet with a nonvanishing Berry curvature can hold an anomalous Hall effect, as observed in ferromagnets.

2.4.3 Anomalous Hall effect

The anomalous Hall effect, named after the Hall effect present in trivial conductors in the presence of an external magnetic field, received its name due to the high strength that it displays when compared to the Hall effect. However, the AHC was first discovered in magnetic materials with a net magnetization; the intrinsic magnetic field

deflects the charge carriers so that a current perpendicular to the electric field can be measured. Moreover, it was long thought that in magnetic materials with zero net magnetization, the AHC was absent. This idea changed along with confirming the Berry phase accumulation in cyclic adiabatic processes and the nonvanishing Berry curvature that it induces. Thus, an AHC can be outsourced from this topological field, and it can be calculated as the integral of the Berry curvature along the Brillouine zone [83]

$$\sigma_{\alpha\beta}^{AHC} = -\frac{e^2}{\hbar}\int_{BZ}\sum_{n}\frac{d^3\vec{k}}{(2\pi)^3}f_n(\vec{k})\Omega_{n,\alpha\beta}(\vec{k}), \tag{2.9}$$

Here, in Eq. 2.9, $f_n(\vec{k})$ is the Fermi-Dirac distribution and $\Omega_{n,\alpha\beta}(\vec{k})$ is the Berry curvature matrix of band n. Therefore, a non-zero AHC is observed as the result of each band contribution to the Berry curvature at the Fermi level. Thus, the Berry curvature acts as a momentum space magnetic field, inducing a charge carriers path deflection even in the absence of a net magnetization. The Γ_{4g} non-collinear antiferromagnetic phase of the Mn_3NiN antiperovskite is a good example of such scenario [84, 85, 40]. There, a net Berry curvature is present due to the symmetry conditions imposed by the magnetism. Recent studies have demonstrated the AHC in the collinear antiferromagnet MnTe in the absence of an external magnetic field [86] thanks to the anisotropy induced by Te atoms.

2.5 Basics of DFT

The vast majority of problems studied in condensed matter physics consist in a set of various atoms spatially extended; many nuclei and their corresponding electrons interact quantum mechanically with each other. The ground state configuration and its corresponding energy E is a parameter of significant importance and the starting point to study the behavior of a set of atoms. In this context, to obtain the ground state, which is a time-independent quantity, the Schrödinger equation $\hat{H}\Psi = E\Psi$ must be solved. Moreover, considering all the terms in the many body problem Hamiltonian,

H, we have:

$$\hat{H} = \hat{T}_e + \hat{T}_N + \hat{V}_{NN} + \hat{V}_{ee} + \hat{V}_{eN}, \tag{2.10}$$

where, $\hat{T}_e$ is the kinetic energy of the electrons, $\hat{T}_N$ is the kinetic energy of the nuclei, $\hat{V}_{NN}$ is the potential energy of the nucleus-nucleus interactions, $\hat{V}_{ee}$ is the potential energy of the electron-electron interactions, and $\hat{V}_{eN}$ is the potential energy due the electron-nucleus interactions. Imposing the adiabatic approximation, the equations of motion of the electrons and that of the nuclei decouples, allowing the dynamics of the electrons to be solved separately as if they were in the potential of fixed nuclei and then resolve the dynamics of the nuclei as if they were in the potential of the electrons (in their new positions) in each step of the time. Furthermore, the Born-Oppenheimer approximation, in which all correlations between the electrons and nuclei are removed, is applied. Thus, the only problem left to solve is the Schrödinger equation for the electrons in the potential of the nuclei. The adiabatic and Born-Oppenheimer approximations application is guaranteed thanks to the really slow motion of the nuclei, when compared to the electrons, allowing the latter to rapidly adapt to the changes in the position of the nuclei [87]. A complete description of a N electron system in the field of nuclei, after considering the Born-Oppenheimer and adiabatic approximations, is given by the Hamiltonian constituted as:

$$\hat{H} = \frac{\hbar^2}{2m_e} \sum_{i=1}^{N} \nabla_i^2 + \sum_{i=1}^{N} V(\mathbf{r}_i) + \sum_{i=1}^{N} \sum_{j<i} U(\mathbf{r}_i, \mathbf{r}_j). \tag{2.11}$$

The terms represent the electronic kinetic energy, the interaction energy between each electron and the nuclei potential, and the electron-electron potential energy of interaction, respectively. However, there is one more difficulty to sorting; the electronic quantum wavefunction is still a function of all electron coordinates

$$\Psi = \Psi(\mathbf{r}_1, \mathbf{r}_2, ..., \mathbf{r}_N). \tag{2.12}$$

To contextualize the massive undertaking this problem represents, let us consider a crystal composed of carbon atoms. Say we want to study a crystal of 100 atoms, the

number of electrons in this system is 1200, and its corresponding number of coordinates would be 3600. This small system can give us some understanding of the physics of the problem. Still, to be able to measure macroscopic quantities (as experimentally observed in the laboratory), the number of atoms of the system must approach the Avogadro constant $N_A = 6.02 \times 10^{23} atoms/mol$ where the real macroscopic behavior of the system happens. The number of coordinates grows overwhelmingly, and the solution to the many-body problem becomes virtually impossible. At this point, the density functional theory comes into the course, replacing the quantum wavefunction by the electronic density, computed as:

$$n(\mathbf{r}) = \int \cdots \int |\Psi(\mathbf{r}_1, \mathbf{r}_2, ..., \mathbf{r}_N)|^2 d\mathbf{r_1} d\mathbf{r_2} \cdots d\mathbf{r_N}. \tag{2.13}$$

The electronic density has the advantage of being a function of only three coordinates and contains the relevant statistical information of the system. In quantum mechanics, the exact position and momentum of a particle are not accessible, and even the classical concept of a path has no quantum analogous; plus, no single-particle experiment is reproducible two times in the same way. Only a statistical ensemble of a quantum system is truly reproducible. Moreover, because of the link between the energy of a system and its electron density distribution[2], and the univocal determination of the ground state energy E_0 as a functional of the ground state charge density $n_0(\mathbf{r})$ proven by Hohenberg and Kohn [88], the ground state wave function can be calculate as a functional of the ground state charge density:

$$\Psi_0 = \Psi[n_0(\mathbf{r})]. \tag{2.14}$$

Equations (2.13) and (2.14) are key in DFT. They tell us that it is indifferent working with the wavefunction or the electron density. Both representations of the problem are equally valid; in DFT, the three-coordinate problem for the density is solved first. Then the $3N$-coordinate wavefunction is recovered to further dig into the physics of the system.

[2]Which allows to establish a one to one relationship between the external potential and the ground state charge density.

Although the mentioned methodology is widely used in quantum chemistry, its application is still inadequate for crystals and needs further assumptions. The Kohn-Sham formalism requires a system describable by a wave function writable in terms of a single Slater determinant:

$$\Psi(\mathbf{r}_1, \mathbf{r}_2, \ldots, \mathbf{r}_N) = \frac{1}{\sqrt{N!}} \begin{vmatrix} \varphi_1(\mathbf{r}_1) & \varphi_2(\mathbf{r}_1) & \cdots & \varphi_N(\mathbf{r}_1) \\ \varphi_1(\mathbf{r}_2) & \varphi_2(\mathbf{r}_2) & \cdots & \varphi_N(\mathbf{r}_2) \\ \vdots & \vdots & \ddots & \vdots \\ \varphi_1(\mathbf{r}_N) & \varphi_2(\mathbf{r}_N) & \cdots & \varphi_N(\mathbf{r}_N) \end{vmatrix} \equiv |\varphi_1, \varphi_2, \cdots, \varphi_N\rangle \quad (2.15)$$

where the $\varphi_i(\mathbf{r})$ are unielectron wavefunctions. In DFT, within the Kohn-Sham scheme [89], the problem of interacting electrons and nuclei, initially represented by a wavefunction, is substituted by noninteracting electrons (Kohn-Sham orbitals) inside an external potential $v_s(\mathbf{r})$. Each orbital $\varphi_i(\mathbf{r})$ is solution of the one-electron Schrodinger equation

$$\left[-\frac{1}{2}\nabla^2 + v_s(\mathbf{r})\right] \varphi_i(\mathbf{r}) = \varepsilon_i \varphi_i(\mathbf{r}). \quad (2.16)$$

According to the Hohenberg-Kohn theorems [88], there is a one-to-one relation between the external potential and the electronic density. In the Kohn-Sham scheme [89], an initial guess of the charge density (*i.e.*, an estimation of the initial ionic and electronic density) induces an external potential $v_s(\mathbf{r})$ which is then used to obtain the set of unielectron wavefunctions by imposing the one electron Schrodinger equation (2.16) on them.

Now that all the necessary approximations are in place, the criteria to find the correct set $\{\varphi_i(\mathbf{r}_i)\}$ must be settled. At this stage, the ground state energy comes into play due to its important property of being the lowest possible energy achievable by the system. Thus, energy of the noninteracting system is written explicitly as:

$$\langle\Psi|\hat{H}|\Psi\rangle = \frac{\hbar^2}{2m_e}\int \nabla\Psi^\dagger \cdot \nabla\Psi d^3r + \frac{1}{2}\int \Psi^\dagger\Psi v(\mathbf{r}) d^3r + \frac{1}{2}\int\int \frac{\Psi^\dagger(\mathbf{r})\Psi(\mathbf{r})\Psi^\dagger(\mathbf{r}')\Psi(\mathbf{r}')}{|\mathbf{r}-\mathbf{r}'|} d^3r d^3r'. \quad (2.17)$$

Now, identifying the density $n(\mathbf{r}) = \Psi^\dagger\Psi$, the total energy of the ground state can be written as a functional of that density in the form

$$E_v[n] = T_s[n] + \int n(\mathbf{r})v(\mathbf{r})d^3r + \frac{1}{2}\int\int \frac{n(\mathbf{r})n(\mathbf{r}')}{|\mathbf{r}-\mathbf{r}'|}d^3r d^3r' + E_{xc}[n], \tag{2.18}$$

where the four terms are the kinetic energy, the interaction energy between the electrons and the external potential, the potential energy of the electron-electron interaction, and the exchange and correlation energy, respectively. The exchange and correlation energy is a correction needed due to the energy lost in the process of removing the electronic correlations and needs to be added by hand with the help of some knowledge of the system.

A new electron density and its corresponding energy are calculated in a self-consistent cycle until the energy is minimized, and only small changes in the energy and density are observed in further calculations. At this point, the density of the auxiliary noninteracting system corresponds to the electronic density of the real system.

Finally, when spin-polarized electronic density is considered, the wavefunction (2.15) depends on the position r_i and the spin s_i of each particle. Therefore, the density (2.13) must be changed into a two-function scheme, one function for the spin up ($\uparrow$) and the other for the spin down ($\downarrow$) density

$$\Psi^\uparrow\left[n^\uparrow(\mathbf{r})\right](\mathbf{r}_1, s_1, \ldots, \mathbf{r}_N, s_N) \tag{2.19}$$

$$\Psi^\downarrow\left[n^\downarrow(\mathbf{r})\right](\mathbf{r}_1, s_1, \ldots, \mathbf{r}_N, s_N). \tag{2.20}$$

Each equation will produce a value of energy that must be combined to get the total energy of the system. Additionally, when including the spin-orbit coupling, it is necessary to include the spinor in the electronic density and equations. In this case, the movement of an electron in a classical external field ($\phi_{ext}(\mathbf{r})$ and $\mathbf{A}_{ext}(\mathbf{r})$) is given by the relativistic Schrödinger equation[90]:

$$\hat{H}^D\psi(\mathbf{r},t) = \left[c\alpha\cdot\hat{\mathbf{p}} + \beta m_e c^2 + q_e(\phi_{ext}(\mathbf{r}) - \alpha\cdot\mathbf{A}_{ext}(\mathbf{r}))\right]\psi(\mathbf{r},t) = i\hbar\frac{\partial}{\partial t}\psi(\mathbf{r},t), \tag{2.21}$$

where the first term in the Hamiltonian is the kinetic energy, the second is the rest energy, and the third is the interaction with the fields. The $\alpha = (\alpha_x, \alpha_y, \alpha_z)$ and β are

the Dirac matrices

$$\alpha_i = \begin{pmatrix} 0 & \sigma_i \\ \sigma_i & 0 \end{pmatrix}, \tag{2.22}$$

$$\beta = \begin{pmatrix} I_2 & 0 \\ 0 & -I_2 \end{pmatrix}, \tag{2.23}$$

where the σ_i are the Pauli matrices and I_2 is the 2×2 identity matrix. Naturally, as $\psi(\mathbf{r}, t)$ is a spinor, it does not need the by-hand spin introduction; it contains the effect of the spin since the beginning. For more details on the theory and mathematical work, the reader can refer to chapter 11 in Feliciano Giustino's book on DFT [91], and Part III in Richard M. Martin's book [92].

2.5.1 Exchange-correlation functionals

As in any theory, not everything is perfect. In the process of switching the all-electrons wavefunction for the electronic density, something is lost, rendering the electron-electron interaction misrepresented. Therefore, a part of the interaction energy, that is not contained in the noninteracting kinetic energy or the electrostatic potential, is missing. The term accounting for this missing part of the energy is called the exchange-correlation energy, E_{XC}. It contributes to the interaction potential with the exchange and correlation potential

$$V_{XC}(\mathbf{r}) = \frac{\delta E_{XC}(\mathbf{r})}{\delta n(\mathbf{r})}. \tag{2.24}$$

Because the exact form of E_{XC} is unknown, the potential V_{XC} can not be calculated. Therefore, it is subject to approximations; some are based on the theory, while others integrate the theory with experimental data. Some of the most known XC functionals are local density approximation (LDA) [89], Perdew-Burke-Ernzerhof (PBE) [93], PBEsol [94][3], and the strongly constrained and appropriately normed semilocal density functional (SCAN) [95]. The LDA functional models the exchange as in the case

[3] PBE corrected for solids

of a noninteracting gas of electrons with no potential energy; therefore, correlations are misrepresented in this approximation, making it prone to overbinding. The PBE functionals, which belong to the family of generalized gradient approximation, depending on the local density and its spatial derivative, can correct some of the flaws of LDA, but in some cases, underbind the atoms. PBEsol is a revised version of the PBE functional, more robust to rapidly varying electron densities in densely packed solids. SCAN functional belongs to the meta-GGA functionals and which, besides the theoretical framework, is designed to reproduce experimental data of reference. This functional manages to achieve very accurate results with a low computational cost when compared to nonlocal functionals. Moreover, there are other approximations, called hybrid functionals, which include a greater part of the all-electron problem with no approximations and mix it with some of the methodologies before mentioned. Some examples are HSE03 [96] and HSE06 [97].

A good approximation to the E_{XC} is fundamental for an adequate description of the physics in periodic systems as crystalline structures. Highly correlated systems, such as those containing d- and f-orbital electrons, are susceptible to correlation issues within the framework of DFT. Another illustrative example is given by systems with a strong spin-phonon coupling, which also need a good balance between the electronic interactions and the structural properties. A well know approach to the selection of the exchange and correlation functional is known as the "Jacob's ladder" [98]. It establishes a comparative measurement of exchange and correlation interaction of the different approximations to a ladder in which the Local Spin Density approximation lays at the bottom with the least amount of this interaction, followed by the GGA functionals with a better representation of the exchange and correlation. In this line, the GGA functionals are followed by meta-GGAs[4] and the hybrid functionals such as HSE03 and HSE06. In this sense, variations within the Jacob's ladder allow fitting the exchange and correlation representation of the system.

[4]meta-GGA are an enhancement of the GGA with the inclusion of local kinetic energy density.

2.6 Wannier functions for band structure interpolation and anomalous Hall effect calculations

The Wannier functions form a complete orthonormal set able to represent molecular orbitals in crystals [99, 100]. As such, a transformation between the Bloch states and the Wannier functions must exist. However, unlike Bloch states, Wannier functions are localized in the space, making them sensitive to introducing additional phases. For a set of Bloch states

$$\psi_{\mathbf{k}}(\mathbf{r}) = e^{i\mathbf{k}\cdot\mathbf{r}} u_{\mathbf{k}}(\mathbf{r}), \tag{2.25}$$

the corresponding Wannier functions can be obtained as

$$w_{\mathbf{R}}(\mathbf{r}) = \frac{1}{\sqrt{N}} \sum_{\mathbf{k}} e^{-i\mathbf{k}\cdot\mathbf{R}} \psi_{\mathbf{k}}(\mathbf{r}), \tag{2.26}$$

However, due to the phase dependence of the Wannier functions, an adjustment of the phase in the set of Bloch states is required to obtain the maximally localized Wannier functions (MLWFs). Once the MLWFs are found, several properties can be calculated on top of them; the Berry curvature, the anomalous Hall conductivity, and the spin Hall conductivity are examples of such.

Of course, obtaining the Wannier functions, a process called wannierization, is not as simple as shown here. For instance, the bands to be wannierised need to be classified by isolated and entangled; the first, attains to band separated from the rest by an energy gap, and the second category is for bands that do not fulfill the isolated criteria. In the case of J isolated bands, the MLWFs ($W_{n\mathbf{R}}$) for a cell unit of volume V are obtained through a unitary transformation U as follows

$$|W_{n\mathbf{R}}\rangle = V \int_{BZ} \frac{d\mathbf{k}}{(2\pi)^3} e^{-i\mathbf{k}\cdot\mathbf{R}} \sum_{m=1}^{J} |\psi_{m\mathbf{k}}\rangle U_{mn\mathbf{k}} \tag{2.27}$$

The unitary transformation U is responsible for the Bloch states phase adjustment, and thus the link between the Bloch states gauge independence and the MLWF spread around their center. Thus, with the help of this transformation, the spread of the

Wannier functions can be minimized. The process for the entangled bands is more elaborated and will not be discussed here; one important difference is that the number of bands is not constant for any **k** within a given energy range.

Fortunately, the process of wannierisation, along with many other features, is already implemented in the `Wannier90` code [101], which is an open-source code maintained by the same people who use it. At this time, wannier90 allows us to wannierize and disentangle the bands but also provides a post-processing tool called `postw90`, capable of calculating several electronic properties.

2.6.1 WannierBerri

In this section, a brief description of the WannierBerri library will be given. WannierBerri [102] is a python library to calculate various electronic properties, such as the AHC, optical conductivity, and orbital magnetization, among others. To do so, it uses the interpolation in Wannier functions over dense grids of k-points. Wannier interpolation is useful for calculating integrals of very rapidly varying functions, such as the AHC and the optical properties. Although, the Wannier90 package includes all the necessary tools to obtain such properties, the compound subject of study in modern research works is getting more complicated. Therefore, due to the complicated Fermi surfaces these materials require, the sampling of the Brillouine zone needs a large amount of Wannier functions. The latter result in a considerably increased computing time. In this regard, the WannierBerri code is more efficient, implementing an adaptive mesh, which refines the integration grid around the points with highly variating and highly contributing parts of the integral. Additionally, the WannierBerri code implements symmetry operations to reduce the number of calculations. Thus, WannierBerri can be even 1000 times faster than Wannier90 at calculating integrals over the Brillouine zone. Advantageously, WannierBerri allows doing all the mentioned work starting from the full set of Wannier90 files (i.e., wannier90.chk, wannier90.mnn, wannier90.eig, and wannier90.amn) or from the tight binding hamiltonian which was

in our case 1/5 the size of the Wannier90 files. All the AHC calculations shown in this thesis were performed in the WannerBerri code.

Chapter 3

The effect of the correlations in the Mn_3BN (B = Ni, Pd, and Pt) non-collinear magnetic antiperovskites

3.1 Introduction

Antiperovskites, A_3BX [27] (also known as inverse-perovskites), such as Mn_3NiN, are cubic structures similar to perovskites in which the cation and anion position are interchanged within the unit cell for the standard perovskite crystal structure [103]. Thus, the anions occupy the octahedral center instead of the corners, which becomes the site for the transition metal cations, forming a XA_6 octahedra. This type of coordination, coupled with their magnetic response, gives unique properties such as the anomalous Hall conductivity, AHC, [39, 40], negative thermal expansion [41], giant piezomagnetism [42], magnetic frustration [43, 44], among others [1, 28, 29, 30, 31, 32, 33, 34, 35, 36, 37, 38]. In particular, the magnetic frustration in triangular magnetic coordination relies on the metallic direct Mn–Mn exchange and the

Mn–N–Mn superexchange interaction. Thus, the metallic Ruderman-Kittel-Kasuya-Yosida (RKKY) interaction, which favors an antiferromagnetic collinear arrangement [104], is more prominent but is in competition with the superexchange [105, 106] interaction mediated by the nitrogen site at the cell center. Apart from the exchange and the superexchange, there is also an antisymmetric coupling, the Dzyaloshinskii-Moriya interaction, DMI, which is present in the (111)-plane inducing canting, which further increases the frustration [107, 44]. Combining all the discussed interactions converges into non-trivial, noncollinear, and possibly chiral magnetic ordering. In this case, the chirality is vectorial and results from the removal of the mirror symmetry due to the magnetic orderings, developing a well-defined handedness given by $k = \frac{2}{3\sqrt{3}} \sum_{ij} [\vec{S}_i \times \vec{S}_j]$ (where i, j runs over all the magnetic moments) [108, 109]. For example, the triangular frustrated magnetism in Mn_3NiN is compatible with the Γ_{5g} and Γ_{4g} [43] irreducible representations. In the case of Γ_{4g} (MSG. 166.101), the ordering is symmetric under the simultaneous application of both the time-reversal symmetry, $\mathcal{T}$, and the mirror symmetry, $\mathcal{M}$, along the M_{100}, M_{110} and M_{010} planes in the Seitz notation; conversely, in the Γ_{5g} case, (MSG. 166.97), the $\mathcal{T} * \mathcal{M}$ is broken due to the magnetic ordering [40]. Moreover, although the overall electronic band structures of both magnetic phases are reasonably similar, the mirror symmetry breaking in the Γ_{4g} allows a sizeable AHC, unlike in the case of Γ_{5g} in which the AHC is null [40]. The AHE in antiferromagnets has risen in research interest due to the possibility of dissipation-less current [18] thanks to the large AHC found in Mn_3Sn and Mn_3Ge [110, 111, 14]. Despite presenting a low density of states at the Fermi level, noncollinear antiferromagnetic antiperovskites are good conductors with a tunable AHC, with strain as the key to accessing this controllability. The strong magnetostructural coupling in the Mn-based antiperovskites [112, 113], on top of the subtle balance between the magnetic, ionic, and electronic structure renders these systems as strongly correlated. Notably, spin-phonon coupling studies in Mn_3NiN, show a marked sensitivity of the octahedral vibrational modes to the Coulomb correlation parameter U in the PBEsol+U scheme [114]. In-phase and out-of-phase unstable octahedral vibrational modes were reported for the U = 6.0 eV

correlation parameter, whereas for other U values, the volume changed tangibly. Thus, an appropriate description of the correlation energy is key to stabilizing the structure and properly reproducing the physical properties in Mn_3NiN. Partially filled d orbitals are often related to this behavior. Manganese-based antiperovskites fall into this category, presenting as correlated systems in which the B site along with the Mn site, are responsible for their behavior.

Therefore, in this chapter we address, within the first-principle calculations framework, the electronic correlations and their appropriate modeling in the manganese nitride antiperovskites. To do so, a structural and electronic characterization study will be performed under various options for the exchange and correlation functional, following the "Jacob's ladder" [98] paradigm and variations of the Hubbard correlation parameter. Thus, the exchange and correlation approximation selection will be justified, and the need for the Hubbard correction will be highlighted at the end of this chapter.

3.2 On the challenges of DFT and the exchange and correlation problems

DFT is a solid first-principles theory that allows us to perform effective and fast calculations of the electronic and ionic structures in crystalline solids. However, there are a few areas in which the theory suffers in modeling the physics adequately, leading to subtle deviations and, in some cases, unfeasible structures and non-physical properties. In topological insulators, the electronic structure is very sensitive to the XC. For example, the bandgap, an essential feature of a TI, varies widely from the PBE to the GW XC functionals, giving differences of several times in energy [115]. The Chern number C is also affected by the XC chosen; in $FrBr_3$, the C topological number is $C = 1$ for PBE, and $C = 0$ for PBEsol [116]. Moreover, in OsO_2, the Chern number depends on the magnetic easy–axis, changing from $C = -2$ to $C = 0$ for the $(0,2\pi)$ range of angles.

This time from the structural viewpoint, a different kind of instability has been spotted in the Fergusonite to Scheelite phase transition in $BiVO_4$ [117]. There, under the PBE approximation, an unusual transition from the monoclinic scheelite to the tetragonal scheelite happens. In this case, the initial crystalline structure confirmed experimentally has a lower symmetry than the tetragonal structure after the transition, going against the expected transition to a lower symmetry group as in the case of $BaTiO_3$ [118]. The reports by Olsen et al. [117] indicate the need for a large Hartree-Fock e–e exchange correction of 60% within a hybrid HSE06 XC functional. The optimization of this structure in the meta-GGA SCAN failed to retain the monoclinic symmetry. On the Other hand, the PBEsol with a Hubbard correction of 4.0, 7.0, and 10.0 eV in the $6s$ of the Bi sites managed to accurately keep the monoclinic scheelite structure while obtaining the lower ground state energy. Significantly, the DOS of $BiVO_4$ for the hybrid XC differs markedly from the PBEsol, giving a wide open bandgap of E_g = 7.0 eV for the first and E_g = 2.2 eV for the latter. Thus, the hybrid functional best reproduces the structural properties, but the PBEsol resolves the polarizability of the O site better. However, a Hartree-Fock exchange much higher than the default value of $\alpha = 0.25$ is needed to achieve such structural stability. This is a perfect example of the strong correlations typical of the transition metal oxides, which push the DFT beyond the limits of its functionality.

Stabilizing the structural properties of strongly correlated compounds is vital to correctly describe the physics happening inside them. Studies on the LDA pressure [119] show an unstable structure in the ferroelectric $BaTiO_3$ in the LDA approximation. An a = 3.94 Å lattice parameter is obtained after the structural optimization, conversely to the experimental parameter a = 4.0 Å. As well established, the ferroelectrics are compounds strongly correlated and highly sensitive to the strain [120]. In the mentioned thesis, this difference in the lattice parameter is addressed as a negative pressure on the structure of -10 GPa. Interestingly, such pressure was proven to induce unstable phonons in the structure.

3.3 Theoretical and Computational Details

For the development of this chapter, first-principles calculations within the density-functional theory (DFT) [121, 89] approach by using the VASP code (version 5.4.4) [45, 46] were performed. The projected-augmented waves scheme, PAW [122], was employed to represent the valence and core electrons. The electronic configurations considered in the pseudo-potentials, as valence electrons, are Mn: ($3p^6 3d^5 4s^2$, version 02Aug2007), Ni: ($3p^6 3d^8 4s^2$, version 06Sep2000), Pd: ($4p^6 4d^{10} 5s^0$, version 28Jan2005), Pt: ($5p^6 5d^9 6s^1$, version 12Dec2005), and N: ($2s^2 2p^3$, version 08Apr2002). The exchange-correlation was represented within the LDA [89], GGA-PBEsol parametrization [94], SCAN [95], and HSE06 [97] in order to reproduce the experimentally observed magnetic moment. The Mn:3d orbitals were corrected through the DFT+U approximation within the Liechtenstein formalism [123]. Variations in the U parameter ranging [0.0,3.0] eV were implemented to study the effect of the exchange-correlation energy in the strong magnetostructural response observed in the Mn_3AN antiperovskites [13]. The U = 2.0 eV parameter was selected as the best setup in the Mn:3d orbitals. This U value allows the structural optimization to reproduce the experimentally observed lattice parameter, which is crucial in obtaining an appropriate charge distribution and, ultimately, the electronic properties under strain. Moreover, the electronic structure of Mn_3BN obtained with PBEsol+U is compared with the computed by the strongly constrained and appropriately normed semilocal density functional, SCAN, [95, 114], observing a fair agreement of the electronic structure in both cases. Importantly, recent reports of SCAN-based calculations have shown results in good agreement with the experimental reports, including the lattice parameter [124, 125], and the magnetic and the electronic structure [112] in strongly-correlated 3d perovskites and Heusler Mn-based alloys [126]. The periodic solution of the crystal was represented by using Bloch states with a Monkhorst-Pack [127] k-point mesh of 13×13×13 and 600 eV energy cut-off to give forces convergence of less than 0.001 eV·Å^{-1} and an error in the energy less than 10^{-6} eV. The spin-orbit coupling (SOC) was included to consider

non-collinear magnetic configurations [128]. The anomalous Hall conductivity, and associated observables, were obtained with the Python library WannierBerri [102] using the maximally localized Wannier functions and the tight-binding Hamiltonian generated with the Wannier90 package [101]. The interpolation was performed with 80 Wannier functions with projections on the s,p,d orbitals for the Mn, Ni, Pd, and Pt atoms while s,p orbitals where taken into account for N atoms. For the disentanglement process, we used an energy window +3.0 eV higher than Fermi level as the maximum, and none for the minimum, and a convergence tolerance of 5.0×10^{-8} Å^2. The atomic structure figures were elaborated with the VESTA code [129]. Finally, the band structure was analyzed with the Python library PyProcar [130].

3.4 Structure and Magnetism Under XC

The family Mn_3BX (B = metal, X = C and N) of antiperovskites are well known for their wide variety of functional properties [28] related to the strong magnetostructural coupling present in those compounds [13] and their tuneability through external perturbations. Good examples of such physical properties are the giant negative thermal expansion [30], the barocaloric effect [131], the giant anomalous Nernst effect [132], the anomalous Hall effect [133, 39, 40], the piezomagnetic effect [34], and the spin-orbit torque (SOT) [134]. In the early works of Fruchart and Bertaut [43], wide variations in the DOS around the Fermi level were reported as a function of the temperature in Mn_3BX, the latter attributed to the p–d hybridization between the X and Mn sites [135]. Notably, due to such hybridization, the compound is significantly sensitive to variation in the X and B sites present in this family of compounds. Additionally, the B and Mn atomic site contributions are crucial to the electronic structure around the Fermi level, ultimately defining the transport phenomena in these antiperovskites. On the other hand, the stability of the structure and the strength of the Mn magnetic moments are mainly influenced by the Mn–X correlation. In Mn_4N antiperovskite (*i.e.* Mn_3MnN) it has been observed a magnetic moment of $\mu(\mathrm{Mn}^I) = 3.9\ \mu_B$ for the Mn in

the octahedral center and $\mu(\mathrm{Mn}^{II}) = 0.9\ \mu_B$ [43] for the Mn in the corners of the cubic structure in the $3c$ and $1a$ Wyckoff positions respectively. Thus, the magnetic moments of Mn^{I} profit from the Mn–N bound in the octahedral center conversely to the decremented magnetic moment for the Mn^{II} in the cubic corner with a curie temperature T_c = 756 K. However, different B metals induce different cell volumes as can be seen in the experimental data gathered for the lattice parameter in the first column of Table 3.1. The lattice parameters data for the PBEsol+U=2.0 eV and PBEsol are consigned in the second and third columns of Table 3.1, showing the behavior $lattice\ parameter_{Ni} < lattice\ parameter_{Pt} < lattice\ parameter_{Pd}$. Noteworthy, the data consigned in this table reveals a strong effect of the U parameter on the structural properties of the three compounds, suggesting a strongly correlated structure.

Table 3.1: *Experimentally reports on the lattice parameter, in Å, for Mn_3BN with B = Ni, Pd, and Pt. Additionally, the computed values, at different U parameters under the PBEsol exchange-correlation, are presented.*

		This work	
B	$a_{Exp.}$ (Å)	PBEsol (U = 2.0 eV)	PBEsol (U = 0.0 eV)
Ni	3.886 [39]	3.894	3.652
Pd	3.985 [49]	3.984	3.726
Pt	3.9699 [135], 3.968[136]	3.967	3.732

Such variations in the B-site also induce a tangible effect on the magnetic moment magnitude as shown in Table 3.2 where the magnetic moment for the Mn sites in each structure is shown for the experimental, HSE06, SCAN, and PBEsol (U=2.0 eV, experimental volume cell, and U=0.0 eV) approximation cases; in all the cases the except for U = 0.0 eV the relation $\mu_B(Ni) < \mu_B(Pt) < \mu_B(Pd)$. Here again, the effect of the e-e interaction energy U is clearly observed, increasing largely the magnetic moments the in U = 2.0 eV with respect to the U = 0.0 eV with the experimental volume. Fur-

thermore, among all the non-hybrid functionals, the PBEsol+U = 2.0 eV is the most close to the results obtained in the hybrid scheme. Thus, even though it is possible to achieve the correct magnetic ordering on the U = 0.0 with the experimental volume, the magnetism is still a misrepresented property. Therefore, variations in the volume and the magnetic moments correlate through the B site substitutions and are only appropriately reproduced within a correlation-corrected scheme such as PBEsol+U, SCAN, and the hybrid.

Table 3.2: *Experimental reported and calculated magnetic moment in μ_B for Mn_3BN for the XC approximations HSE06, SCAN, PBEsol with and without the U=2.0 eV Hubbard correction. The latter are computed in the experimental volume imposed and the fully relaxed cases.*

		This work				
B	Experimental	HSE06	SCAN	U=2.0 eV	U=0.0 eV, exp. vol.	U=0.0 eV, rel.
Ni	3.0 [137]	3.85	3.39	3.57	2.92	1.50
Pd	–		3.65	3.76	3.22	2.35
Pt	3.5 [1][136]		3.60	3.71	3.13	3.17

Besides, the B site, the nitrogen site is also important in defining the volume of the structure. A quick check on the Mn_3Pt experimental lattice parameter $a_0 = 3.833$ Å [11] against the Mn_3PtN, $a = 3.970$ Å, confirms that nitrogen in the center of the octahedra dramatically increases the cell volume. Furthermore, variations in the content of N, as in Mn_3PtN_x ($0 \leq x \leq 1.0$) [136], induces a triangular antiferromagnetic (AF) to collinear AF phase transition at $x = 0.15$, which reach a rhombohedral structure after $x = 0.4$. Moreover, there is a lowering of the critic transition temperature for $x = 0.02$, where the $a_0 = 3.870$ Å. The collinear AF phase is sustained up to $x = 0.15$, where a transition to a hexagonal structure happens that holds up to $x = 0.4$. Further increasing

[1] In Mn_3PtN_x with little or zero N content.

x, induces an hexagonal to cubic transition with lattice parameters of $a_0 = 3.925$ Å and $a_0 = 3.972$ Å for $x = 0.4$ and x=1.0, respectively. Thus, taking Mn_4N and Mn_3PtN_x as examples, it can be inferred that the electronic structure, the magnetism, and the crystalline structure are intimately linked in the Mn_3BX antiperovskites, producing their characteristic response to mechanical stimuli such as the epitaxial strain. As such, the structure, magnetism, and electronic structure are entangled, and therefore, influences the remaining physical properties. All the latter can be traced back to the strongly correlated behavior induced by the partially filled d orbitals in the Mn and the B sites which suffer from the misrepresented e-e interaction. Therefore, a deeper understanding of the electronic correlations in these sites is required to properly model the manganese nitride antiperovskite structures and their properties.

It is worth mentioning that another vital role that nitrogen plays in the Mn_3BN structure is the mediation of the Mn–N–Mn superexchange interaction that shapes the magnetic ordering along with the Mn–Mn exchange and the Dzyaloshinskii-Moriya interaction (DMI). Then, the proper representation of the exchange-correlation in the Mn sites will directly affect the magnetic properties in the Mn-based antiperovskites. The combination of all the before-mentioned structural characteristics and interactions produces the characteristic Γ_{4g} and Γ_{5g} magnetic orderings in this family of compounds.

The determination of magnetism in noncolinear antiferromagnets is a very challenging task. Experimentally, the magnetic structure can be resolved through neutron powder diffraction, guided by symmetry considerations and spectra analysis, allowing the determination of the direction of the magnetic moments in the crystal. Measuring the magnitude of the moments is a more problematic endeavor; being a zero net magnetization system, the magnitude of a single moment is undetermined due to the multiple solutions to the summation over all the $\mathbf{m}_i$ magnetic moments, $\sum_i \mathbf{m}_i$=0, the constraint of the antiferromagnetic sublattices. For this reason, there are very few experimental reports on the magnetic moments per atomic specie in non-collinear frustrated antiferromagnets such as the ones we are focused on in this work (see Table 3.2). Table 3.2 contains the magnetic moment per Mn atomic site calculated in the

hybrid-HSE06 [138], meta-GGA[139] SCAN [95], and the GGA [93, 140] PBEsol [94] approximations; which follow the *"Jacob's ladder"* [98] with PBEsol in the lowest level. In this case, the HSE06 hybrid functional works as a trustable reference parameter due to its more detailed and complete description of the electronic interactions. Moreover, the GGA-PBEsol is known for achieving good results in the charge density and the physical properties of many solids. Thus, the data in table 3.2, shows a correlation of the magnetic moment magnitude to the cell volume; a bigger cell volume induces larger magnetic moments. Therefore, substitutions of the atomic site in the corner of the cubic cell change its volume, ultimately modifying the magnetic moments of the Mn sites in the octahedral center. Here, the 3*d*-orbitals of the Mn site 'inflate' or 'deflate' to fill the available space.

From Table 3.2, we can observe that all the XC functionals give the same trending in the magnetic moment magnitude, except for the PBEsol with U = 0.0 eV, which breaks the pattern, throwing a monotonically increasing moment with the atomic substitutions Ni, Pd, and Pt. Furthermore, in the U = 0.0 eV with relaxed volume case, the Mn magnetic moment of Mn_3NiN is notably smaller when compared to the Mn_3PdN and Mn_3PtN cases; presumably due to the misrepresentation of the e-e electrostatic interaction energy, which traduces in a small volume of the unit cell and more tightly bounded electrons in the d orbitals, allowing the spins in the d orbital to align mainly antiferromagnetically, lowering the effective magnetic moment. Moreover, the structural stability of Mn_3NiN is compromised when the U correction parameter is neglected and the structural relaxations are performed, giving rise to unstable phonons [114]. Therefore, it can be inferred that the absence of the Hubbard correction and the misrepresented cell volume leads to an erroneous electronic structure calculation. The latter is linked to the strong electronic and spin-phonon coupling in this compound [114]. Thus, among the studied cases, the setup structurally optimized in the PBEsol scheme with no U correction should be avoided if electronic structure-dependent physical properties are to be calculated, as in the case of the AHC. Finally, the PBEsol+U = 2.0 eV configuration resulted as the closest to the meta-GGA and hybrid approxima-

tions. In the following section, a comparison of the results in the GGA approximation is given in order to further establish the relevance of correlation correction in the manganese nitride antiperovskite compounds.

3.5 Effect of XC on the Electronic Structure

Mn_3BN antiperovskites have been reported as strongly correlated systems, a feature also attributed to the $2p$:N–$3d$:Mn hybridization [43]. However, more recent reports present Mn_3PdN as a weakly correlated system [49], based on the Kadowaki-Woods coefficient [141] of $A/\gamma^2 = 0.551a_0$. In heavy Fermion compounds with a relevant electron-electron correlation, the coefficient is $1.0a_0$. Conversely, both, Mn_3NiN and Mn_3PdN have been reported as sensitive to the strain in the (001) plane of the cubic structure that induces a structural phase transition to a tetragonal in which either the anomalous Hall effect (AHE) or the anomalous Nernst effect (ANE) gets enhanced [13, 39]. According to the reports, the strain controllability of the anomalous Hall conductivity (AHC) and the anomalous Nernst conductivity (ANC) arise from the prominence of the magnetostructural coupling and the control over the Weyl crossings, which respond to the strain that modifies the band structure. However, as we reported recently, the presence of the Weyl nodes at the Fermi level can be discarded as the primary source of the AHC, finding the most decisive contribution to this effect in the non-localized and non-divergent Berry curvature of the avoided band crossings in the (111) plane of the cubic structure [84]. The latter findings are discussed in the following Chapter 4. Additionally, an important magnetostructural coupling and electron-electron correlation have been confirmed by reports on the unstable phonons found at large tension values on the structure of Mn_3NiN [114]. The Hubbard model [142] provides a simple way to qualitatively understand the physical properties that arise from the electronic band structure; it states that the electronic structure results

[2] with A as the coefficient of the quadratic term of the resistivity, γ as the coefficient of the linear term in the temperature dependence in the specific heat and $a_0 = 1.0\times10^{-5}$ $\mu\Omega$cm/(mJ/mol· K)^2

from a competition between the electron-electron (e-e) repulsion and their kinetic energy. In noncorrelated systems, such as those consisting of s and p orbitals only, the orbitals from different atoms overlap considerably, up to the point that the electrons behave much like in a gas, in which case, the kinetic energy is far more important term than the e-e repulsion [89]. Thus, the electronic structure is mainly defined by kinetic energy; here, the DFT works really well [143]. Conversely, a partially filled $3d$ orbital in a solids feels a strong nuclear potential because of the low screening that the higher shell $4s$ orbital offer. The *Slater's rule* [144], establish the nuclear charge shielding s for the atomic orbitals as $s_s > s_p > s_d > s_f$, allowing the effective nuclear charge Z_{eff} to increase along with the number of electrons. Thus, leaving the d orbitals more localized and bound to the nucleus. Therefore, in such systems the d orbitals overlapping is minimum and the e-e repulsion dominates the electronic structure. Hence, a more localized and correlated behavior of the electrons is observed [145]. Such correlated behavior demands a fair representation in order to accurately reproduce the physics of the system.

Electronic structure characterization of the Mn_3BN (B = Ni, Pd, and Pt) has been performed to check on the effect of different electronic correlations among the three compounds. The band structure for the three compounds is shown in Fig. 3.1 for the Hubbard correction $U = 2.0$ eV, $U = 0.0$ eV [4] cases. First, a quick inspection of all the band structures reveals a boldly marked difference between the $U = 0.0$ eV relaxed concerning the experimental volume imposed and the $U = 2.0$ eV optimized structure. This was expected because the electronic structure obtained through the $U = 0.0$ eV relaxed calculation setup appears as inaccurate when compared with the electronic structure obtained with the GGA and hybrid functionals, due to the misrepresentation of the correlations present in the U=0.0 eV case. The misrepresentation of the e–e correlations affects the magnetism and the electronic properties, producing erroneous results, as mentioned before. On the other hand, between the $U = 0.0$ eV with experimental volume and the $U = 2.0$ eV relaxed structure cases, various similarities can be

[4] The relaxed cell and the fixed experimental volume cell cases.

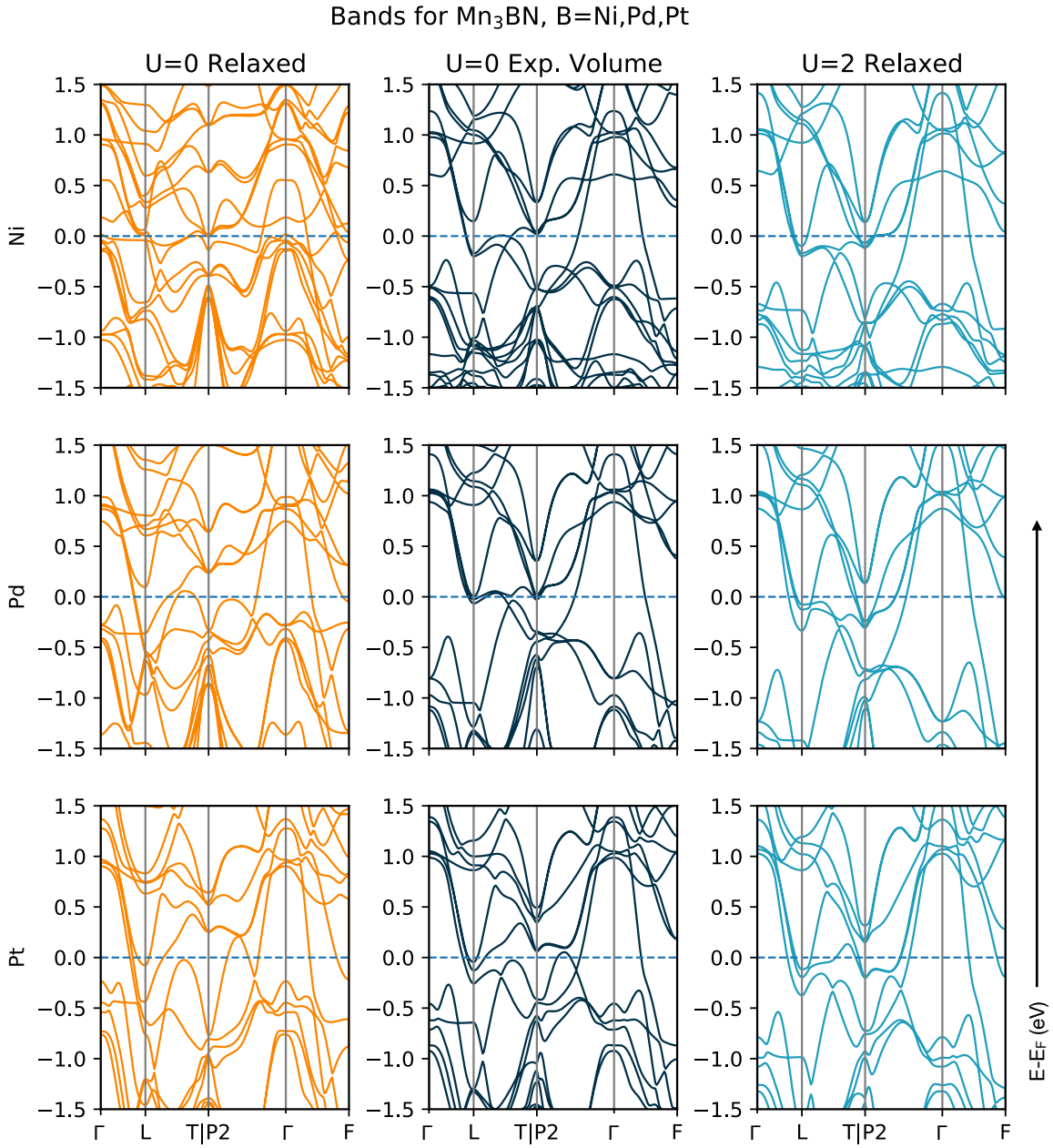

Figure 3.1: *Band structure for Mn_3NiN, Mn_3PdN and Mn_3PtN calculated for the relaxed structure without the Hubbard correction in the left column, fixed to the experimental volume without the Hubbard correction in the middle column, and relaxed with the U=2.0 eV Hubbard correction in the right column.*

observed, with essential differences in the L–T and the $P2$–Γ paths being spotted. In the L-T path, which lies along the (111) plane of the cubic structure, the differences are noticeable, and their consequences on the Berry curvature should be explored in more detail to establish the role of that topological field on the AHC. Although the bands in that path are relatively similar for both cases, there is an energy difference concerning the $U = 2.0$ eV case. In the $P2$-Γ path, Mn_3NiN and Mn_3PdN are very similar, but in the case of Mn_3PtN the band structure differs notably. Observing the band structure for each compound and each case, sizeable variations in the Fermi level are found; in each case, the structures conformed by the energy bands are located in different energy levels. So far, the band structure obtained through the $U = 0.0$ eV with experimental volume and the $U = 2.0$ eV relaxed setups are mostly the same with minor energy deviations one from another; meanwhile, the $U = 0.0$ eV optimized structure calculations of the bands, reveal a more crowded arrangement and show little similarity to the other cases. Thus, obtaining a correct electronic band structure in a GGA approximation implies either the experimental volume imposition or the electrostatic interaction correction through the U parameter. The latter poses an advantageous automatically reproduced experimental volume along with the electronic band structure and with it, a proper implementation of the electronic correlations.

In Fig. 3.2, there are three columns with the d projected DOS for Mn_3NiN, Mn_3PdN and, Mn_3PtN from left to right respectively; each column shows the effect of variations of the Hubbard parameter in the range U = [0.0, 3.0] eV. For U = 0.0 eV, a hybridization of the 3d-Mn and the d-B can be observed within [-2.0,-1.0] eV for B = Ni, [-4.0, 0.0] for B = Pd and, [-4.0, 0.0] for B = Pt. The contribution of each atom to the DOS in the mentioned range of energies is affected by the Hubbard correction in all the cases; a very important factor in compounds with itinerant magnetism. Another effect of the $e - e$ interaction correction is related to the broadening of the valley present around the Fermi energy in all the compounds; relevant to the conduction and magnetic phenomena in these compounds.

Moreover, analyzing the data from the electronic correlations, another important

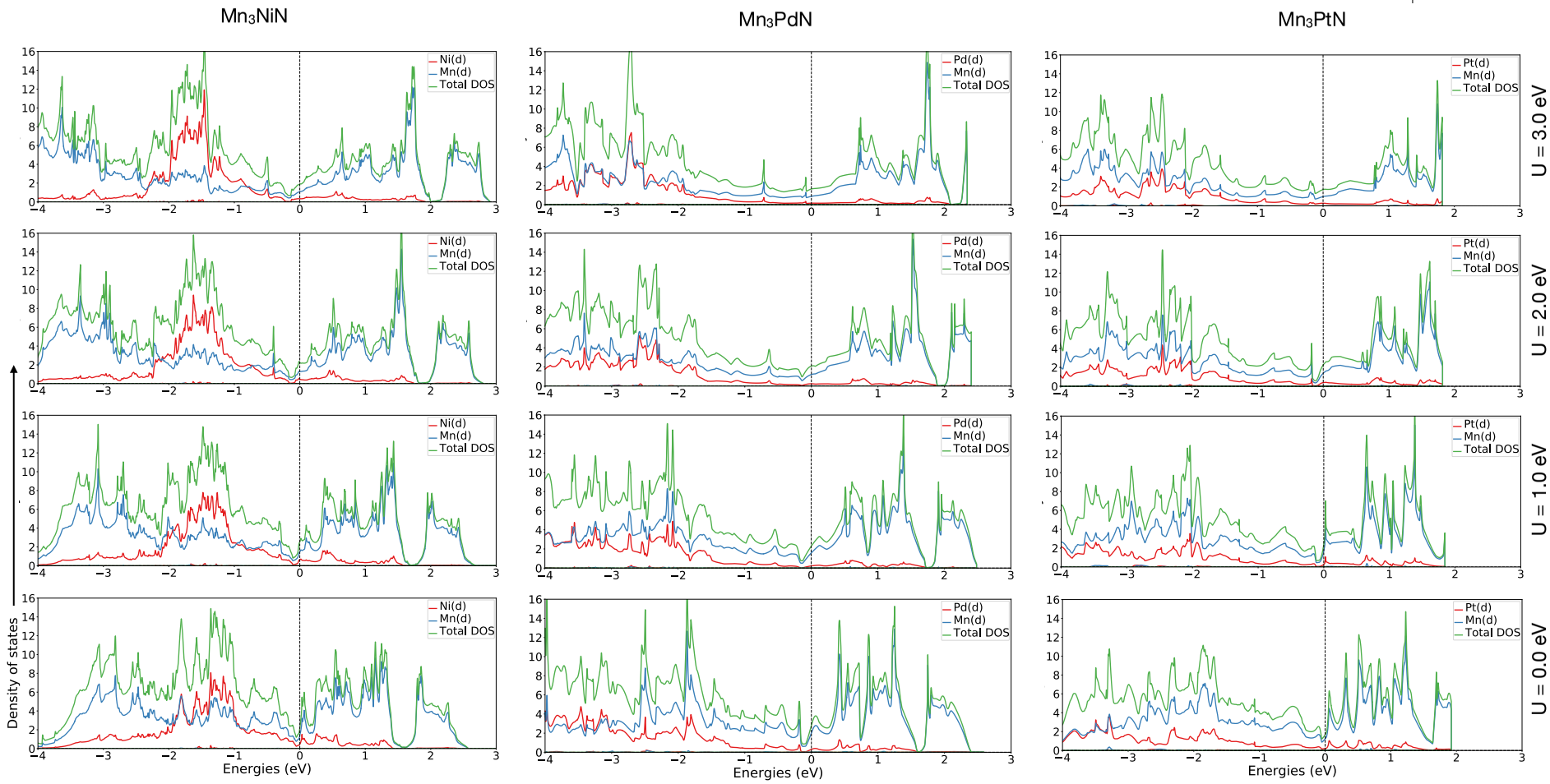

Figure 3.2: *Density of states vs E-E_F for Mn_3NiN, Mn_3PdN and Mn_3PtN, with the experimental volume fixed and the Hubbard parameter U = 0.0, 1.0, 2.0 and, 3.0 eV.*

interaction is the spin–orbit coupling (SOC). The SOC gets stronger when advancing vertically in the periodic table due to its marked dependence on the effective nuclear charge Z_{eff}. Thus, a way to investigate the effect of the spin-orbit coupling in the Mn_3BN antiperovskites is to set B = Ni, Pd, and Pt to successive increase the SOC while keeping the symmetry and the structural properties. Regarding the band structure, the effect of the SOC can be observed in the band repulsion which also increases with the SOC. For example, the group of bands near E = −0.5 eV in the Γ point for B = Ni are more spread in the case of B = Pd. This effect is even more prominent in the case of B = Pt.

3.6 Anomalous Hall Conductivity vs the Hubbard U Correction

The AHC reported here is calculated based on a modified version of the Eq. 2.9 which is defined as follows [146]:

$$\sigma_{\alpha\beta}^{AHE} = -\frac{e^2}{\hbar}\epsilon_{\alpha\beta\gamma}\int_{BZ}\sum_n \frac{d^3\vec{k}}{(2\pi)^3} f_n(\vec{k})\Omega_n^{\gamma}(\vec{k}), \tag{3.1}$$

Here, in Eq. 3.1, $\epsilon_{\alpha\beta\gamma}$ is the antisymmetric tensor, $\sum_n f_n(\vec{k})\Omega_n^{\gamma}(\vec{k})$ is the summation over all the included bands contribution to the Berry curvature, $\Omega_{\gamma}(\vec{k})$, and $f_n(\vec{k})$ is the Fermi distribution; the γ subscript runs over a discrete grid of energy points, allowing the AHC calculation in other energy levels apart from the Fermi level. The Eq. 3.1 is implemented in the WannierBerri code [102] which uses the Wannier functions to efficiently interpolate the band structure and various other physical observables [147]. Wannier interpolation for AHC calculation is performed after a previous calculation of the Berry curvature through the geometric formula in terms of the derivatives of the Bloch states [148].

$$\Omega_{n,\alpha\beta}(\mathbf{k}) = -2Im\left\langle \frac{\partial u_{n\mathbf{k}}}{\partial k_\alpha} | \frac{\partial u_{n\mathbf{k}}}{\partial k_\beta} \right\rangle \tag{3.2}$$

The derivatives in Eq. 3.2 are calculated in a explicit formula of the Wannier functions. The latter expressed in a efficient matrix form allowing to integrate in a dense grid of millions of points in the reciprocal space, instead of the reduced grids used in DFT. On top of that, WannierBerri uses the symmetry operations of the system to reduce the number of calculations as well as an adaptive mesh in order to properly capture the rapidly varying nature of the Berry curvature near band crossings [102].

The integral at the Eq. 3.1, depends on two main factors, the available electronic states around the Fermi level and the Berry curvature in the BZ. As such, due to its connection with the electronic structure, the AHC is very sensitive to the band structure and the Fermi-level energy. Thus, wide variations of the AHC magnitude are expected when there are minor variations in the Fermi level and the shape of the bands. The theoretical AHC reports found so far in the literature set the magnitude of the conductivity in the (111) plane of Mn_3NiN at values within σ_{111} = –300 S/cm and σ_{111} = 520 S/cm (see Table 3.3 with the reported values). The sign here should not be taken strictly; it depends on the coordinate reference position and orientation in the crystal. The experiments, however, reveal a different reality, the AHC σ_{111}^{AHE} in Mn_3NiN is reported as very weak by Zhao [133] and σ_{111}^{AHE} = 22 S/cm by Boldrin *et al.* [39]. To explain such a wide range of variations in the AHC when obtained by *ab-initio* calculations, one can appeal to cell volume variations [13], parameters of the relaxation, exchange-correlations approximations employed, and even perhaps, a wrong Fermi level definition. We explored the possibility of the electron-electron correlation misrepresentation in the *d*-orbitals as the source of all the unwanted outcomes; it is well known that the *e*–*e* interaction in strongly correlated systems is a pain point of the DFT. The PBEsol [149] GGA functional is a good way to reproduce the charge density and the properties of many solids. Still, in the case of low-populated *d*-orbitals, such as Ni and Pd, the correlation effect is considerably higher than in the highly-populated *d*-orbital counterparts (*e.g.* Zn) [150]; the structural, electronic, and physical properties of Mn_3ZnN can accurately be reproduced in the LDA, PBE, PBEsol, and among others. In the former, the cell volume and the magnetism are intimately related, and the

emergent properties, such as the AHC, depend on a fair exchange and correlation definition. In the MnBN compounds reviewed in this research, the structural, and electronic properties suggested that to capture the strongly correlated electron-electron *in-situ* interactions present in these systems, a GGA+U scheme is needed.

Table 3.3: *Theoretical and experimental reports on the AHC in Mn_3NiN, units in S/cm*

AHC in the Γ_{4g} magnetic phase of Mn_3NiN in S/cm	
Theoretical	Experimental
σ_{111}^{AHE} = 294.5 (σ_{xy}^{AHE} = 170) [39]	σ_{xy}^{AHE} = 22 [39]
σ_{111}^{AHE} = -301 (σ_{xy}^{AHE} = -174) [12]	
σ_{111}^{AHE} = 525 (σ_{xy}^{AHE} = 303) [133]	
σ_{111}^{AHE} = 375.7 (σ_{xy}^{AHE} = 217) [151]	
σ_{111}^{AHE} = 225 (σ_{xy}^{AHE} = 130) [40]	
σ_{111}^{AHE} = 118 (σ_{xy}^{AHE} = 68)[3]	

As observed in Table 3.1, the introduction of the Hubbard U = 2.0 eV achieves structures with lattice parameters in good agreement with the experiments. Furthermore, the AHC calculations for Mn_3NiN reported (presented in Table 3.3) show results far from the experimental measurements; meanwhile, the calculations with the appropriate Hubbard correction yield a more realistic value. At this point, the reproduction of the experimental cell lattice under ionic relaxation, the agreement of the magnetic moments with respect to the hybrid XC functional, and the better agreement of the AHC with the experiments are indicators of a better electronic structure calculation under the U = 2.0 eV Hubbard correction setup than in the other cases concerning this research. The results of the AHC obtained for Mn_3BN (B = Ni, Pd, and Pt) for various iterations with the WannierBerri code are shown in Fig. 3.3 and condensed in Table 3.4, which also includes the ionic radius of the B site. In that table, it can be

[3]This work

observed the behavior of the AHC under the effect of the different levels of electronic correlation can be observed in the horizontal direction, as well as the effect of different levels of SOC in the vertical direction. The Tight-Binding Hamiltonian for each system was obtained through Wannierization in the WANNIER90 code using the *s, p, d* orbitals projections, 80 Wannier functions, and 116 bands within the energy window E_F+3.0 eV (with E_F as the Fermi energy level).

Table 3.4: *Average of the AHC in the [111] plane, σ_{111}^{AHE}, of the Γ_{4g} magnetic phase of Mn_3BN in S/cm ± the standard deviation over the WannierBerri iterations.*

AHC calculations in Mn_3BN

	Ionic radius (pm)	Relaxed U=0.0 eV	Exp. Volume U=0.0 eV	Relaxed U=2.0 eV
Ni	149	93.6±6.5	259.5±1.0	117.2±16.5
Pd	169	51.7±0.5	-189.3±18.4	-133.9±1.9
Pt	177	854.8±1.9	383±0.6	-195.7±12.3

At first sight, the AHC in Fig. 3.3 appears to be highly oscillating; however, a more appropriate range on all the plots to better allow the comparison shows a different picture (see Fig. 3.4).

The AHC in non-colinear antiferromagnetic antiperovskites has been reported to be directly related to the SOC. Therefore, the results should exhibit an increasing SOC (for Ni, Pd, and Pt, respectively) with a rising AHC. However, the AHC magnitude is smaller for Mn_3PdN than in the Mn_3NiN and Mn_3PtN compounds for the $U = 0.0$ eV relaxed and the $U = 2.0$ eV with experimental volume cases (see Table 3.4). In the case of $U = 2.0$ eV relaxed, we found a one-to-one monotonically increasing relation between the SOC and the AHC. The SOC has been identified in the past as a source of AHC in antiperovskites [146]. Therefore, such a monotonically increasing relation between the AHC and the SOC is an indicator of a fair electronic structure calculation and the reliability of the physical properties obtained from that electronic structure.

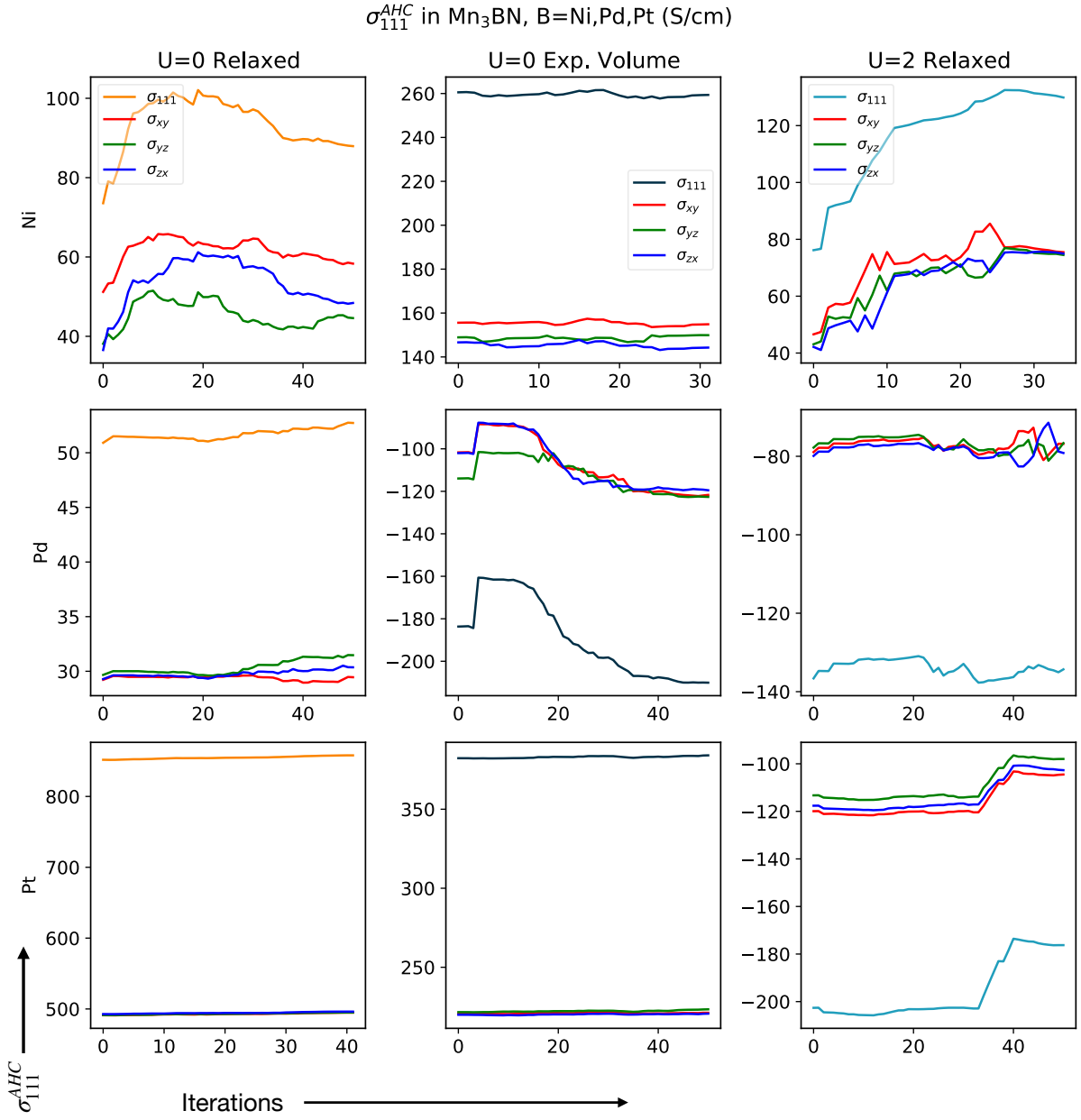

Figure 3.3: *AHC for Mn_3NiN, Mn_3PdN, and Mn_3PtN calculated for the optimized structure without the Hubbard correction in the left column, fixed to the experimental volume without the Hubbard correction in the middle column, and relaxed with the U = 2.0 eV Hubbard correction in the right column.*

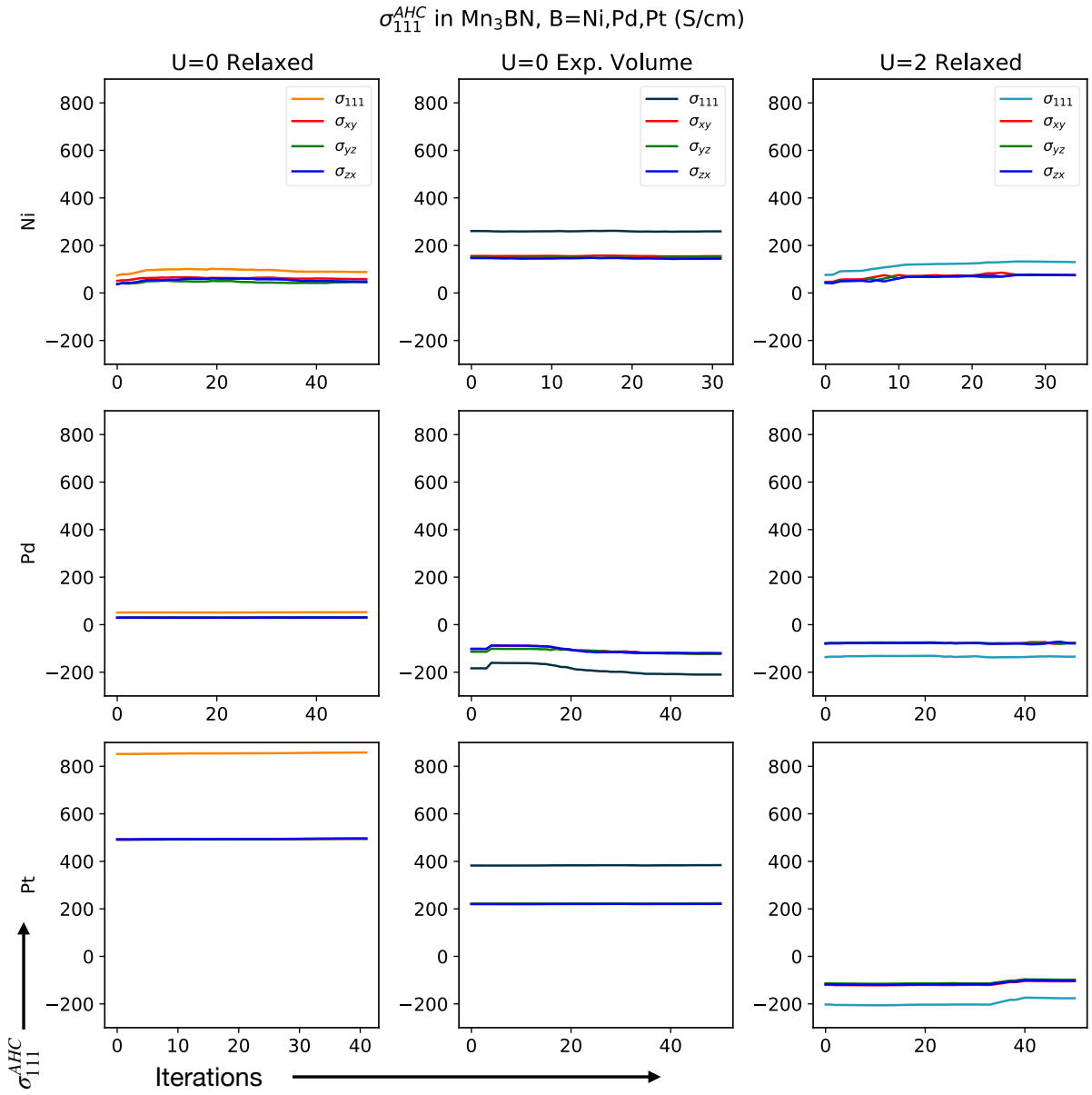

Figure 3.4: *AHC with a Standardized vertical axis range for Mn_3NiN, Mn_3PdN and Mn_3PtN calculated for the relaxed structure without the Hubbard correction in the left column, fixed to the experimental volume without the Hubbard correction in the middle column and relaxed with the U=2.0 eV Hubbard correction in the right column.*

Thus, the results shown suggest how the electronic correlations correction is essential to properly describe the physics in these systems; even thou PBEsol+U = 0.0 eV with the experimental volume gives a similar band structure to that of PBEsol+U = 2.0 eV, the AHC in the first does not follow the expected behavior of increasing along with the SOC; the U = 2.0 eV in the key to correctly resolve the physics in Mn_3BN.

3.7 Conclusions

The transition metal in the B-site (B = Ni, Pd, Pt) has direct implications in the cell volume and, in conjunction with the Mn site controls the transport phenomena at the Fermi level. Moreover, a d–d hybridization between Mn and the B sites is observed. Therefore, the B site is also a relevant factor in deciding the magnetism and consequently the anomalous Hall conductivity phenomena exhibited by these compounds. The hypothesis of this work relates the transition metal site B of the family Mn_3BN to the correlation and the SOC which has been highlighted by other authors as the main source of AHC in noncollinear antiferromagnets. The results revealed that cell volume expansion with the substitutions are accompanied by a magnetic moment increase through a spin-lattice coupling. Such process stabilizes and enhances the magnetic frustration, guaranteeing a non-vanishing Berry curvature. Our findings suggest that, due to the strong volume dependence in these compounds, the pure PBEsol approximation, without the U value, fails to capture the AHC behavior because of a wrong cell volume after the structural relaxation and misrepresented electronic correlations. Of course, being highly correlated systems, Mn_3BN antiperovskites are not adequately represented within a standard PBEsol approximation. The alternative approach of a fixed cell volume to the experimental value was able to partially solve the issue, improving the electronic band structure but still failing in capturing the AHC behavior. The latter, highlighting the importance of a correct description of the electronic correlations in the noncollinear antiperovskites. Among the studied cases in this chapter, the PBEsol+U = 2.0 eV, was the only GGA approximation producing a cell volume and

AHC results fitting the experimental data and the hypothesis proposed for the compounds studied here; the AHC was enhanced with the electronic correlations increasing with the successive substitutions B = Ni, Pd, Pt. Thus, the AHC in these compounds could be traced back to the spin-orbit coupling and the electronic correlations as has been suggested by other authors.

Chapter 4

Anomalous Hall conductivity controlling in Mn_3NiN antiperovskite by epitaxial strain along the kagome plane

4.1 Introduction

Among the Mn_3BN family on antiperovskites, the Mn_3NiN has been the subject of study of various works. Importantly, the possibility of controllability of the AHC in Mn_3NiN [40, 151, 39] has attracted a considerable amount of interest in the topological properties community. However, the source of its behavior is not yet completely established. There is still division among the topological (*i.e.,* Weyl nodes related) or trivial (*i.e.,* band coherences related) origin of the AHC in this compound. Moreover, the first-principles calculation reports on the AHC for Mn_3NiN are found along a wide range, σ_{111}^{AHE}= -301 S·cm^{-1} [12] to σ_{111}^{AHE} = 525 S·cm^{-1} [133] (see Table 3.3 for a comprehensive list of the AHC values reported in Mn_3NiN so far). Such results, coming from computational calculations, are most likely related to a marked dependence on

the approach and calculation parameters set by the authors. Notably, the theoretical and experimental reports on the AHC in (001) Mn_3NiN strained thin films result in a considerable disagreement, reported as $\sigma_{xy}^{the} \approx 170$ S·cm^{-1} and $\sigma_{xy}^{exp} = 22$ S·cm^{-1} in the same work [39]; an important difference that speaks about the intricate nature of the AHC source. However, such a finite increase of the AHC in the strained structure with respect to the vanishing AHC in the unstrained structure [133] reveals a path to control the AHC through strain. A compression (tension) to increase (decrease) relation can be derived between the strain and the AHC in Mn_3NiN. However, we suspect that experimental measurements of the AHC under the strain before mentioned are a product of a non-vanishing net magnetization. Applying the strain in the (001) plane would distort the crystal, inducing a transition into a tetragonal symmetry, ultimately modifying the magnetic and structural properties; adding a weak-ferromagnetic canting into the magnetic response [42]. As the ferromagnetic contribution to the AHC can not be separated from the topological contribution, it is impossible to distinguish the nature of the AHC source in the distorted tetragonal structure. Therefore, a symmetry–preserving straining process is required to examine the AHC controllability and its source in Mn_3NiN properly. So far, it is possible to experimentally explore the effect of the strain on antiferromagnetic nitride antiperovskites such as Mn_3GaN and Mn_3NiN; epitaxial growth of thin films of antiperovskites onto perovskites, $SrTiO_3$, has been achieved experimentally [152, 153]. Furthermore, the epitaxial growth of Mn_3NiN on the piezoelectric $BaTiO_3$ [154] has already been achieved, showing the sensitivity of the AHC to the strain. Notwithstanding these efforts, there is still more room to explore the controllability of the AHC through the strain and the origin of its behavior more profoundly. In this chapter, a first-principles study of the symmetry–preserving epitaxial strain as a control mechanism of the electronic properties is performed. Furthermore, the AHC and the Berry curvature, BC, features are explored in the antiferromagnetic antiperovskite Mn_3NiN as a prototype among the Mn_3BN family. Thus, our results explain the physical origin of the AHC controllability and possible experimental tuning.

4.2 Computational and Theoretical Details

We performed first-principles calculations within the density-functional theory (DFT) [121, 89] approach by using the VASP code (version 5.4.4) [45, 46]. The projected-augmented waves scheme, PAW [122], was employed to represent the valence and core electrons. The electronic configurations considered in the pseudo-potentials, as valence electrons, are Mn: ($3p^6 3d^5 4s^2$, version 02Aug2007), Ni: ($3p^6 3d^8 4s^2$, version 06Sep2000), and N: ($2s^2 2p^3$, version 08Apr2002). The exchange-correlation was represented within the generalized gradient approximation GGA-PBEsol parametrization [94]. The Mn:$3d$ orbitals were corrected through the DFT+U approximation within the Liechtenstein formalism [123]. Due to the strong magnetostructural response observed in the Mn_3BN antiperovskites [13], we used the $U = 2.0$ eV parameter in the Mn:$3d$ orbitals. This U value allows the structural optimization to reproduce the experimentally observed lattice parameter, which is crucial in obtaining an appropriate charge distribution and, ultimately, the electronic properties under strain. Moreover, the electronic structure of Mn_3NiN obtained with PBEsol+U is compared with the computed by the strongly constrained and appropriately normed semilocal density functional, SCAN, [95, 114], observing a fair agreement of the electronic structure in both cases. Importantly, recent reports of SCAN-based calculations have shown results in good agreement with the experimental reports, including the lattice parameter [124, 125], and the magnetic and the electronic structure [112] in strongly-correlated $3d$ perovskites and Heusler Mn-based alloys [126]. All the procedures described above are essential due to the needed accuracy related to the lattice degrees of freedom as a function of the applied strain and its effect on the magnetostructural behavior. The periodic solution of the crystal was represented by using Bloch states with a Monkhorst-Pack [127] k-point mesh of 12×12×12 and 600 eV energy cut-off to give forces convergence of less than 0.001 eV·Å^{-1} and an error in the energy less than 10^{-6} eV. The spin-orbit coupling (SOC) was included to consider non-collinear magnetic configurations [128]. The anomalous Hall conductivity, and associated observables, were obtained with the Python library

WannierBerri [102] using the maximally localized Wannier functions and the tight-binding Hamiltonian generated with the Wannier90 package [101]. The interpolation was performed with 80 Wannier functions with projections on the *s*,*p*,*d* orbitals for the Mn and Ni atoms and *s*,*p* for N atoms. For the disentanglement process, we used an energy window +3.0 eV higher than Fermi level as the maximum, and none for the minimum, and a convergence tolerance of 5.0×10^{-8} Å^2. With the support of the WannierTools code [155], the number of band crossings around the Fermi energy was obtained for the range between -1.3 to 1.3 eV, as well as their position in energy and momentum. The latter considers an energy-gap crossing (E_w) below the threshold of $E_w = 0.050$ eV computed in a $17\times17\times17$ k-mesh.

The atomic structure figures were elaborated with the VESTA code [129]. Finally, the band structure was analyzed with the Python library PyProcar [130].

4.3 Structure and Magnetism in Mn_3NiN

A symmetry analysis in the FINDSYM [156, 157] portal revealed a rombohedral symmetry after the structural optimization in the unstrained Mn_3NiN structure shown in Fig 4.1(a), which appears cubic at plain sight. Small off-axis components of order $\sim 10^{-3}$ Å where observed in the lattice vectors; presumably an effect of the magnetic interactions between the two magnetic kagome lattices. Moreover, the symmetry in the Γ_{4g} magnetic phase of Mn_3NiN is imposed by the magnetic sublattice which reduces the symmetry of the system from cubic to rombohedral and allows the existence of topological phenomena. As briefly stated in the introduction, avoiding additional contributions induced by structural phase transitions that might be enforced by the strain application in the (001)-plane of the rombohedral 5-atom reference (depicted in Fig 4.1(a)) is essential to explore the symmetry induced AHC. Each symmetry group has an associated AHC tensor σ_{ij}^{AHE} with its corresponding non-zero components. Thus changing the symmetry modifies not only the magnitude of the components but also the form of the AHC tensor, potentially introducing finite values in components absent

before the strain. As the magnetic moments of the Γ_{4g} magnetic phase are coplanar along the (111) plane, with the magnetic symmetry axis pointing in the [111] direction, the only symmetry–preserving straining process is the biaxial strain in the (111) plane. Therefore, to keep the system in the R$\bar{3}$m' symmetry, the epitaxial strain was applied along the (111)-plane so that the kagome lattice, the magnetism, and their associated symmetry conditions are preserved.

The process to apply the strain in the (111) oblique plane of the 5-atom reference will be described. The kagome lattice, formed by the Mn atoms present in the (111)-plane and its spatial orientation highlighted in a yellow plane, is shown in Fig. 4.1(b). First, as the *Vienna Ab-initio Simulation Package* is unable to apply strain in an oblique plane, the structure was rotated to orientate the (111) plane parallel to the cartesian xy-plane as shown in Fig. 4.1(c). After the rotation, an equivalent 15-atom hexagonal cell shown in the same figure is obtained as the unit cell. In this new representation, the structural symmetry allows the homogeneous application of the epitaxial strain. Here, applying biaxial strain in the xy-plane is equivalent to homogeneously straining the kagome lattice; thus the two independent lattice directions serve as the crystallographic directions to apply the epitaxial strain. As observed in Fig. 4.1(d), stretching the structure homogenously along the kagome plane would only change the Mn–Mn distance, not the atomic arrangement. The latter results in control over the magnitude of the exchange and the superexchange interactions by modifying only the interatomic distances while preserving the magnetic symmetry.

Punctually, the straining process was performed as follows. The a lattice parameter is variated along with the values from –3% to +3%, while allowing the complete relaxation of the crystal structure and atomic positions along the perpendicular c direction in all cases to obtain the ground state under strain. In this case, the strain percentage, η, characterizes a deviation of the current lattice parameter a from the unstrained lattice parameter a_0 as:

$$\eta = \frac{a - a_0}{a_0} \times 100\%, \tag{4.1}$$

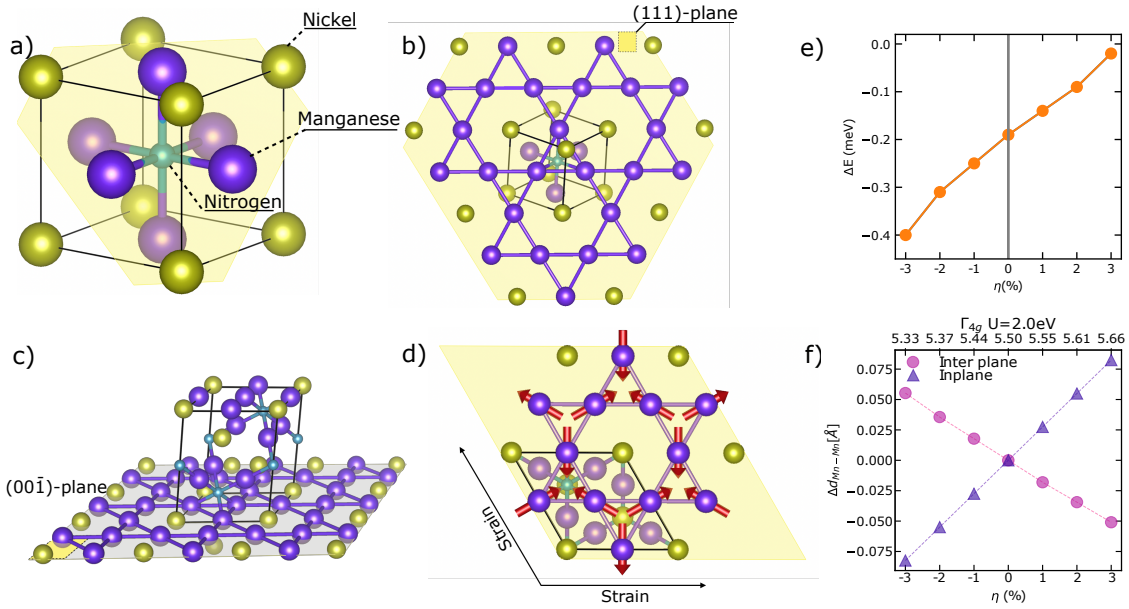

Figure 4.1: *(a) Mn_3NiN rombohedral structure showing the Mn, Ni, and N atoms in violet, yellow, and green colors, respectively. Here, the (111)-plane is shown in yellow color. (b) The kagome lattice, on the (111)-plane formed by the Mn atoms, is highlighted on top of the unit cell of Mn_3NiN. (c) 15-atom hexagonal reference obtained after rotating the 5-atom structure, aligning the (111)-plane kagome lattice with the xy-plane. (d) Noncollinear antiferromagnetic Γ_{4g} ordering, in which the magnetic moments per atom are depicted in red. Additionally, the kagome lattice and the schematics of the strain application are also shown. (e) Ground state energy difference, $\Delta E = E_{\Gamma_{4g}} - E_{\Gamma_{5g}}$, versus the applied epitaxial strain suggesting lower energy for the Γ_{4g} in each case. (f) Variation of the inter-plane and in-plane Mn–Mn distances as a function of the epitaxial strain.*

as such, the above relationship, Eq. 4.1, translates into compression for negative values of η and tension for positive values of the variable.

Anticipating the intimately entangled nature of the electronic, magnetic, and crystalline structures of Mn_3NiN, the atomic cell was carefully optimized within the PBEsol+U approximation. Thus the e–e interaction was tuned through the Hubbard U parameter to reproduce the experimental unstrained cell lattice constant (a_0 = 3.886 Å below T_N = 262 K) [158] were the Γ_{4g} magnetic ordering had been found stable. As a result, a relaxed structure in agreement with the available experimental reports was found, ready to be strained. After testing for a variety of U values, within the range [0,3] eV (see Table 4.1), U = 2.0 eV resulted as the best setup to obtain the desired lattice parameter accurately. Under the selected U correction, the 15-atom

Table 4.1: *Lattice parameter vs Hubbard correction in PBEsol+U for Mn_3NiN. The selected U to reproduce the experimental value is highlighted.*

U	Lattice parameter
0.0	3.74524
1.0	3.82126
2.0	3.88535
3.0	3.94635

reference (hexagonal cell) was obtained with the parameters of a = 5.496 Å and c = 6.726 Å with the stable Γ_{4g} magnetic ordering. In the equivalent 5-atom reference, the lattice parameter turned out as a_0 = 3.885 Å. This way, a pre-strained setup as in the case of pure LDA/PBE–based calculations was avoided; approximations that under/overestimate the experimentally observed lattice value respectively[125]. Importantly, there is a strong link between the electronic and lattice degrees of freedom in Mn-based compounds [114, 112], which in some cases might induce structural instabilities. Additionally, the full phonon dispersion was obtained for the unstrained

structure and the -3.0%, and $+3\%$ strain cases to ensure no imaginary vibrational modes along the straining process (see Fig. 4.2). Thus, guaranteeing the structural stability of the Γ_{4g} phase of Mn_3NiN and avoiding a strain-induced structural phase transition.

Furthermore, a comparison of the ground state for the Γ_{4g} against the Γ_{5g} was realized (see Fig. 4.1(e)) to test the stability of the mirror symmetry broken Γ_{4g} over the mirror-symmetric Γ_{5g} magnetic phase. As such, the results indicate a reinforcement of the Γ_{4g} over the Γ_{5g} with the application of the compression strain, establishing the negative strain values as a mechanism to keep the Mn_3NiN in the Γ_{4g} magnetic phase. Experimental reports, supported on the similar magneto-crystalline anisotropy energy (MAE) in the unstrained structure, indicate a mixture of both Γ_{4g} and Γ_{5g} magnetic phases in Mn_3NiN [159, 160, 161]. Nonetheless, in agreement with our results in Fig. 4.1(e), a more recent report of the magnetism in Mn_3NiN points towards the Γ_{4g} ordering as the preferred state [12] under compressive strain values. Moreover, as already discussed in the introduction, the structural phase transition to the tetragonal phase induced by the strain in the (001) plane adds a weak ferromagnetic component perpendicular to the kagome lattice. Therefore, the possibility of an off-plane ferromagnetic canting along the (111)-axis was explored. Nevertheless, a complete atomic and electronic relaxation under strain eliminated the introduced canting, arriving at a coplanar configuration of the magnetic moments in the (111) plane; the lattice of the Mn_3NiN antiperovskites is dynamically unstable at the FM state along the (111)-axis, an imaginary phonon at the R-point related to out-of-phase octahedral rotations has been reported [114]. In Fig. 4.1(f), the variations of the plane-to-plane distance between the kagome planes as a response to the variations of the distance between two Mn nearest atoms of the same plane, are shown. There, it can be observed how the application of compression (tension) on the plane of the magnetic kagome lattice is equivalent to increasing (decreasing) the separation of the (111) family of planes. Furthermore, in Fig. 4.1(f) can be observed how linear variations of the distance between Mn atoms of the same plane produce inverse linear variation in the separation of the kagome planes.

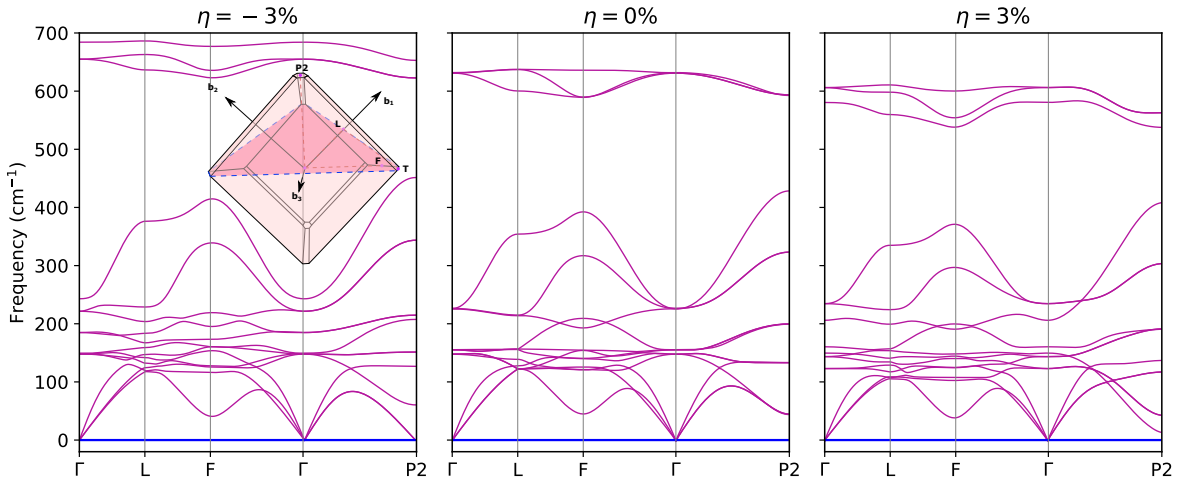

Figure 4.2: *Full phonon dispersion for the η = −3, 0, +3% strain cases in Mn_3NiN. The Brillouine Zone is embedded to illustrate the position of the high symmetry point with regard to the 111 plane.*

Consequently, the frustration mechanism can be controlled through the exchange and superexchange magnitude tuning with the strain. Thus, the advantage of straining in the (111) plane is the preservation of the symmetry due to the undistorted result in each strain case, keeping the initial $R\bar{3}m$' symmetry intact along the deformation path on the 15-atom reference. Therefore this strain methodology only modifies the electronic and exchange effects by controlling the distances between the Mn atoms. The latter permits the observation of the AHC behavior as a pure function of the strain with no additional components. Additionally, as the symmetry is not changed, it is possible to make the straining and optimizing on the 15-atom reference and then recover the 5-atom representation to perform the rest of the calculations and analysis, avoiding electronic bands unfolding issues. To recover the 5-atom representation, the transformation matrices, as implemented in the FINDSYM tool [156, 157], were used. In what follows, all the calculations and analyses related to the 5-atom reference for each strained and relaxed cell.

4.4 Electronic Structure

The currently accepted approach to the AHC understanding in non-collinear antiferromagnets relays on a non–vanishing BC at the Fermi level. The BC, being a result of the electronic structure, is affected by band interactions (*i.e.,* band coherences) and topologically protected band degeneracies called Weyl nodes. The electronic band structure and the Berry curvature calculated along the Γ–L–T–Γ–F, and P2–Γ paths in the BZ for the $\eta = -3.0\%$, 0.0%, and +3.0% in the 5-atom reference are presented in Fig. 4.3(a-c). In the figure, two relevant Weyl nodes W_1 and W_2 near Fermi in the T–Γ path marked inside black circles. Expectedly, the bands in the L–T path, which lies parallel the (111)-plane (where the kagome lattice lies), and the bands in the perpendicular P2–Γ path, present inverse behaviors; compression, push away the energy bands close to the Fermi energy in the L–T path (see Fig. 4.3(a)). On the other hand, in the P2–Γ path, shown in the same figure, electron bands are displaced to higher energy values together for the same compression case. Moreover, under tension, the electronic band structure displays the opposite behavior, as observed in the $\eta = +3\%$ case shown in Fig. 4.3(c). the second row of Fig. 4.3(a-c), the BC for the same path of the band structure is included. Interestingly, in the L–T path, the BC shows a non-divergent and spread behavior; meanwhile, in all the remaining paths, the BC is either vanishingly small or very localized and divergent. The discontinuous BC is a characteristic of the band degeneracies (*i.e.,* band crossings) located near the Fermi level. As such, band crossings displace energy as a function of the epitaxial strain following the band structure behavior. However, not all the crossings remained unaltered and were broken due to the strain; in this case, the degeneracy is said to be of trivial nature. In general, there are more crossings above Fermi for compression, while the majority lie below the same energy level for tension. The unstrained structure presents most of the crossings on the Fermi level or very close to it. Later in the text, we will discuss this observation in contrast to the AHC results.

A projection of the band structure per atomic species for $\eta = -3.0\%$, 0.0%, and 3.0%

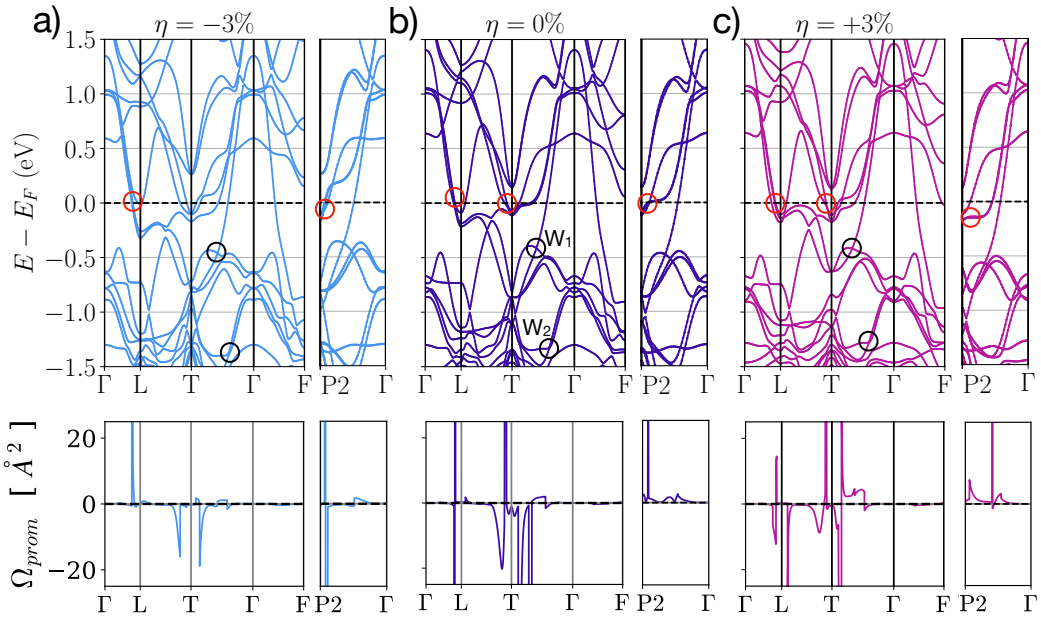

Figure 4.3: *(a-c) Electronic band structure (first row) and Berry curvature (second row) of the Mn_3NiN in the Γ_{4g} noncollinear magnetic phase. Here, marked in a black circle is presented a Weyl node close to the Fermi level in the T–Γ path as well as for non-topological band crossings in red circles.*

is presented in Fig. 4.4. In there, the Mn:3*d*-states represent the major contribution for energies higher than the Fermi level. The bands below the Fermi level are dominated mainly by the Ni:3*d*-states, with the most substantial component around -1.25 eV.

The intermediate zone $-0.5 \leq \mathrm{E} \leq +0.5$ eV is a common place where both atomic species Mn and Ni share dominance over the band structure. Thus, a hybridization of the Mn and Ni *d*-orbitals is occurring, shaping the conduction phenomena and the magnetism at the same time. Such configuration, known as itinerant magnetism, consists of electrons participating in the conduction phenomena and the magnetism of the crystal.

Being a conduction phenomenon, the AHC might depend on the number of states available near the Fermi energy. Aiming to analyze the available charge and states around the Fermi level, we computed the DOS for $\eta = -3\%$, 0%, and +3% and the results are contained in Fig. 4.5(a-c). Here, a displacement of the total DOS with respect to the energy as a response to the applied strain was observed. Tracking the minimum of the DOS, located at -0.5 eV in the $\eta = 0.0\%$ DOS plot in Fig. 4.5(b), which moves up (down) in energy for compression (tension), this behavior becomes apparent. More precisely, the available states near the Fermi level decrease with compression and increase with tension, as seen in Fig. 4.5(d). To further dive into the DOS subtleties around the Fermi level, the Mn and Ni:3*d*-orbitals projections of the DOS are included in Fig. 4.5(a-c). As it can be observed, the contribution at the Fermi level from the $3d_{xy/yz/xz}$ orbitals increase (decrease) for tension (compression) strain values. The same is the case for $3d_{z^2/x^2-y^2}$. In general, the 3*d* orbitals are pushed upwards in energy when the structure is compressed. In the case of Ni:3*d* orbitals, a marginal contribution is observed close to the Fermi level. Finally, the direct integration of the total DOS for each η in the [−0.1,+0.1] eV interval, as presented in Fig. 4.5(d), confirms the relationship between the electronic states and the strain inferred from the complete and partial DOS analysis. Moreover, the integration of the DOS over the ranges [−0.1,0.0] and [0.0,+0.1] eV for the occupied and unoccupied bands, respectively, follow the same behavior already observed in the [−0.1,+0.1] eV

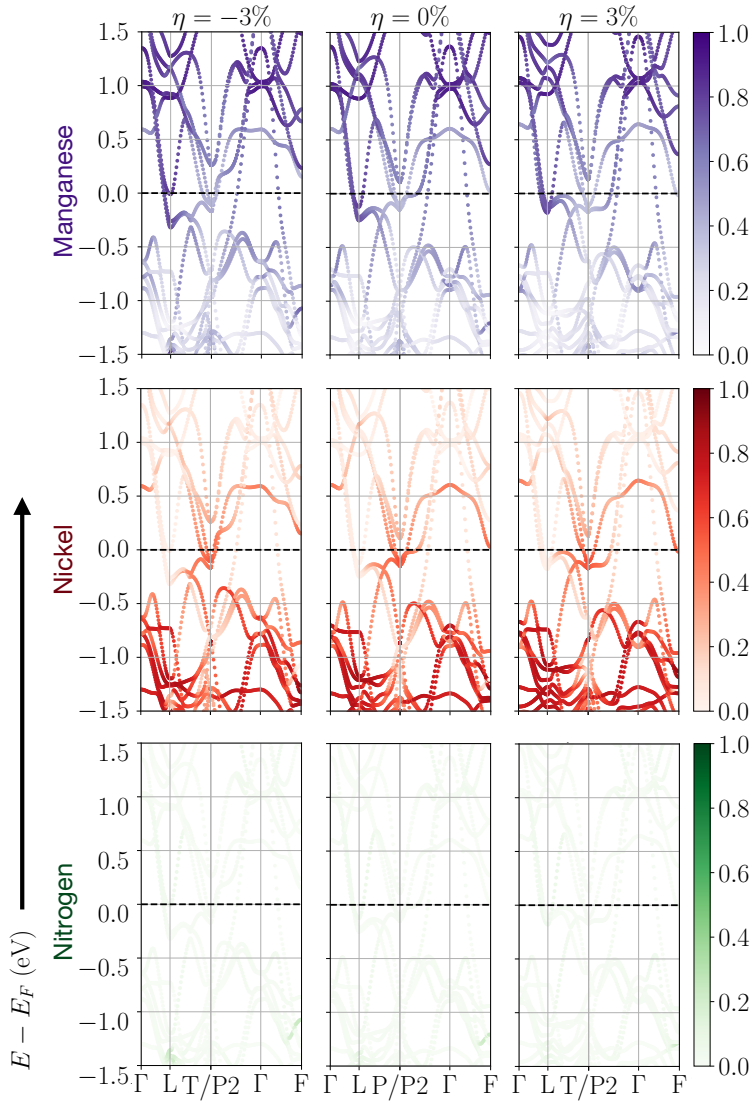

Figure 4.4: *Projections per atomic species of the band structure in Mn_3NiN for each case of strain.*

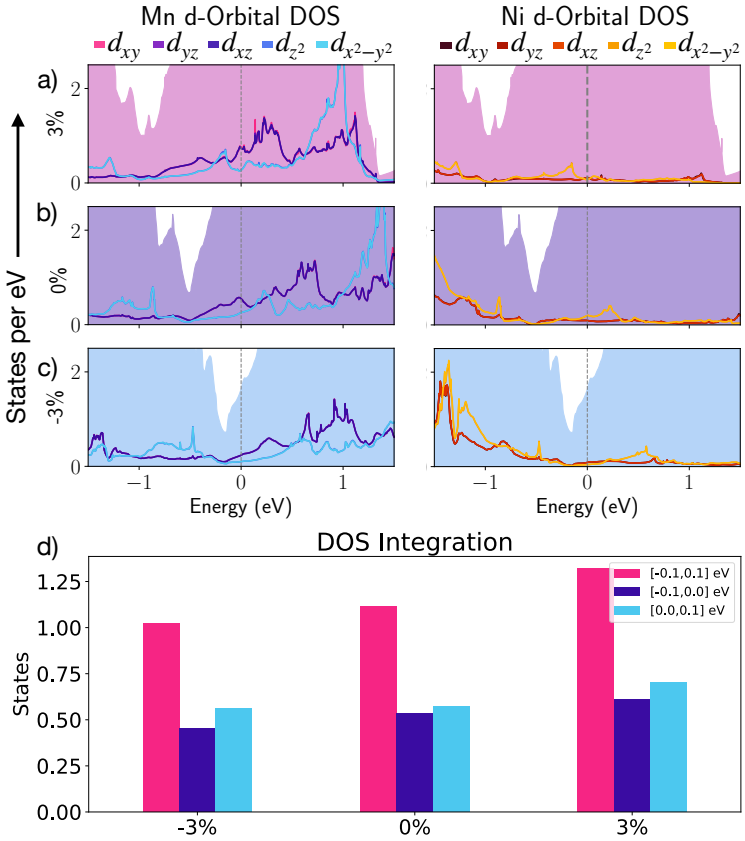

Figure 4.5: *(a-c) Density-of states, DOS, for the* -3.0%*,* 0.0%*, and* $+3.0\%$ *strain values including the d-orbitally projected Mn and Ni states. (d) DOS states integration for an energy range of 0.1 eV under, over, and around the Fermi energy.*

interval.

4.5 Anomalous Hall conductivity

The AHC can be the outcome of various sources: the intrinsic, side jump, and the skew scattering contribution, as shown in Ref. [146]. The last two of them are a consequence of impurities in the crystal that deflect and scatter the electrons sideways. In this work, attempting to understand the topological nature of the AHC, only the intrinsic component will be the study subject. As the intrinsic AHC results from the electronic, magnetic, and structural properties of a perfect crystal, it is their balance that builds

the properties of the space around the charge carriers. Additionally, the intricate combination of the many interactions in the frustrated triangular shape created between the Mn atoms in the kagome plane reduces the symmetry to $R\bar{3}m$ in the Γ_{5g} case. On the other hand, in the case of the Γ_{4g} magnetic ordering, shown in Fig 4.1(e), the $\mathcal{M}$-symmetry is also removed, ending up with the $R\bar{3}m$' symmetry. The removal of $\mathcal{M}$-symmetry is essential for the unbalanced Berry curvature, resulting in the existence of AHC in the Γ_{4g} phase. For the same reason, the $\mathcal{M}$-symmetry present in the Γ_{5g} forbids the AHC.

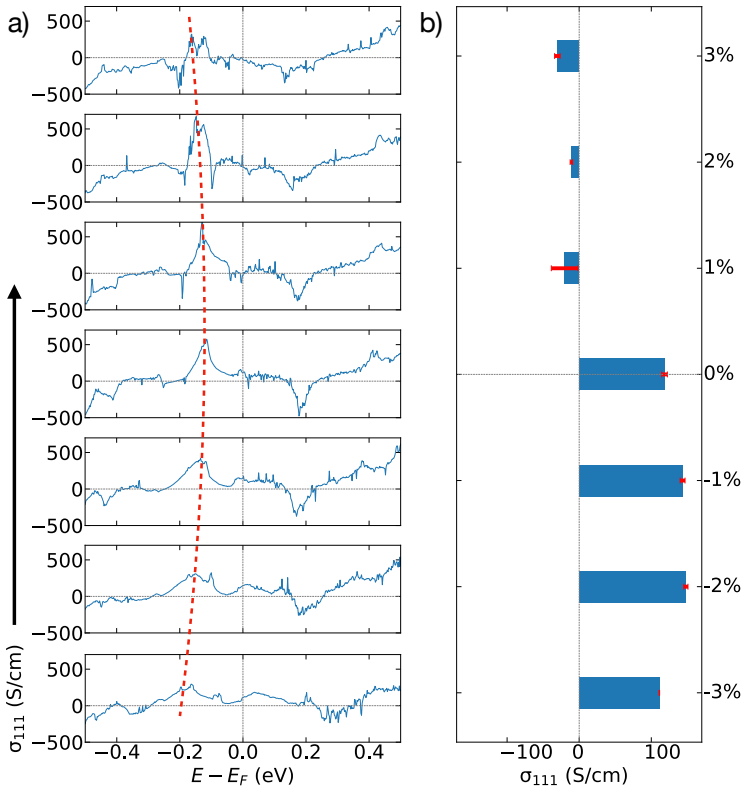

Figure 4.6: *(a) Anomalous Hall conductivity as a function of energy for various strain values. The AHC around − 0.2 eV shows a downward shifting behavior marked with a red dashed line for compression and tension strain values. (b) AHC value extracted at Fermi energy, including the error estimated as the standard deviation of the last 20 computational iterations.*

The AHC behavior as a function of the epitaxial strain should relate to the response

of both or any of those properties. The Γ_{4g} phase of the Mn_3NiN system is a non-collinear antiferromagnet; each Mn atom possesses a non-zero magnetic moment, but the net magnetization of the unit cell is zero. Consequently, in the absence of an internal or external magnetic field, the Hall conductivity must result from the anomalous Hall effect (AHE) through a non-vanishing Berry curvature, as in Eq. 3.1. In this case, the AHC for the $R\bar{3}m'$ magnetic symmetry group can be written as the following tensor [162, 40]:

$$\sigma_{\Gamma_{4g}} = \begin{pmatrix} 0 & \sigma_{xy} & -\sigma_{xy} \\ -\sigma_{xy} & 0 & \sigma_{xy} \\ \sigma_{xy} & -\sigma_{xy} & 0 \end{pmatrix} \tag{4.2}$$

with the magnitude of all the non-zero components identical $\sigma_{xy} = \sigma_{zx} = \sigma_{yz}$ and therefore written all in terms of the σ_{xy} component. The strain application process proposed in this work now reveals its advantages by guaranteeing a fixed AHC tensor form and symmetry conditions, as seen in Eq. 4.2. As such, the setup for the strain, as seen in Fig. 4.1(e), is the key to studying the AHC in Mn_3NiN as a pure function of the strain without altering the allowed symmetry features. Then, the variations on the AHC in the (111)-plane $\sigma^{\eta}_{111} = \frac{1}{\sqrt{3}}(\sigma^{\eta}_{xy} + \sigma^{\eta}_{yz} + \sigma^{\eta}_{zx})$ can be extracted as a function of η in the kagome lattices. Fig. 4.6(a) shows the σ_{111} component of the AHC as a function of the energy, in the energy range $[-0.5,+0.5]$ eV, for strain values between $\eta = -3.0\%$ to 3.0%. In Fig. 4.6(b) is presented a bar plot condensing the σ_{111} value at the Fermi level for each strain value, as well as their error bars. The latter error bars, marked in red in Fig. 4.6(a), were estimated as the standard deviation of the last 20 adaptive refinement iterations [102] while computing the σ^{AHE}_{xy} component based on the Eq. 3.1. A considerably large error bar can be observed in the case of $\eta = +1\%$ which is the consequence of a rapidly varying BC which in turns produces wide variations in the AHC results between successive mesh refinements in the interpolation for the AHC integral calculation. Interestingly, the AHC behavior turned out to be more complex than expected; its value does not just increase or decrease with the epitaxial

strain. As seen in Fig. 4.6(a), the whole function is flattened with the compressive and tensile stress incremental. Additionally, the maxima and minima of the conductivity function diverge away from the Fermi level with both types of deformation, rendering unfeasible the possibility of tuning the position of these points to maximize the AHC. Furthermore, as seen in the barplot of Fig. 4.6(b), the tensile strain greatly disrupts the AHC, stretching the (111)-plane as low as $\eta = +1\%$ and upwards reduces the conductivity dramatically. The AHC for the compression case shows a fascinating behavior with three different phases. Initially, compression strain induces an increase of the AHC from $\sigma_{111}^{0\%} = 114$ S·cm^{-1} to $\sigma_{111}^{-1\%} = 144$ S·cm^{-1} representing an increase of 26%. However, after this phase, the AHC remains constant in a plateau zone that holds until $\eta = -2\%$. After this point, further compression does not enhance the AHC; instead, the conductivity drops after this strain value, reaching $\sigma_{111}^{-3\%} = 111$ S·cm^{-1} for $\eta = -3\%$, returning to a value similar to the unstrained case $\eta = 0\%$. Looking at Fig. 4.6(a), a small spike of AHC can be spotted just under the Fermi level for $\eta = 0.0\%$. Following a similar trend as has already been observed for the AHC under strain, the mentioned spike disappears for tension but enhances under compression. Noteworthy, this spike grows non-stop along the $0\% \geq \eta \geq -2.0\%$ interval. Moreover, the mentioned spike moves up to energies higher than the Fermi level, being its maximum synchronized with the Fermi level for a compressive η between -1.0% and -2.0% Thus, our findings suggest that the AHC function is not shifting in energy; its behavior under string is more appropriately described as a redistribution of the area under the AHC curve with the strain. Taking the AHC formula, Eq. 3.1, into account and aiming to anchor the AHC strain response to a satisfactory explanation, the $\sigma_{111}^{-1.5\%}$ and the Berry curvature were calculated. The conductivity for the additional strain value turned out as $\sigma_{111}^{-1.5\%} = 141$ S·cm^{-1}, confirming the plateau zone previously mentioned. Here, some saturation is occurring that is stable within $-1\% \geq \eta \geq -2\%$. Surprisingly, a comparison between the AHC (in Fig. 4.6) and the states available near the Fermi level (see Fig. 4.5(d)) within the range [−0.1,+0.1] eV, directly associated with $f_n(\vec{k})$, in Eq. 3.1, shows no correlation. This result was unexpected because of

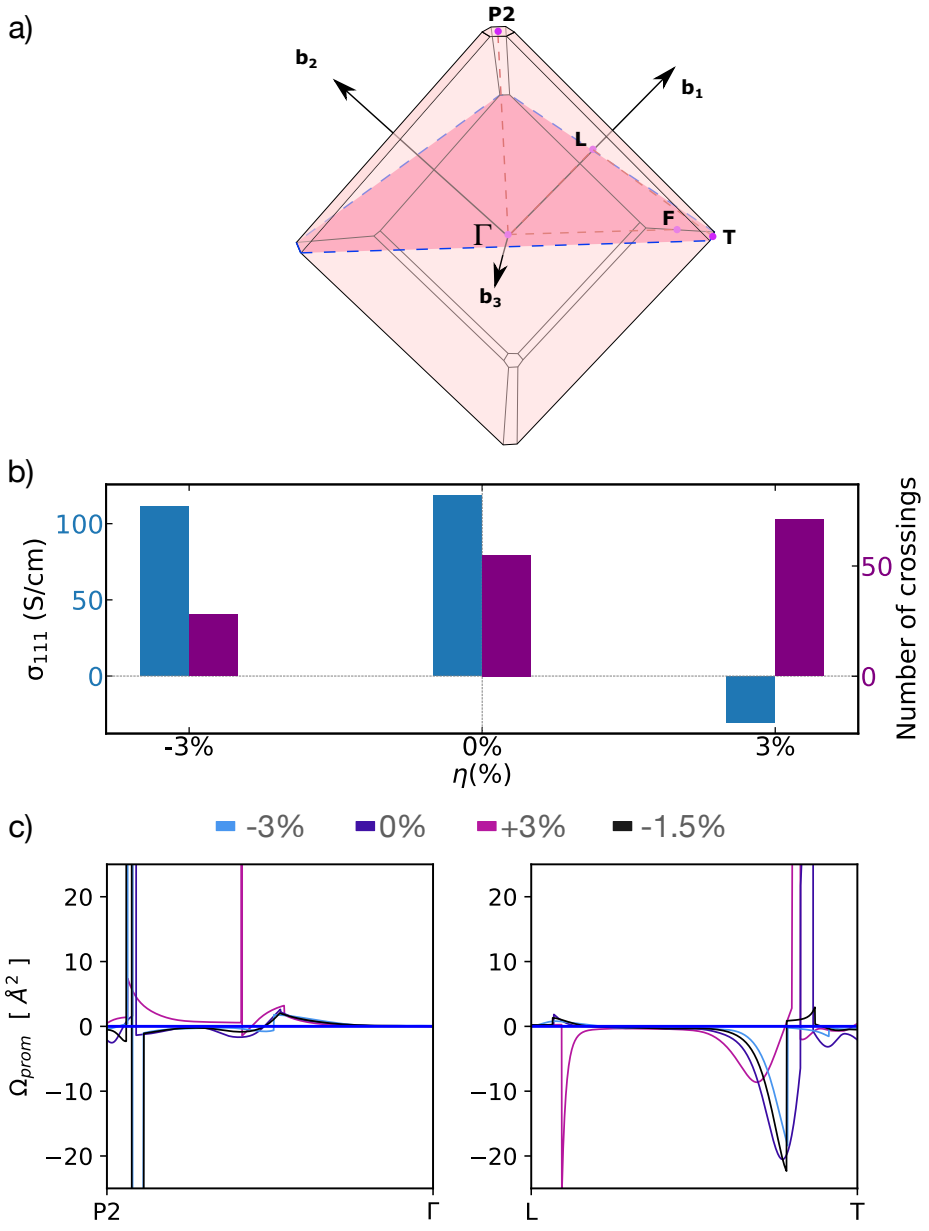

Figure 4.7: *(a) Brillouin zone for the rhombohedral structure of Mn_3NiN. Here, the plane parallel to the (111)-plane, and the high symmetry points included in the band structure calculation are highlighted. (b) Bar plot including the σ_{111} component of the AHC as well as the number of non-topological band crossings in the range [−0.1,0.1] eV around the Fermi level. (c) Berry curvature calculated for the path connecting the high symmetry points* P2–Γ *on the left and* L–T *on the right, perpendicular and parallel to the kagome lattices, respectively.*

the appearance of the Fermi distribution inside the integral for the AHC; a connection between the conductivity property and the charge carriers distribution at the Fermi level was anticipated. However, the data showed the opposite behavior; as the number of states increased with tension, the AHC gets almost destroyed. Compression strain, however, induced an inverse response, fewer states were available around the Fermi level, but a higher anomalous conduction magnitude occurred. A DOS projection onto the Mn:3*d* and Ni:3*d* orbitals, which dominate most of the band structure around the Fermi level, showed a non-similar behavior to the AHC. The contribution of those orbitals follows the same rules as the total DOS, already discussed in the electronic structure analysis. The final resource of control to investigate and the most relevant to the AHC is the Berry curvature. The Berry curvature results and their implications and correlation with the AHC will be analyzed in what follows. The Mn_3NiN BZ is shown in Fig. 4.7(a) in which P2–Γ and L–T are shown with respect to the (111)-plane kagome lattice. In Fig. 4.7(b) is presented the AHC as well as the number of band crossings in the [-0.1,0.1] eV range as a stacked bar plot. The BC integration results for $\eta = -3.0\%, -1.5\%$, 0.0%, and 3.0% along the P2–Γ and the L–T paths are shown in the left and right parts of Fig. 4.7(c), respectively.

The BC has two sources that produce curvature of different natures: the bands crossings and the band interaction. The BC produced by the bands crossings is highly localized and divergent, and the BC produced by the bands interactions is more spread and non-divergent. Therefore, the BC source can be identified by comparing the electronic band structure and the BC along the same path in the BZ. For instance, the BC along the P2–Γ path shown in Fig. 4.7(c) displays various discontinuities associated with band crossings near and at the Fermi level. However, not all the bands crossings are the same; some arise as a consequence of the topology, while most are trivial. A symmetry analysis included later in this text corroborates that most of those crossings are not protected by the symmetries of the system and therefore belong to the non-topological band crossings classification.

Of course, if a band crossing is induced by the topology (i.e., Weyl node), it can not

be destroyed by any other means than a change in the topology. Therefore, to remove a degeneration such as bands crossing protected by the topology, the symmetry of the system must be altered. Here again, the rhombohedral symmetry preservation throughout the strain application process is advantageous because the number and approximate location of the Weyl nodes are preserved. In this case, the strain allows the shape of the band structure to remain mostly unaltered. As a result, the topological band crossings can only move up and down in energy, and the non-topological band crossings are subject to being dissolved by external perturbations. Notably, the trivial bands crossings near the Fermi level (shown in Fig. 4.3(a-c)) produce a divergent component of the BC that is maximum for the unstrained structure, very weak for compression but considerable for tension strain. Despite that, the highest AHC values were obtained for compression and the unstrained cases, while the minimum AHC is obtained for tension strain. Thus rendering unrelated the highly localized BC of the non-topological bands crossings and the AHC. Moreover, the counting of the band crossings near the Fermi energy shown in Fig. 4.7(b), in agreement with the DOS integral, shown in Fig. 4.5(d), displays a proportional compression (tension) to decrease (increase) of the number of crossings. Thus, giving more crossings near the Fermi level for tension than for compression and an intermediate number of crossings for the unstrained case. Again, the Berry curvature of the non-topological crossings does not follow the behavior already seen in the AHC. Therefore, in agreement with Huyen *et al.* [151], our results suggest that the highly localized and divergent contribution to the Berry curvature, induced by the bands crossings near the Fermi level, is not the AHC primary origin.

4.6 Weyl nodes in strongly correlated and magnetic systems

As has already been commented, not all bands crossings are actual Weyl nodes. On the contrary, most of them are non-topological crossings, non-topological or trivial bands crossings resist small symmetry-preserving perturbations but will most certainly break under a considerable strain perturbation; they do not result from the symmetry, so they are not protected by any means. In what follows, the Weyl nodes identification process will be presented.

The electronic band structure is usually spanned in Bloch functions which are unlocalized functions that live in the momentum. However, it is possible to span the band structure in a set of localized functions in the real space known as the Wannier functions. Therefore, thanks to the link between the Bloch and Wannier functions, a relationship between the localized orbitals of atomic sites with the wave functions can be established [163, 164]. In this case, the Hamiltonian inherits the symmetry of the crystal and, with them, the protected degeneracies in the high symmetry paths in the Brillouine Zone. To obtain such paths, the compatibility relations between the high symmetry points must be extracted from the character tables of the high symmetry points. There, the relevant paths are spotted because of the non-symmorphic symmetry (e.g., the roto-translations) they hold, hosting symmetry-protected Weyl nodes. The character tables and the compatibility relations for the R-3m' (166.101) magnetic symmetry group were obtained from the Bilbao crystallographic server, tabulating such information for all the known symmetry groups. Such tables were calculated through a generalized implementation of the induction algorithm based on the Frobenius reciprocity [165, 166].

The TRS breaking relives the bands degeneracy in systems such as the Γ_{4g} magnetic phase of Mn_3NiN that would otherwise be degenerate for the spin up and down components. However, some degeneracies that arise from the non-symmorphic symmetries can not be removed by this symmetry breaking due to their topological origin, which

Table 4.2: *Compatibility relations in the* Γ-T *path*

Compatibility relations for Γ	Intermediate path	Compatibility relations for T
$\Gamma_1^+(1) \rightarrow \Lambda_1(1)$		$T_1^+(1) \rightarrow \Lambda_1(1)$
$\Gamma_1^-(1) \rightarrow \Lambda_1(1)$		$T_1^-(1) \rightarrow \Lambda_1(1)$
$\Gamma_2^+(1) \rightarrow \Lambda_2(1)$		$T_2^+(1) \rightarrow \Lambda_2(1)$
$\Gamma_2^-(1) \rightarrow \Lambda_2(1)$		$T_2^-(1) \rightarrow \Lambda_2(1)$
$\Gamma_3^+(1) \rightarrow \Lambda_3(1)$		$T_3^+(1) \rightarrow \Lambda_3(1)$
$\Gamma_3^-(1) \rightarrow \Lambda_3(1)$	Λ	$T_3^-(1) \rightarrow \Lambda_3(1)$
$\bar{\Gamma}_4(1) \rightarrow \bar{\Lambda}_4(1)$		$\bar{T}_4(1) \rightarrow \bar{\Lambda}_4(1)$
$\bar{\Gamma}_5(1) \rightarrow \bar{\Lambda}_5(1)$		$\bar{T}_5(1) \rightarrow \bar{\Lambda}_5(1)$
$\bar{\Gamma}_6(1) \rightarrow \bar{\Lambda}_6(1)$		$\bar{T}_6(1) \rightarrow \bar{\Lambda}_6(1)$
$\bar{\Gamma}_7(1) \rightarrow \bar{\Lambda}_4(1)$		$\bar{T}_4(1) \rightarrow \bar{\Lambda}_4(1)$
$\bar{\Gamma}_8(1) \rightarrow \bar{\Lambda}_5(1)$		$\bar{T}_5(1) \rightarrow \bar{\Lambda}_5(1)$
$\bar{\Gamma}_9(1) \rightarrow \bar{\Lambda}_6(1)$		$\bar{T}_6(1) \rightarrow \bar{\Lambda}_6(1)$

protects them against symmetry-preserving perturbations. According to the compatibility relations, the $C_{3(111)}$ symmetry in this non-collinear antiferromagnet induces a total of 6 possible Weyl nodes located along the path Γ:(0,0,0)$\rightarrow$ T:(1/2, 1/2, -1/2). Each Weyl node is conformed by a crossing between a pair of bands from the Γ point at an intermediate Λ point, after which the bands separate again towards the point T (see Table 4.2).

The protected status of the Weyl nodes means that they are resistant to all the symmetry-preserving perturbations in the system and invulnerable to the SOC. The SOC often removes accidental bands crossings unrelated to a non-symmorphic symmetry. Therefore, true Weyl nodes hold against small or extreme strain values, such as $-3\% \leq \eta \leq +3\%$, either in the presence or the absence of the SOC, whenever the symmetry/topology are the same before and after the strain. Here, the symmetry

analysis provides information about the path where the Weyl is located but not about the exact location in the Brillouine zone or the energy at which it occurs. Therefore, a direct check of the band structure must be performed to localize the Weyl nodes to confirm the band inversion characteristic of these degeneracies and their robustness against the strain. After analyzing the band structure in the T-Γ path, looking for band degeneracies with band inversion, we spotted some crossings that disappear under compression or tension, but four crossings hold from –3% to +3% strain (see Table 4.3). In figure 4.8, the spin projected band structure for Mn_3NiN plotted in PyProcar [130] is shown for each strain case to observe the band inversion characteristic of the Weyl nodes in the T-Γ path and their invulnerability against the strain. Among the

Table 4.3: *Weyl nodes with energy E (eV) and coordinates $\vec{b}$ ($Å^{-1}$) in the BZ along the Γ:(0, 0, 0)-T:(0.5, 0.5, -0.5) path.*

-3%		0%		+3%	
E	$\vec{b}$	E	$\vec{b}$	E	$\vec{b}$
-0.460	(0.291, 0.291, -0.291)	-0.414	(0.305, 0.305, -0.305)	-0.417	(0.335, 0.335, -0.335)
-1.364	(0.195, 0.195, -0.195)	-1.331	(0.203, 0.203, -0.203)	-1.275	(0.200, 0.200, -0.200)
-1.619	(0.228, 0.228, -0.228)	-1.589	(0.255, 0.255, -0.255)	-1.550	(0.250, 0.250, -0.250)
-1.798	(0.058, 0.058, -0.058)	-1.765	(0.069, 0.069, -0.069)	-1.788	(0.071, 0.071, -0.071)

found nodes, the Weyl node shown in Fig. 4.3(a-c) occupying the energy levels –0.461, –0.413, and –0.4177 eV for –3%, 0%, and +3% respectively is the closest to the Fermi level. Despite remaining intact in all the strain cases, the contribution of the mentioned crossing to the BC at the Fermi level was not evident. Although one of the triangles formed by the Mn atoms in the octahedra holds a coplanar inwards magnetic moments configuration and the other has a coplanar outwards magnetic moment configuration, the chirality of both triangles is the same. Thus, as reported in Kübler *et al.*, [167], due to the same chirality of both triangles, the induced Weyl nodes result in the same

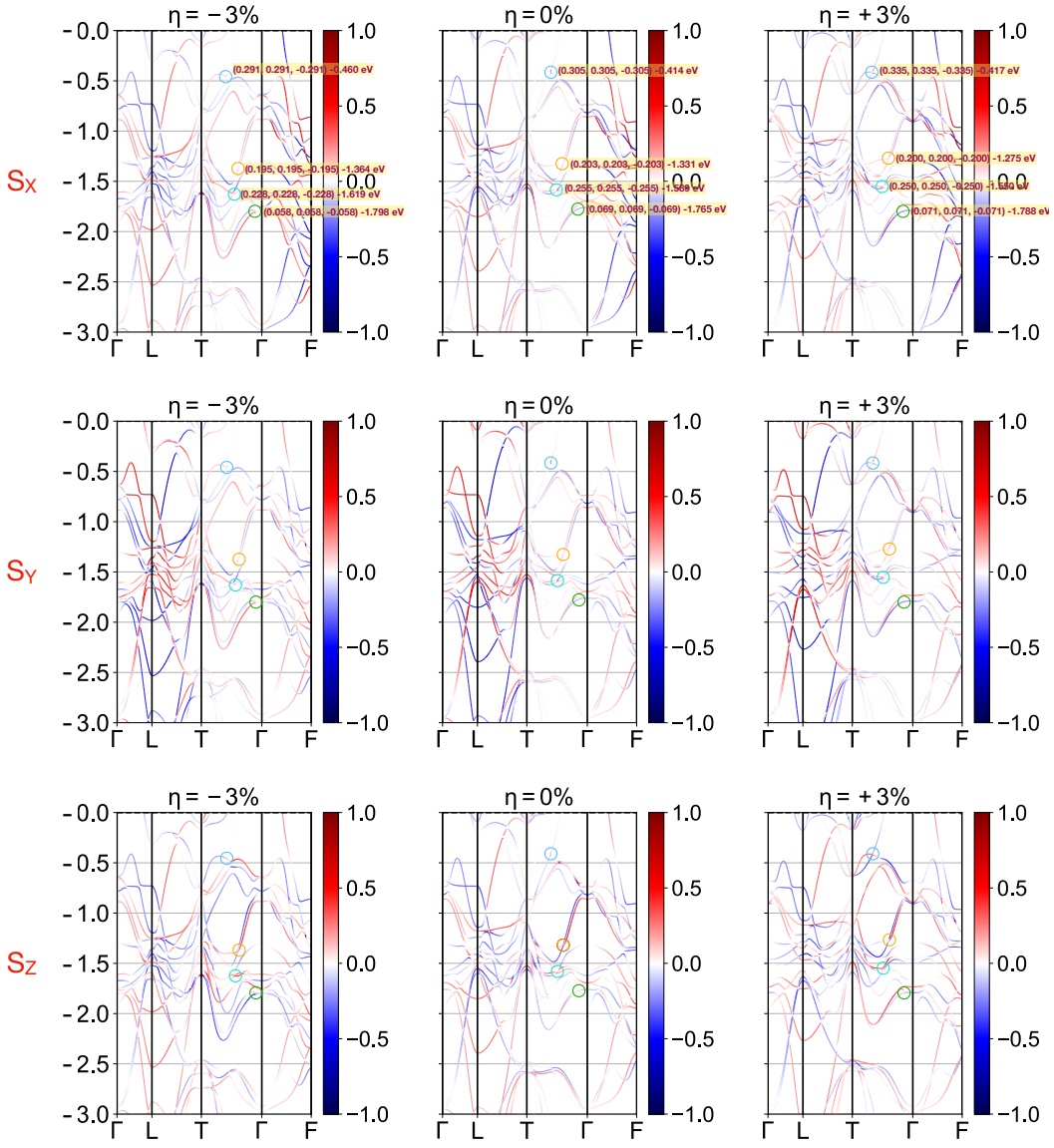

Figure 4.8: *spin projected band structure with four Weyl nodes marked with colored circles for -3%, 0%, and +3% of epitaxial strain.*

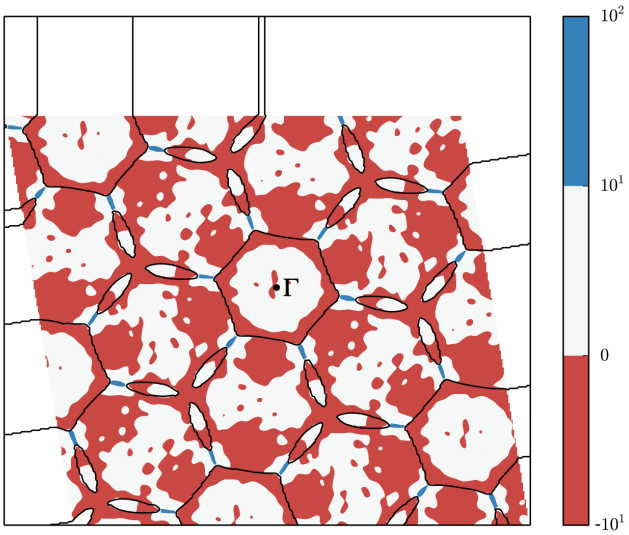

Figure 4.9: *Berry curvature in the 111 plane in units of [Å²] with a magnitude according to the color bar on the right. The* Γ *point is marked in the center of the figure.*

topological charge, canceling each other contribution to the AHC. On the other hand, the BC in the L–T section, shown in Fig. 4.7(c), provides both types of BC, localized and not localized, over the path. The localized BC is once more uncorrelated to the AHC data. This confirms what has already been discussed in the BC analysis along the P2–Γ segment. Interestingly, the spread BC correlates to the AHC for each strain value. The highest values of the BC are $\Omega_{111}^{0\%} = -20.5$ Å^2, $\Omega_{111}^{-1.5\%} = -22.5$ Å^2 and $\Omega_{111}^{-3\%} = -18.4$ Å^2, while for +3% a relatively small value of BC is spotted $\Omega_{111}^{+3\%} = -8.6$ Å^2. The AHC values in each of the mentioned cases are $\sigma_{111}^{0\%} = 114$ S·cm^{-1}, $\sigma_{111}^{-1.5\%} = 140$ S·cm^{-1}, $\sigma_{111}^{-3\%} = 111$ S·cm^{-1} and $\sigma_{111}^{+3\%} = -27$ S·cm^{-1}. It is important to remark that the L–T path lies in a plane parallel to the (111)-plane, and the P2–Γ is parallel to the magnetic symmetry axis (*i.e.* along the (111)-axis and perpendicular to the kagome lattice, see Fig. 4.7(a)). Thus, as expected, the AHE occurs only over the (111)-plane (*i.e.* into the kagome lattice) and not in the perpendicular direction. Therefore, the AHC, induced by a nonvanishing BC in the (111)-plane, conducts the carriers over the same plane where the $\mathcal{T} * \mathcal{M}$ preserving magnetic orderings are placed. This non-divergent BC can be attributed to interband coherence induced by the electronic field

[146]. Avoided band crossings at the Fermi energy level benefit the AHC due to the strong interaction of the occupied and the unoccupied bands [148, 83, 168]. The latter was observed for the computed BC within the (111)-plane included in Fig. 4.9.

4.7 Conclusions

First principle calculations of the AHC in the Mn_3NiN antiperovskite under strain confirmed such deformation as a control mechanism. One of the main results of this study is the strain application methodology in the (111)-plane that preserves the symmetries of the system, allowing control over the dispersion of the bands in energy without changing topology. Notably, the source of the AHC, the $\mathcal{T} * \mathcal{M}$ in the Γ_{4g} magnetic ordering, is kept during the whole straining process, leaving the AHC tensor form unchanged in each case. Thus, the AHC is a function of the distances between the Mn atoms within the same and different kagome lattice planes.

The AHC vs. strain results indicate a non-direct relationship between the AHC magnitude and the epitaxial strain; compression (tension) strain values lead to an enhancing (decreasing) of the AHC only within the range $-2\% \leq \eta \leq +1\%$ of strain. Moreover, a redistribution of the AHC function maxima and minima near the Fermi energy is observed due to the strain. The magnitude of the AHC and the BC as strain functions showed a correlation only over their components in the kagome lattice plane. Therefore, controlling the BC in this plane is also the key to the AHC control. However, there is a limit to this control mechanism, subject to the nontrivial relation between the AHC and the BC. The maximum AHC value is reached between $-1\% \leq \eta \leq -2\%$; further compression only reduces the AHC.

Remarkably, neither the total nor the $3d$-orbital projected DOS in the vicinity of the Fermi energy presented correlations to the AHC. Instead, the physics behind the tuning of the AHC relies exclusively on the non-divergent Berry curvature within the (111) kagome plane. Noteworthy, the AHC in this compound showed no correlation to the band crossings (trivial or topological), and the AHC could be traced to the avoided

crossings and the interband coherences.

In conclusion, the BC in the L–T path in this plane is sensitive to the strain that controls the Mn-Mn distances. Therefore, the strain in the (111)-plane can be linked to the AHC in the Γ_{4g} magnetic phase of Mn_3NiN through the BC in the L–T, proving to be an effective controlling mechanism.

Chapter 5

Structurally Chiral Crystals and its Effect in the Anomalous Hall Conductivity

5.1 Introduction

Chirality, from the symmetry and crystallographic point of view, is related to the handedness that some crystals exhibit. In this sense, chiral crystals can be regarded as right- and left-chiral; a pair of right- and left-handed versions of a crystal with the same chemical formula, are known as enantiomers. Due to that laterality property, all the roto-inversion symmetries are absent in chiral crystals, in which the mirror image of one enantiomer gives the other. The set of symmetries particular to the chiral crystals give rise to a variety of interesting topological phenomena such as the Kramers-Weyl fermions [56], quantized circular photogalvanic current [169] and, the chiral magnetic effect [170]. Moreover, the symmetries removed by the chirality set the conditions for the AHC existence along with the Weyl nodes. Thus, the search for IS- and TRS-breaking chiral crystals is very appealing due to the physics they hold, suitable for many modern applications.

In this chapter, we will cover the conditions for chirality in crystals from the space groups, SG, point of view, and its effect on the electronic band structure. Additionally, we will explore the inference of the chirality on the AHC in the cases of magnetic and non-magnetic phases of ternary compounds. The very interesting lanthanides $LaBPt_2$ and $NdBPt_2$ will be analyzed; the first, a chiral crystal with broken inversion symmetry, and the second, a chiral crystal that breaks both the inversion and the time-reversal symmetry.

5.2 Crystals with Chiral Symmmetry

The next step in this journey concerns the chiral crystals, *i.e.* structures with no glide planes but with screw axis symmetry operations. The SG is the group of symmetry operations of a fundamental pattern able to systematically filling the space. There are 230 SGs compatible with the actual crystals in 3-dimensional space. Such SGs can be classified into chiral and achiral. The latter set contains 208 SGs; 165 out of the 208 SGs are compatible only with achiral crystals, and the remaining 43 are non-chiral SGs compatible with the symmetries of chiral crystals. On the other hand, the group of the chiral SGs is conformed of 22 SGs; 11 pairs of *'right'* and *'left'* handed SGs. The union of the 22 chiral and the 43 chiral compatible SGs form a group known as the Sohncke group [171, 172]. In this final part, the attention concentrates on the chiral crystals with chiral SGs among the 22 chiral SGs (see Table 5.1). Therefore, the search for the crystals started from a list of 500 structures with chiral SG provided by Prof. Aldo H. Romero and his group at West Virginia University. The latter materials were obtained by data-mining over the ICSD [173] and the Materials Project [174] databases. From there, a subset of compounds with no more than 12 atoms in the unit cell was selected, reducing the list from 500 to 64 potential candidates. That list was further filtered, searching for compounds including transition metals, obtaining the following 12 chiral SG crystals to begin the study: ZnTe (SGs 144, 181), HgS (SGs 152,154), $CrSi_2$ (SGs 180,181), VSi_2 (SGs 180,181), $LaBPt_2$ (SGs 180, 181) and, $NdBPt_2$ (SGs 180, 181).

Table 5.1: *Space groups with chiral symmetry operations*

Chiral SGs	
Right-handed	Left-handed
76: $P4_1$	78: $P4_3$
91: $P4_122$	94: $P4_322$
92: $P4_12_12$	96: $P4_32_12$
144: $P3_1$	145: $P3_2$
152: $P3_121$	154: $P3_221$
151: $P3_112$	153: $P3_212$
169: $P6_1$	170: $P6_5$
171: $P6_2$	172: $P6_4$
178: $P6_122$	179: $P6_522$
180: $P6_222$	181: $P6_422$
213: $P4_132$	212: $P4_332$

In Table 5.1 can be evidenced the roto-translation symmetry present in each chiral SGs in the form of a screw axis (*e.g.* 6_2, 4_1, etc.); a symmetry that is expected to induce interesting physics in the same directions. Weyl nodes are an example of properties induced and protected by such symmetries. Here, we proceeded with full structural and electronic optimizations (Details are provided in Section 5.3) revealing the non-magnetic nature (*i.e.* no magnetic moment per atom) of 10 out of the 12 compounds: ZnTe (SGs 144, 181), HgS (SGs 152,154), $CrSi_2$ (SGs 180,181), VSi_2 (SGs 180,181) and $LaBPt_2$ (SG 180, 181). Conversely, $NdBPt_2$ (SG 180, 181) converged in a magnetically active compound with various possible magnetic orderings, including the case with the magnetic moments ferromagnetically aligned in the z-direction. The latter were obtained by a symmetry analysis in the k-Subgroupsmag Tool [175] of the Bilbao Crystallographic Server which allows finding all the magnetic groups compatible with

certain magnetic propagation vectors and the unit cell. As the main interest of this work is to observe the effect of adding magnetism response on top of the chirality of the crystal, the ferromagnetic alignment is enough for the moment. Interestingly, $LaBPt_2$ and $NdBPt_2$ are fairly similar, crystallizing in the same chiral SGs, with the difference of the zero net magnetic moments in $LaBPt_2$ and sizeable magnetic moments per Nd atom in $NdBPt_2$ (m = 2.98 μ_B/Nd). Thus, the two enantiomeric forms of the ternary compounds, $LaBPt_2$ and $NdBPt_2$, are the ideal scenario to study the effect of the magnetism and the chirality on the topological features, specifically, the anomalous Hall conductivity.

In what follows, the structural and electronic properties of the selected chiral crystals will be discussed in detail. To pay special attention to the ternary compounds and the subtleties that differentiate $LaBPt_2$ from $NdBPt_2$, the former will not be included in the discussion concerning the non-magnetic chiral crystals; instead, the structural and electronic properties of both ternary compounds will be addressed in Section 5.5.

5.3 Theoretical and Computational Details

We performed first-principles calculations within the density-functional theory (DFT) [121, 89] approach by using the VASP code (version 5.4.4) [45, 46]. The projected-augmented waves scheme, PAW [122], was employed to represent the valence and core electrons. The electronic configurations considered in the pseudo-potentials, as valence electrons, are Zn: ($3p^2 3d^{10}$, version 09Oct2010), Te: ($5s^2 3p^4$, version 08Apr2002), Cr: ($3p^6 3d^5 4s^1$, version 02Aug2007), V: ($3p^6 3d^4 4s^1$, version 07Sep2000), Si: ($3s^2 3p^2$, version 05Jan2001), La: ($5s^2 5p^6 6s^2 4f^0 5d^1$, version 06Sep2000), Nd: ($6s^2 4f^4$, version 23Dec2003), B: ($2s^2 2p^1$, version 06Sep2000), Pt: ($5p^6 5d^9 6s^1$, version 12Dec2005) and N: ($2s^2 2p^3$, version 08Apr2002). The exchange-correlation was represented within the generalized gradient approximation GGA-PBEsol parametrization [94]. The Nd:$4f$ orbitals were corrected through the DFT+U approximation within the Liechtenstein formalism [123]. Due to the marked misrepresentation in the e–e interaction present in

Nd, which affects the DOS at the Fermi level as in the case of NdAlSi[176, 177], we used the $U = 6.0$ eV parameter in the Nd:4f orbitals. This U value allows the structural optimization to reproduce the experimentally observed lattice parameter in $NdBPt_2$, which is crucial in obtaining an appropriate charge distribution and, ultimately, the electronic properties. The periodic solution of the nonmagnetic crystals were represented by using Bloch states with a Monkhorst-Pack [127] k-point mesh of 7×7×5 and 600 eV energy cut-off to give forces convergence of less than 0.001 eV·Å^{-1} and an error in the energy less than 10^{-6} eV. In the case of $LaBPt_2$ and $NdBPt_2$, we used a mesh of 11×11×9 and the same cut-off energy to achieve a similar accuracy in the groud state and the forces. The spin-orbit coupling (SOC) was included in all the cases to consider non-collinear magnetic configurations [128] and observe the spin-inversion in the band structures. The anomalous Hall conductivity, and associated observables, were obtained with the Python library WannierBerri [102] using the maximally localized Wannier functions and the tight-binding Hamiltonian generated with the Wannier90 package [101]. The interpolation was performed with the following number of Wannier functions and projections: $LaBPt_2$:162WF[1] La:(p;d), B:(p), Pt:(p;d), $NdBPt_2$:174WF Nd:(p;f), B:(p), Pt:(p;d). For the disentanglement process, we used an energy window +3.0 eV higher than Fermi level as the maximum, and none for the minimum, and a convergence tolerance of 5.0×10^{-8} Å^2. The atomic structure figures were elaborated with the vesta code [129]. Finally, the band structure was analyzed with the Python library PyProcar [130].

5.4 Non-magnetic Chiral Crystals

Since the beginning of this research work, most of the crystals were expected to be non-magnetic with interesting spin textures as in the case of chiral tellurium crystals [23] reported recently within the 154 and 152 SGs. There, magneto-optical and magneto-electric responses have been observed experimentally, rendering attractive possibilities

[1] Wannier functions

on the side of physical functionalities triggered by the chiral symmetry. Nevertheless, the list conformed by ZnTe (SGs 144, 181), HgS (SGs 152,154), $CrSi_2$ (SGs 180,181), VSi_2 (SGs 180,181), and $LaBPt_2$ (SG 180, 181) was confirmed as non-magnetic; a result expected due to the lack of magnetic atoms in their structures.

In the case of ZnTe, it was found to crystallize in two different chiral SGs, shown in Fig 5.1. Naturally, each SG of ZnTe presents an associated electronic band structure with distinctive characteristics associated with the allowed symmetries.

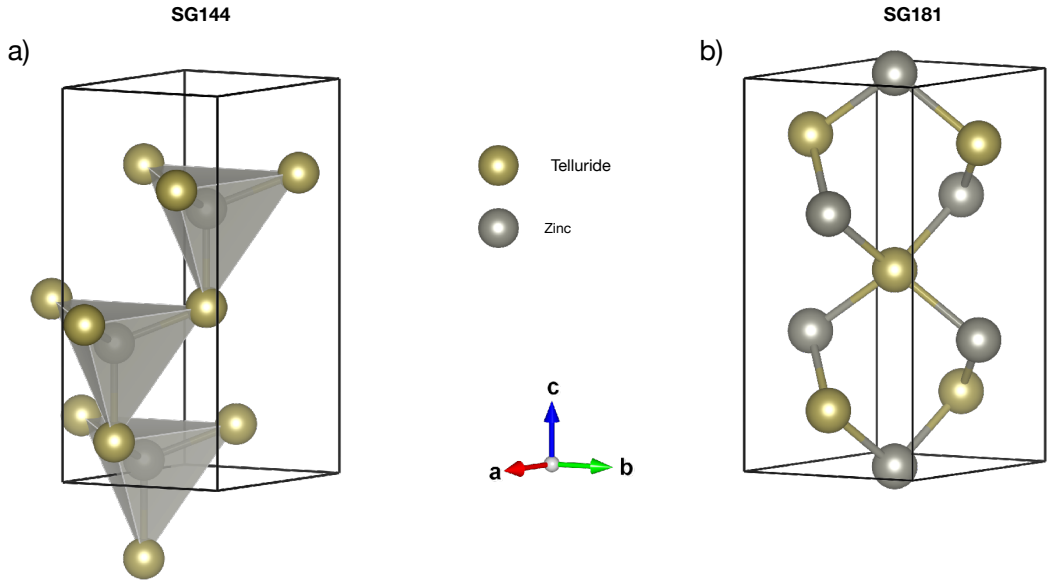

Figure 5.1: *The crystalline structure of ZnTe in two different chiral configurations belonging to the chiral SGs 144, 181.*

In Figure 5.2, it can be observed the electronic band structure for each chiral SG of ZnTe. There, some similarities arise, for example, along the Γ–M and the K–Γ paths, presumably, because of the same atomic species among both compounds. However, because of the different screw axis, differences are observed, mainly in the Γ–A path, which lies in the direction parallel to the 3_1 and 6_4 symmetry axis of the 144 and the 181 SGs.

Interestingly, the Γ–A path holds various bands crossings, with a linear dispersion which is clearly between non-degenerated bands in the case of the 181 SG. In such

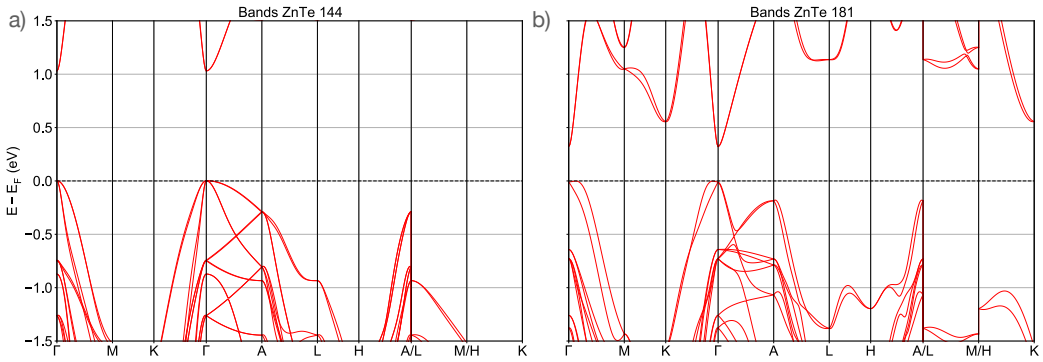

Figure 5.2: *The electronic band structure of ZnTe in two different chiral configurations belonging to the chiral SGs 144, 181. The*

a case, the crossing might be generated by symmetry and, therefore, belong to the Weyl node classification. To observe this phenomenon more clearly, the example of the enantiomers HgS SG. 152 and HgS SG. 154 is going to be analyzed; a very simple chemical formula that, due to the chirality, translates into a 6 atoms unit cell. The mentioned enantiomers can be observed in Figure 5.3.

Here, due to the chirality, a complete identification of a Weyl node would require a spin projection of the band structure. In Figures 5.4(a) to 5.4(f) are presented the spin-projected band structures of the 152 and 154 SGs of HgS. An immediate observation and comparison of the projections for both crystalline structures reveal an inversed spin polarization of each band when compared with its counterpart in the other enantiomer. Furthermore, the path Γ–A, parallel to the screw axis, permits only charge carriers with an S_z component of the spin. Moreover, in the same path, clear evidence of linearly dispersing single-point degeneracies is observed near the Fermi level, between 0.0 eV and –0.25 eV. Such degeneracies are Weyl nodes protected by the roto-translation symmetry present in that path of the Brillouin Zone. The roto-translation symmetry of chiral crystals automatically induces an IS breaking which along with the SOC is the requirement for Weyl semimetallic phases [178].

A similar situation is observed along the M-point, where the inversion of the spin occurs exactly at that high symmetry point. After the discussed results, the Weyl nodes

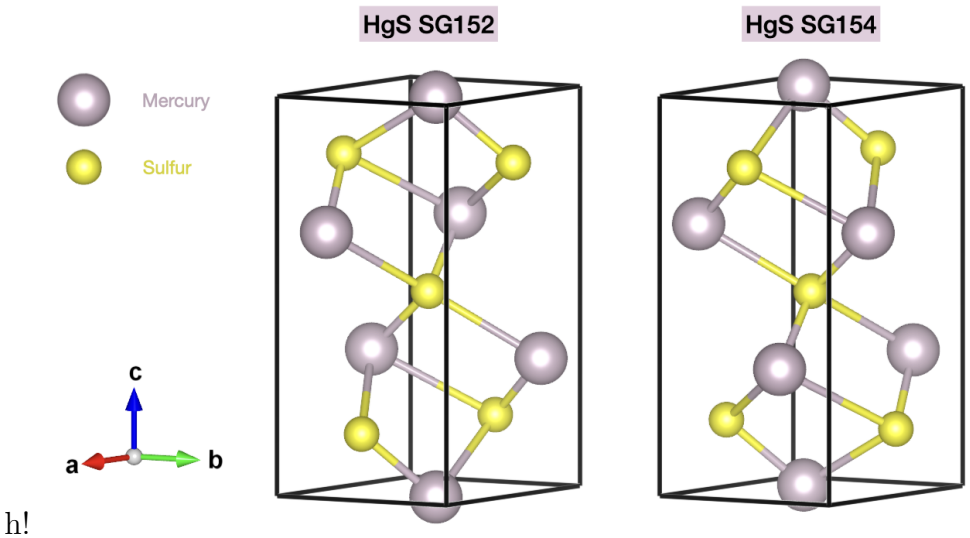

h!

Figure 5.3: *Crystalline structure of the enantiomers HgS SG.152 and HgS SG.154. In both symmetry groups, the chiral symmetry can be appreciated by observing the roto-inversion symmetry operation.*

as degeneracies protected by the symmetry have been confirmed in chiral crystals, populating the zones with screw axis symmetry principally in the Brillouin Zone.

In Figure 5.5, a zoom of the band structure of HgS can be observed. The effect of the chirality over the bands is corroborated along the Γ–A path in this compound; the spin projection reveals an inverted projection in one enantiomer with respect to the other. Finally, an example of a degeneracy removal due to the SOC can be observed in the band structure of $CrSi_2$, presented in Figure 5.6. The band structure calculation, without including the effect of the spin-orbit coupling, shows various band crossings, which might be confused with Weyl nodes and are associated with trivial crossings. However, the non-symmorphic symmetries are not present in the L–H–A path to protect the crossings, in which case, the SOC coupling can break the degeneracy. In this case, it is said that the crossing is not protected by symmetry.

The complete electronic band structures of $CrSi_2$ and VSi_2 are included in the Appendix section 7 in Figs. 7.1, 7.2, along with the structural parameters for all the non-magnetic compounds.

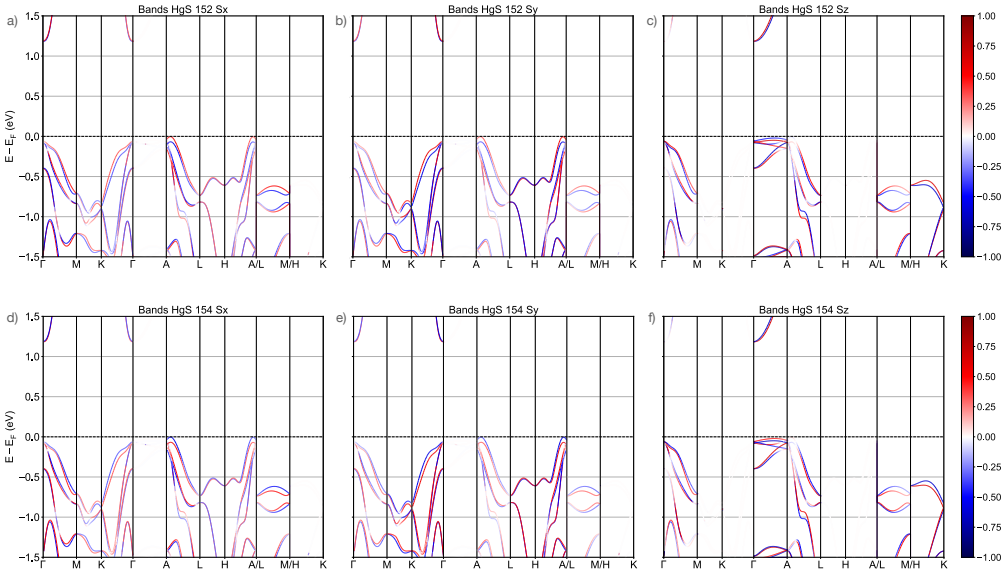

Figure 5.4: *The spin-projected electronic band structure of HgS in the two enantiomeric configurations belonging to the chiral SGs 152 and 154.*

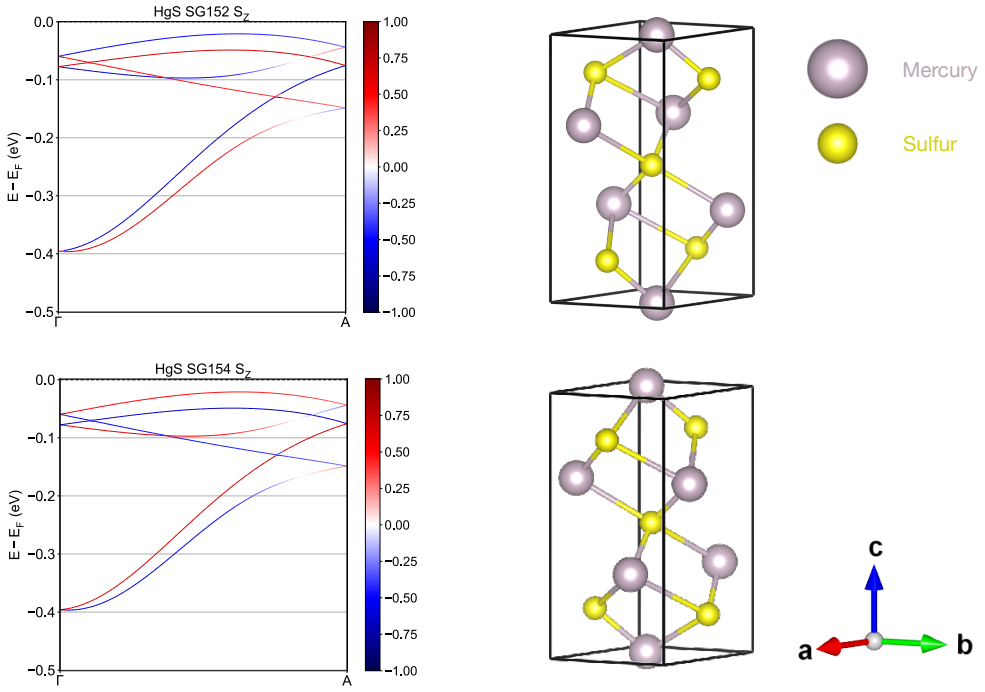

Figure 5.5: *The spin-projected electronic band structure of HgS in the two enantiomeric configurations belonging to the chiral SGs 152 and 154 along the Γ–A path.*

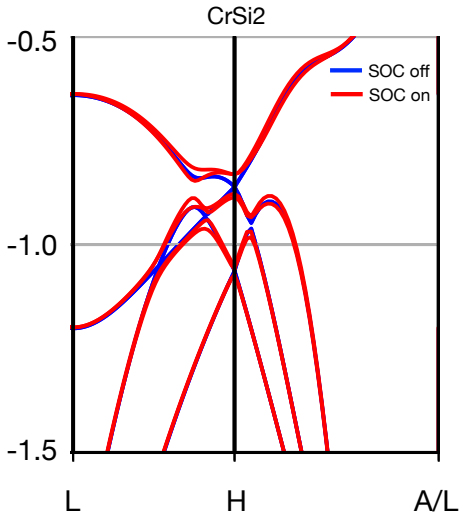

Figure 5.6: *A close-up of the electronic band structure for $CrSi_2$ SG. 181 without spin-orbit in blue in the background and with spin-orbit coupling in red in the front.*

5.5 Magnetic $NdBPt_2$ vs Non-Magnetic $LaBPt_2$

In Figure 5.7 are shown the crystalline structure of $LaBPt_2$ and $NdBPt_2$ SG180 along with the $NdBPt_2$ SG181. At first sight, both right-handed LBPt$_2$ (L=La and Nd) SG.180 ternary compounds have almost identical crystalline structures and helicoidal arrangement of the atomic sites. Alternatively, the left-handed $NdBPt_2$ SG.181, which is the mirror image of the $NdBPt_2$ SG.180, shows an inverted helix when compared to its counterpart.

In agreement with the experimental reports [179, 180], $NdBPt_2$ and $LaBPt_2$, have fairly similar lattice parameters (see Table 5.2). Moreover, both enantiomers of each compound have the same lattice parameter. Although the data presented so far indicate no major differences between $LaBPt_2$ and $NdBPt_2$ other than the substitution of La by Nd, the magnetic nature of Nd has a big impact on the electronic properties of the system.

Of course, being such an interesting crystalline structure, $NdBPt_2$ is compatible with a wide range of magnetic orderings, both coplanar and noncoplanar. In Figure 5.8 can be observed some of the coplanar configurations of the magnetism permitted;

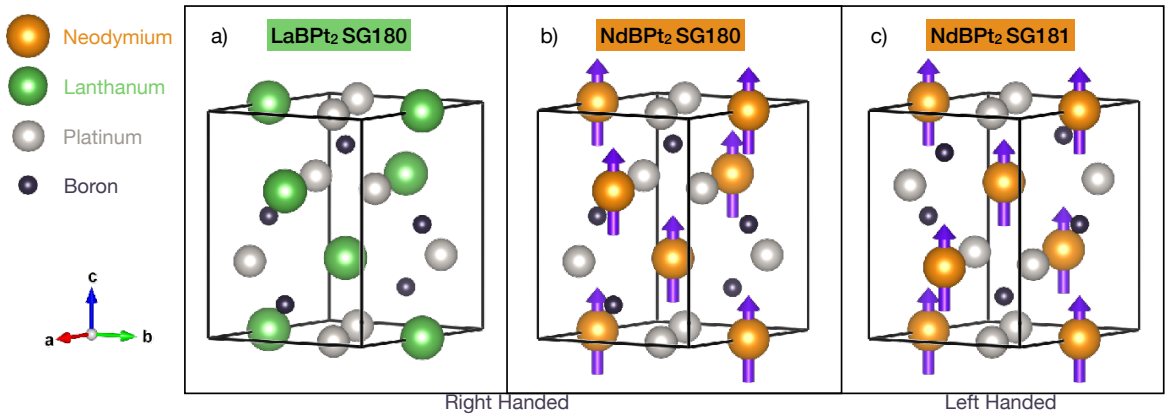

Figure 5.7: *Crystalline structure of a) $LaBPt_2$ SG.180, b) $NdBPt_2$ SG.180 and, c) $NdBPt_2$ SG.181. In the $NdBPt_2$, the violet arrows denote the magnetic moment per Nd atom.*

obtained with the k-Subgroupsmag Tool from the Bilbao Crystallographic server [175], which allows finding all the magnetic subgroups compatible with a given propagation vector. Interestingly, the ordering in parts (a) and (b), when seen from the top part

Table 5.2: *Lattice parameters, in Å, experimentally reported and computationally obtained for the $LaBPt_2$ and $NdBPt_2$ compounds.*

		This work
	Experimental	PBEsol
$LaBPt_2$	$a = b = 5.5222$ Å, $c = 7.8978$ Å [179]	$a = b = 5.516$ Å, $c = 7.844$ Å
$NdBPt_2$	$a = b = 5.4242$ Å, $c = 7.8799$ Å [179, 180]	$a = b = 5.422$ Å, $c = 7.897$ Å [1]

of the structure, resemble the Γ_{5g} and Γ_{4g} of the antiperovskites studied in this work, see Chapter 4. When analyzed in the standard view the structure reveals that these orderings are formed along various planes at different z-positions. Notably, the structure in Figure 5.8(c), similar to a blender blade, removes all the symmetry operations except the screw axis along the z-direction.

Three noncoplanar noncollinear ferromagnetic orderings compatible with the

[1] With the Hubbard correction to the f orbital $U = 6.0$ eV

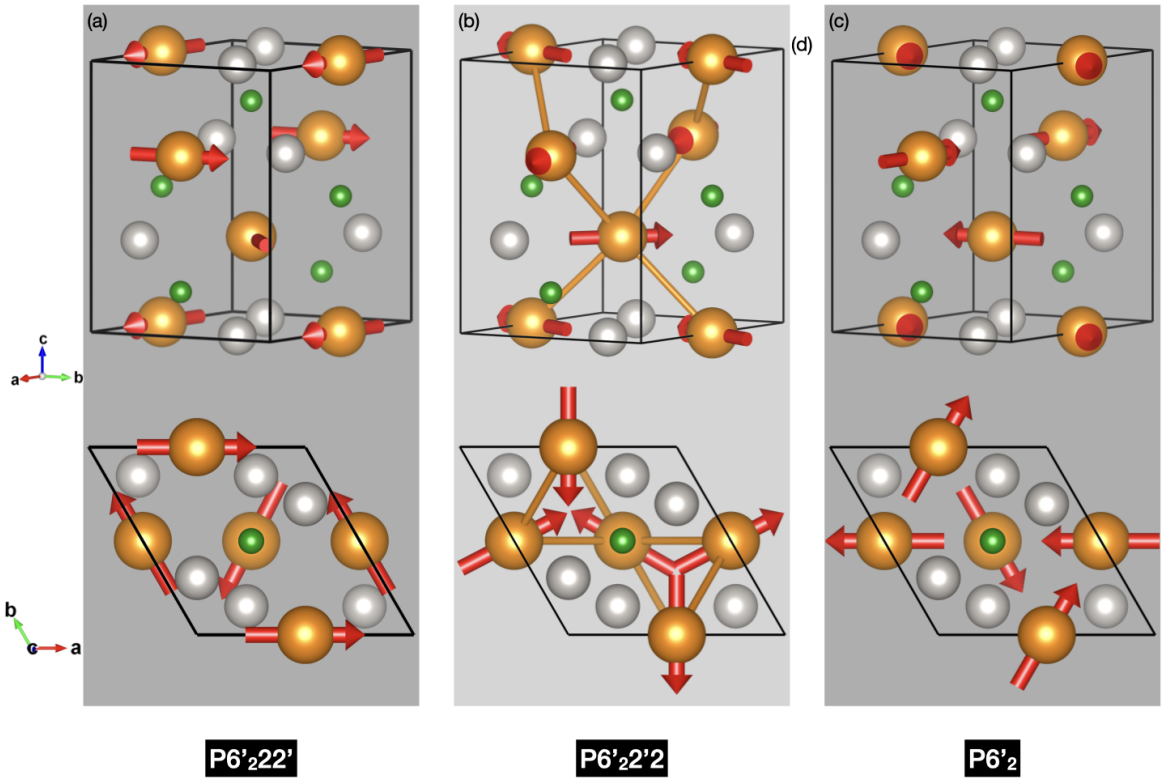

Figure 5.8: *(a-c) Other coplanar magnetic orderings compatible with $NdBPt_2$ SG.180. Here, clear noncollinear chiral antiferromagnetic orderings can be observed.*

$NdBPt_2$ crystalline structure are shown in Figure 5.9. Each can be understood as the combination of the noncollinear antiferromagnetic orderings in the xy-plane coupled to a ferromagnetic component in the z-direction. Notably, this net magnetic component further reduces the symmetry, setting it to $P3_2$ in the case shown in Figure 5.9(c). Interestingly, the screw axis changes from 6_2 to 3_2 in all the ferromagnetic noncoplanar structures.

The ground state for the magnetic point groups shown in Figs 5.8 and 5.9 are consigned in Table 5.3. There, a similar energy for all the magnetic orderings in $NdBPt_2$ can be observed. In this work, however, due to the limitation in time, we will concentrate our efforts on collinear ferromagnetic ordering and crystalline chirality. Nonetheless, due to the possibilities that these magnetic orderings represent in terms of physical properties a more profound revision of them is worth it and will be addressed

Table 5.3: *Ground state energy in eV for $NdBPt_2$ in different ferromagnetic (FM), non-collinear antiferromagnetic NCAF and, noncollinear ferromagnetic NCFM point groups*

Space group (magnetic ordering)	$E_0[eV]$
$P6_22'2'$ (FM)	-108.4447
$P6'_22'$ (NCAF)	-108.4453
$P6'_22'2$ (NCAF)	-108.4548
$P6'_2$ (NCAF)	-108.4434
$P3_22'1$ (NCFM)	-108.4450
$P3_212'$ (NCFM)	-108.4550
$P3_2$ (NCFM)	-108.4341

in future works. Despite this, a graph with the full magnetic subgroups possible is included in the Appendix Section 7.2. The latter was obtained through the Bilbao Crystallographic Server k-Subgroupsmag tool [181, 166], which performs a systematic breaking of symmetries to obtain all the magnetic symmetry groups compatible with a give propagation vector.

In what follows, the differences between both compounds will be highlighted to distinguish the inference of the magnetic contribution introduced in the $L\mathrm{BPt}_2$ properties by the Nd sites. First, let us discuss the main features of LaBPt_2. In Figure 5.10, the band structure for LaBPt_2 and NdBPt_2 are shown. As shown there, this ternary compound is metallic with bands crossing the Fermi level in all directions for the paths L–H–K–M, which belong in the same squared face of the hexagonal Brillouin zone.

In Figure 5.11, the band structure for LaBPt_2 SG180 including the SOC interaction is superimposed on top of the band structure for the same compound excluding the SOC. Remarkably, the removal of the SOC leaves the band structure completely degenerated in all the paths. This result was surprising, because of the lack of inversion symmetry present chiral crystals, we were expecting the bands to be non-degenerate

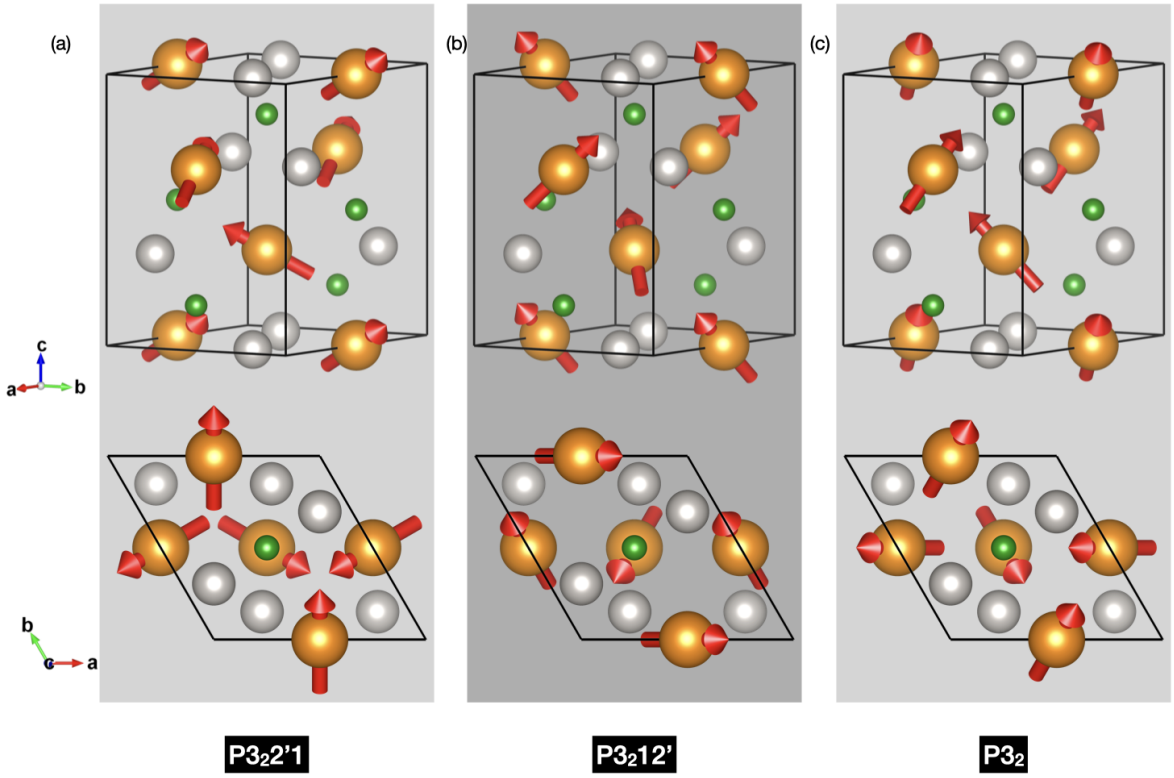

Figure 5.9: *(a-c) Other noncoplanar magnetic orderings compatible with $NdBPt_2$ SG.180. Here, it can be observed the noncollinear chiral antiferromagnetic ordering, in the xy-plane, coupled to a ferromagnetic component along the z-axis.*

even in the absence of SOC. For example, the $LaBPt_2$ and $NdBPt_2$ crystals have the point group 622 which lacks of center of inversion. However, the degeneracy lifting in the presence of the SOC interaction suggests that the presence of Weyl nodes and related properties, such as the AHC, also relies on this interaction [178]. Therefore, the combination of IS/TRS breaking, non-symmorphic symmetries, and, SOC is required for the existence of the Weyl nodes in these compounds.

As expected from the enantiomers of a chiral compound, the electronic band structures of $LaBPt_2$ SG.180 and $LaBPt_2$ SG.181 are indistinguishable, and their differences can be established only by the spin projection of the bands.

A direct comparison of the spin-projected electronic band structures of $LaBPt_2$ SG.180 and $LaBPt_2$ SG.181, in Figure 5.12, shows that spin-up bands in the SG.180

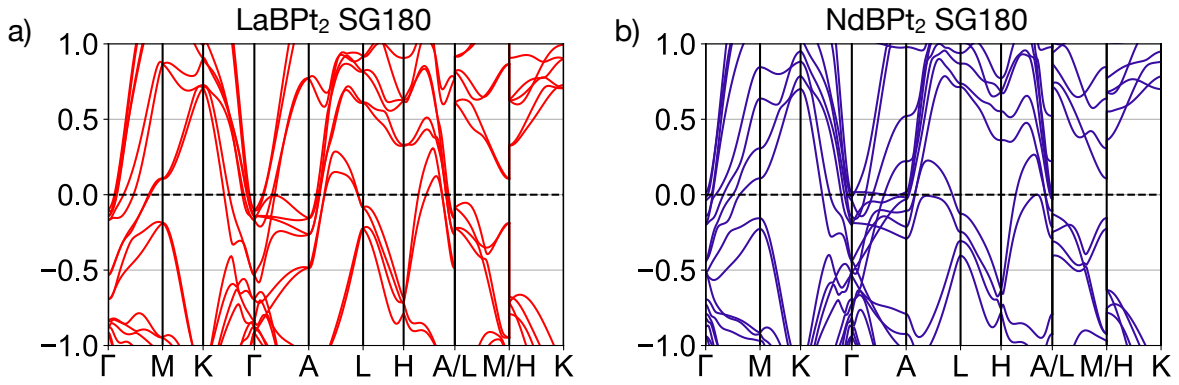

Figure 5.10: *Electronic band structure of (a) $LaBPt_2$ SG180, (b) $NdBPt_2$ SG180.*

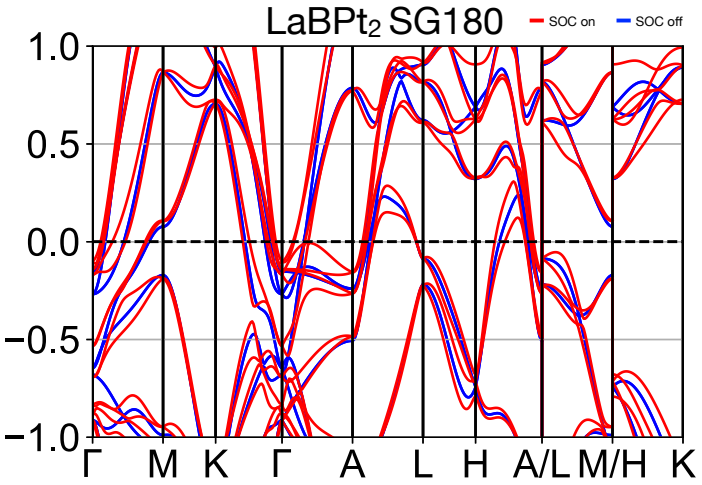

Figure 5.11: *Electronic band structure of $LaBPt_2$ SG180 with spin-orbit coupling included in red on top of the band structure for the same compound without the spin-orbit coupling interaction.*

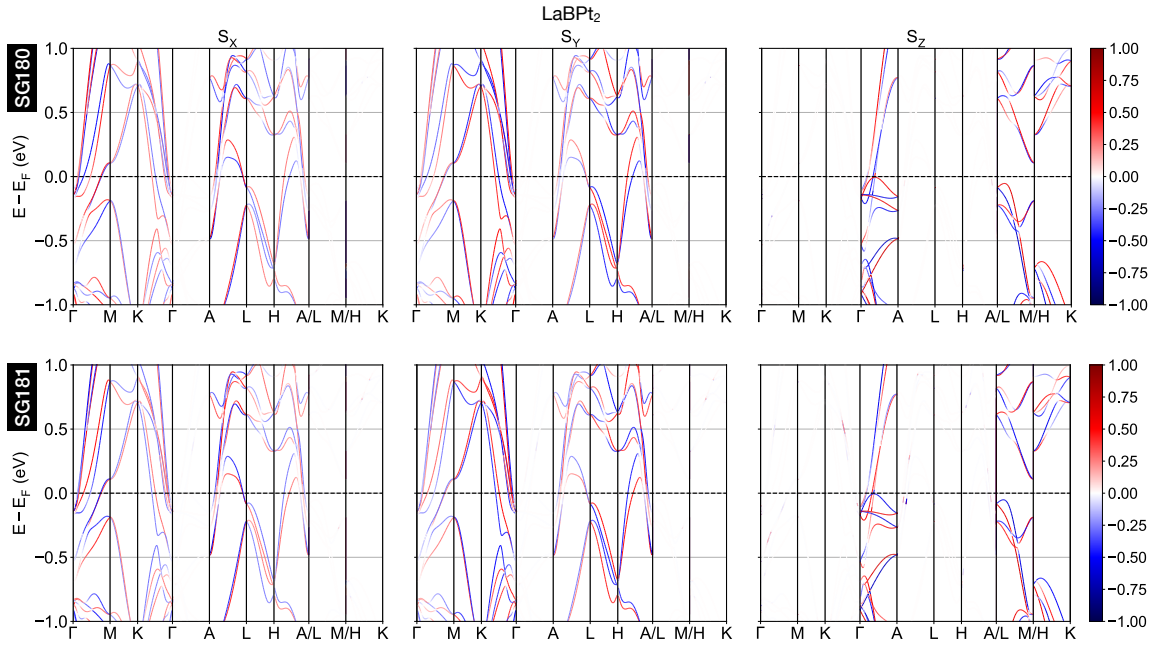

Figure 5.12: *Electronic band structure of $LaBPt_2$ SG.180 projected per spin component.*

are spin-down bands in the SG.181. Interestingly, once more, the Γ–A direction which coincides with the 6_2 and the 6_4 screw axis of the 180 and the 181 SGs, displays only the s_z projection of the spin. Thus, the z-component of the spin is only allowed to propagate along the axis of chiral symmetry the parallel directions, while absent in the perpendicular plane to that direction. Again, as in the case of HgS, the Weyl nodes were found mainly within the Γ–A path, where the screw axis symmetry is present. $NdBPt_2$, on the other hand, is a metallic compound where the TRS breaking induced by the magnetism separates the bands even more. The substitution of the Lanthanum site by the Neodymium in $LaBPt_2$ displays the interesting feature of ferromagnetically aligned magnetic moments in the z-direction. Such a magnetism response has its origin in the Nd sites, which have 4 unpaired electrons in the $4f$ orbital, achieving a $\mathbf{m} = 2.967$ μ_B magnetic moment per Nd atom. Furthermore, within the framework of the density functional theory, the four unpaired electrons in an f orbital, able to hold a total of 14 electrons, will suffer from a misrepresentation of the e–e exchange-correlation [177] as in the case of the low-populated d orbital in the Mn_3BN antiperovskites discussed

in Chapter 3.

Moreover, the structural optimization of $NdBPt_2$ was impossible without the Hubbard U correction; a $U = 6.0$ eV was needed since the beginning of the calculations to achieve convergence and stabilize the structure. This value for the U parameter has been established in a recent report as the appropriate correction for the electronic correlations in the $4f$ orbitals of Nd [176]. A large contribution of the f orbitals to the DOS at the Fermi level occurs in the absence of such correction.

Heavy atoms such as lanthanides are difficult to model with the density functional theory due to their large number of electrons, many of which are enclosed inside the pseudo-core, encapsulating their effect on the properties of the atom [182]. Thus, a small number of valence electrons are taken into account, and correlation issues are introduced by low-populated f orbitals worsening the situation [183]. The U parameter, as has already been observed in the noncollinear antiperovskites studied in Chapter 3, is directly related to the magnetic moments of the magnetic sites. This correction is needed by DFT to automatically reproduce the experimental volume and stabilize the structure while avoiding negative phonons that appear in the non-corrected calculations. Therefore, the $U = 6.0$ eV correction is mandatory because it stabilizes the structure and improves the calculations of the magnetism in the highly correlated compounds with low-populated d or f orbitals. The magnetism is a very important feature when it comes to the AHC, as the net magnetization is known to dramatically increase the AHC in ferromagnets such as in the case of the body-centered cubic Fe [148, 102]. Moreover, the AHC requires TRS breaking to exist; in the case of IS breaking only, the Berry curvature at **k** and **-k** have the same magnitude and opposite sign, which causes vanishing of the BC and the AHC [184, 185]. However, for the purpose of comparison and confirmation, the AHC in $LaBPt_2$ is shown here. Thus, a contrast between the AHC calculated in the non-magnetic $LaBPt_2$ and the ferromagnetic phase of $NdBPt_2$ chiral structures will be made. As such, it allows us to observe the AHC behavior under the effect of the crystalline chirality in the IS broken $LaBPt_2$ and compare it to $NdBPt_2$ where both IS and TRS are broken because of the ferromagnetic ordering in

the z-direction on top of the chiral structure.

In Figure 5.13 is presented the band structure of $LaBPt_2$ interpolated with Wannier functions superimposed over the band structure calculated within VASP [45, 46]. The mentioned band structures match fairly well, showing a good correspondence within the area around the Fermi level, a good indicator of a proper set of Wannier functions, and a good disentanglement process.

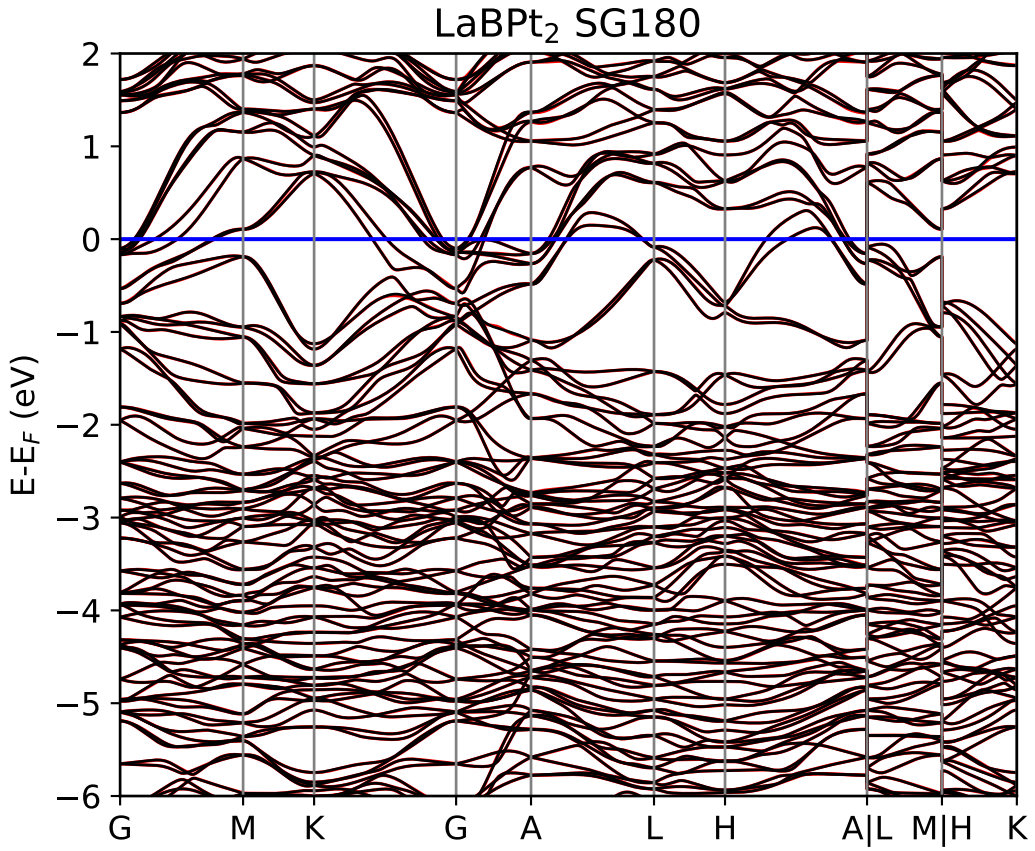

Figure 5.13: *Electronic band structure of $NdBPt_2$ SG.180, denoted in black color, interpolated in a set of Wannier functions, denoted in red color, on top of the ab-initio band structure.*

As a result, a well-fitted tight-binding Hamiltonian was obtained, which will serve as the tool to calculate the AHC. The AHC results will be discussed in the final part, along with the results for $NdBPt_2$. Unfortunately, calculating the appropriate set of Wannier

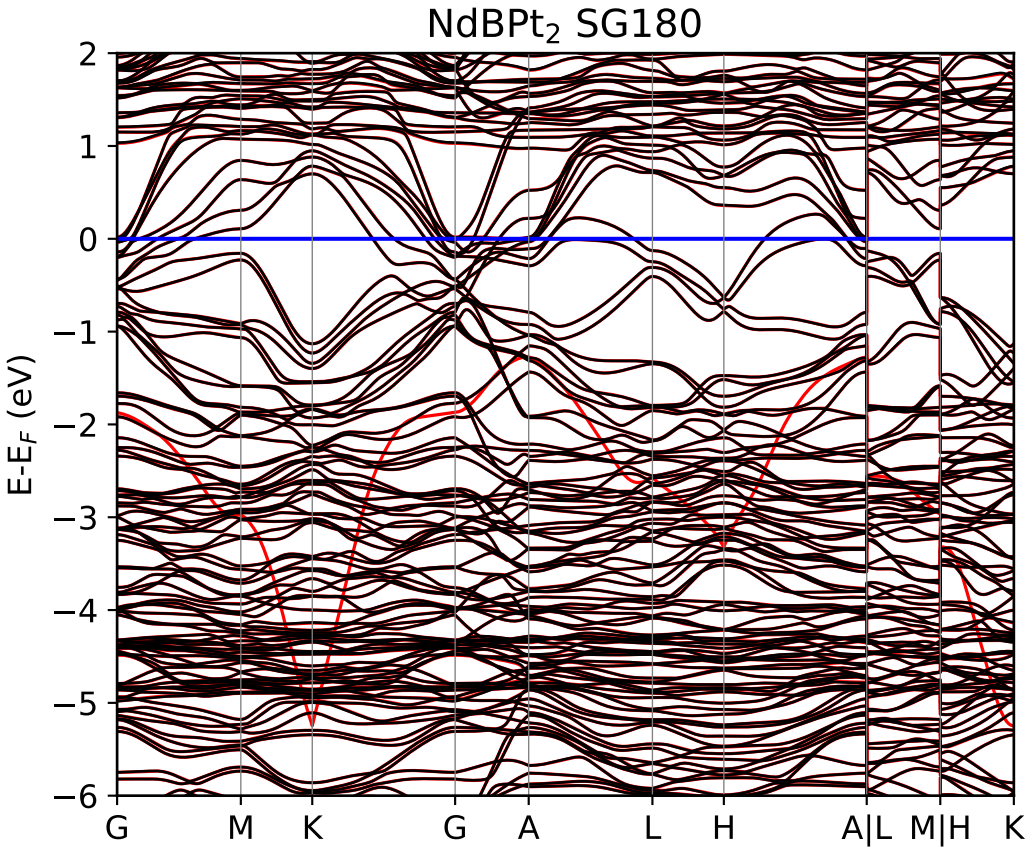

Figure 5.14: *Electronic band structure of $NdBPt_2$ SG180 interpolated in a set of Wannier functions on top of the ab initio bandstructure.*

functions for the ternary compounds considered in this thesis was a very difficult task and time demanding that limited the reach of the results. For example, in Figure 5.14, the band structure calculated in VASP is presented in black, superimposed over the electronic band structure interpolated through the Wannier functions, presented in red, obtained after the wannierisation performed in the WANNIER90 code [101]. Here, the match between both band structures is almost perfect, except for a single band that only appears in the Wannier interpolation for the energies below -1.2 eV. This situation is problematic because the Tight-Binding Hamiltonian cannot be fully trusted unless the interpolated band structure replicates the DFT band structure. Nevertheless, due to the almost exact Wannier and DFT band structure, the results could still be useful.

Therefore, they will be reported here as preliminary data on the AHC behavior in the chiral crystals with a chiral space group. The symmetry imposed conductivity tensor in the case of $NdBPt_2$ (MSG 180.171) with magnetic point group 62'2' and magnetic Laue group 6/mm'm' is given as [162]:

$$\sigma = \begin{pmatrix} \sigma_{xx} & \sigma_{xy} & 0 \\ -\sigma_{xy} & \sigma_{yy} & 0 \\ 0 & 0 & \sigma_{zz} \end{pmatrix} \tag{5.1}$$

where the diagonal is populated by the ordinary components of the conductivity, while in the off-diagonal terms, we can see the AHC components.

Table 5.4: *Anomalous hall conductivity components for $LaBPt_2$ and $NdBPt_2$ SG180 in the PBEsol+U, U = 6.0 eV approximation.*

	This work
	AHC [S/cm]
$LaBPt_2$	σ_{xy} = –5.445, σ_{yz} = –0.273, σ_{zx} = –8.000
$NdBPt_2$	σ_{xy} = –234.636, σ_{yz} = –0.762, σ_{zx} = 1.845

In Table 5.4, are listed the AHC components for $LaBPt_2$ and $NdBPt_2$, respectively. There, a small magnitude of each component can be observed in the case of $LaBPt_2$, showing almost no particular plane for the AHC in this compound. A similar situation occurs in the planes parallel to the magnetic axis in $NdBPt_2$; the components are negligibly small. Nonetheless, in the plane perpendicular to the magnetic axis, the AHC has a magnitude significantly higher. The results of both compounds suggest a minor inference of the crystalline chirality on the AHC, highlighting the magnetization as the source of this anomalous transport property in chiral crystals. Nevertheless, the chirality, being the reason behind the inversion symmetry removal, is a crucial ingredient for the existence of the AHC in these compounds. Moreover, it is, to the best

of our knowledge, the first demonstration of AHC in a chiral material with magnetic response.

5.6 Conclusions

In this chapter, the structural and electronic properties of ZnTe (SGs 144, 181), HgS (SGs 152,154), $CrSi_2$ (SGs 180,181), VSi_2 (SGs 180,181), and $LaBPt_2$ (SG 180, 181) were covered along with the AHC, a property derived from the electronic structure. Interesting properties, such as the spin inversion at Weyl points and inverted spin projections of the band structures in an enantiomer with respect to the other, were observed in chiral crystals with chiral SG. Both, $NdBPt_2$ and $LaBPt_2$, chiral ternary compounds showed interesting spin transport phenomena. Particularly, the directions parallel to the roto-translation axis, transport only the z-component of the spin. However, anomalous transport phenomena were not observed along the chiral axis or in the perpendicular plane; $LaBPt_2$ showed no relevant AHC components in any of the planes. Naturally, the off-axis components of the conductivity tensor are null in TRS-preserving compounds with broken IS. In such compounds, the Berry curvatures vanish due to the $\Omega(\mathbf{k}) = -\Omega(-\mathbf{k})$ that the TRS imposes. In the case of $NdBPt_2$, the result along the chiral axis was similar to $LaBPt_2$, with the difference in the AHC in the plane perpendicular to the magnetic symmetry axis. The AHC in the plane perpendicular to the screw axis of the crystal was considerably enhanced, reaching more than $\sigma_{xy} = 200$ S/cm. This result was expected and aligned with the reports on AHC in ferromagnets [168, 186, 148]. Thus, the results suggest little or no inference of chirality in the AHC beyond the removal of IS. Additionally, the role of magnetic ordering and TRS breaking is reaffirmed; besides having the same SG, $NdBPt_2$ have AHC while the same property is absent in $LaBPt_2$. Furthermore, the breaking of IS and TRS allows the existence of Weyl nodes in both compounds, but once more, the presence of such solid-state quasiparticles is not enough to trigger the AHC. Again, as in the case of the Γ_{4g} phase of Mn_3NiN, the Weyl nodes near the Fermi level seemed unrelated to the

AHC magnitude. Nevertheless, a more in-depth study of the AHC in chiral crystals is still needed to discard the impact of chirality on the AHC.

Chapter 6

Main Conclusions, Remarks, and Future Outlook

Through first-principles calculations and theoretical analysis, the role of chirality, from the magnetic and symmetry point of view, on the AHC in multifunctional materials has been investigated. As a general remark, so far, it is safe to say that the main contribution made by crystalline chirality is to aggregate a new functionality related to the removal of inversion symmetry. Also, crystalline chirality protects the Weyl nodes along the axis of chiral symmetry, allowing other phenomena, such as the chiral anomaly. On the other hand, the vector chirality, typical of the noncollinear antiferromagnets, is the main ingredient for the AHC existence in the compounds.

The magnetic frustration in Mn_3BN antiperovskites results from many different interactions, including the exchange, superexchange, DM, and RKKY. On top of this, the p-d hybridization between the Mn and N sites adds a highly correlated response, unleashing noncollinear antiferromagnetic orderings. As a result, the chiral degree of freedom is permitted and enhanced by the spin-orbit coupling arising from the transition metals Mn and B. The relation between the magnetic moments and the volume variations induced by substitutions of the transition metal in the B-site allowed us to study the spin-lattice coupling, concluding a correlated material. The latter is

confirmed by the impossibility of appropriate modeling in the LDA approximation. Additionally, magnetic moment increment through a spin-lattice coupling with the B sites substitutions stabilizes and enhances the magnetic frustration. On the other hand, a pure PBEsol approximation was not enough to reproduce the data of the experimental reports, and due to the strong volume dependence in these compounds, an imposed fixed cell volume was required to align the computational model with the experimental reports. The most accurate description of these systems was given the PBEsol+U, with U = 2.0 eV, which fairly reproduces a cell volume and AHC results better fitting the experimental data and the hypothesis proposed for the compounds studied here. The calculations in the PBEsol+U scheme showed a strengthened AHC with the successive substitutions B = Ni, Pd, and Pt, increasing the correlation and spin-orbit coupling in the system.

Among the studied structures, Mn_3NiN was chosen for a more profound revision, comprehending strain-driven control of the AHC. Here, it is worth recalling the success of the strain methodology proposed in this work. The strain application methodology in the (111)-plane preserves the symmetries of the system, allowing control over the dispersion of the bands in energy without changing topology. Thus, the $\mathcal{T} * \mathcal{M}$ in the Γ_{4g} magnetic ordering along with the AHC tensor are kept during the whole straining process. Facilitating the study of the AHC as a pure function of the distances between the Mn atoms of the structure. The relation between the AHC and the strain resulted in a nontrivial and nonmonotonic response within the range –3%$\leq \eta \leq$+3%. However, compression (tension) strain values enhance (decreasing) the AHC within the subset of values ranging –2%$\leq \eta \leq$+1% of strain. Moreover, a redistribution of the AHC function maxima and minima near the Fermi energy was observed due to the strain, confirming the controllability of the AHC. Interestingly, the AHC and the BC correlated as strain functions only over their components in the Kagome lattice plane. Therefore, controlling the BC in this plane is also the key to the AHC control, a control mechanism subject to the nontrivial relation between the AHC and the BC, reaching its maximum efficiency within –1%$\leq \eta \leq$ –2%; further compression only reduces the

AHC. Remarkably, despite being a transport phenomenon, the AHC was unrelated to DOS in the vicinity of the Fermi energy. Instead, the AHC turned out to be connected exclusively to the non-divergent Berry curvature within the (111) Kagome plane, and more precisely, in the L–T path. Noteworthy, the AHC in this compound showed no correlation to the band crossings (trivial or topological); its magnitude was found relying on the avoided crossings and the interband coherences. Thus, the strain controls the distances between the Mn atoms, altering the BC in the L–T path, ultimately affecting the AHC, which is intimately linked to the BC over the plane of chiral symmetry. Therefore, the strain in the (111)-plane can be linked to the AHC in the Γ_{4g} magnetic phase of Mn_3NiN through the BC in the L–T, proving to be an effective controlling mechanism.

Crystals with chiral SG showed their interesting properties, among which the spin inversion at Weyl points and inverted spin projections of the band structures were observed. Particularly the bands in directions parallel to the roto-translation axis showed transport only of the z-component of the spin. Such selective behavior can be applied to spin transport devices. However, the anomalous transport phenomena along the chiral axis or in the perpendicular plane resulted in vanishingly small in $LaBPt_2$. In the case of the TRS breaking $NdBPt_2$, as expected, the magnetism induced a strong AHC component in the plane perpendicular to the magnetic symmetry axis, reaching more than 200 S/cm. The remaining components showed a similar behavior to $LaBPt_2$. This result is coherent with the strong AHC in ferromagnets reported by other authors. Thus, the results suggest a weak inference of chirality in the AHC in chiral crystals beyond the removal of IS. Again, as in the case of the Γ_{4g} phase of Mn_3NiN, the Weyl nodes near the Fermi level seemed unrelated to the AHC magnitude. Nevertheless, a more in-depth study of the AHC in chiral crystals is still needed to discard the impact of chirality on the AHC. For example, a study of a zero net magnetization ordering in $NdBPt_2$ would bring more clarity to this issue.

Overall, chirality serves the purpose of removing the IS. In chiral noncollinear antiferromagnets, such IS breaking is crucial for adding AHC on top of the already known

functionalities they hold. Therefore, to establish AHC in these compounds, a combination of vector chirality from the magnetic ordering and a nonvanishing Berry curvature is required. Moreover, the AHC and the strain link exist through the BC in the kagome lattice plane, responsible for the chirality in these compounds, leaving the chirality as the intermediary entity in the multifunctionality typical of the chiral noncollinear antiperovskites. In chiral crystals, the results obtained so far withdraws the chirality as a trigger to the AHC. These compounds still need a net magnetization in order to display AHC. These results still need confirmation in other magnetic orderings of the ternary magnetic compound.

After the results obtained during this research work, I expect to see compounds such as Mn_3NiN in straintronics applications where its switchable AHC, turned on/off with compression/tension strain, can serve as a control mechanism. Regarding the chiral crystals, the effect of chirality still has a lot of areas to be explored. For example, due to the lack of inversion symmetry, the chiral crystals are expected to be polar and hold ferroelectricity. Spin selective transport phenomena, as observed in the direction parallel to the screw axis, can find an application in spintronics.

Chapter 7

Appendices

7.1 Additional data for nonmagnetic chiral compounds

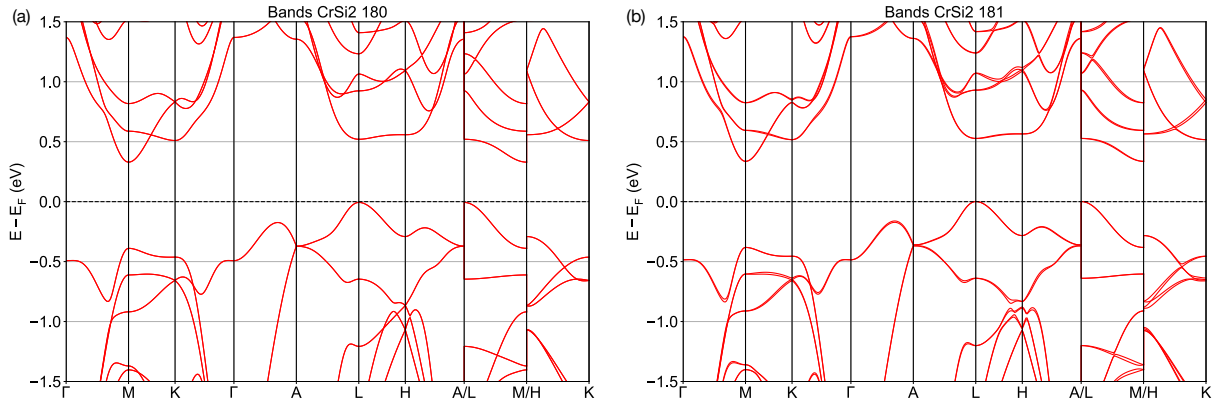

Figure 7.1: *Band structure for the enantiomeric $CrSi_2$ crystal with chiral SGs 180 and 181.*

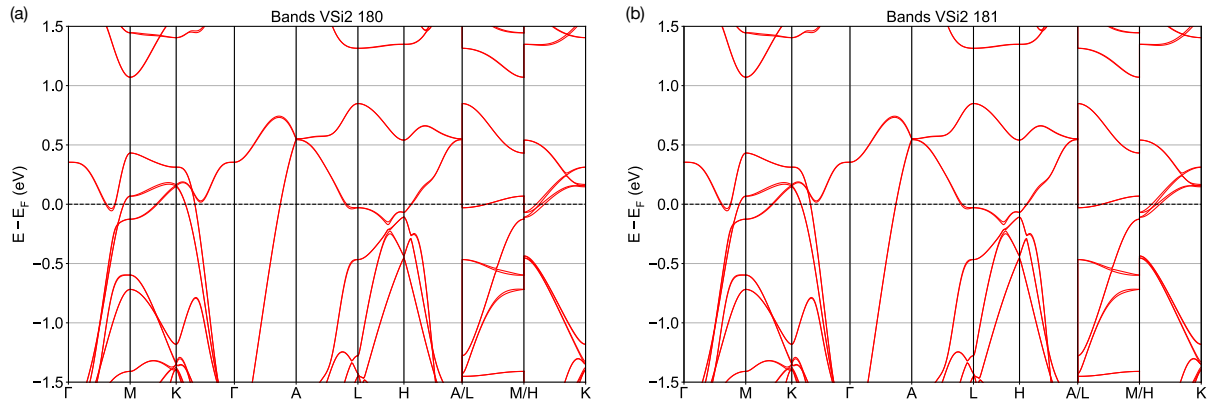

Figure 7.2: *Band structure for the enantiomeric VSi_2 crystal with chiral SGs 180 and 181.*

Table 7.1: *Lattice parameters in Å for the chiral non magnetic compounds.*

Compound	a	b	c
ZnTe(144)	4.29140	4.29138	10.51156
ZnTe(181)	4.26350	4.26350	9.56787
HgS(152)	4.14426	4.14426	9.39697
HgS(154)	4.14429	4.14429	9.39710
$CrSi_2$(180)	4.36684	4.36683	6.31583
$CrSi_2$(181)	4.36668	4.36668	6.31568
VSi_2(180)	4.52473	4.52473	6.32681
VSi_2(181)	4.52473	4.52472	6.32678

7.2 Magnetic subgroups of $NdBPt_2$

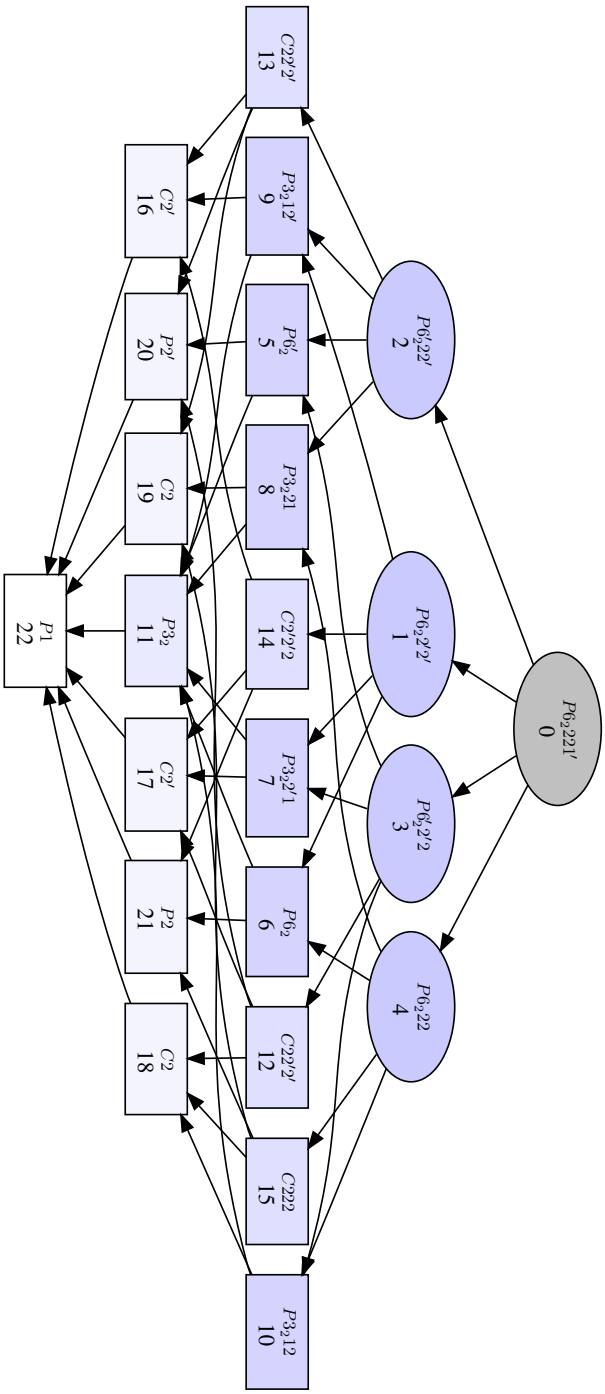

Figure 7.3: *Magnetic subgroups for $NdBPt_2$ with chiral SGs 180 and 181. Obtained with the k-Subgroupsmag tool od the Bilbao crystallographic server*

Bibliography

[1] Manfred Fiebig. THE EVOLUTION OF MULTIFERROICS. *Nature Reviews Materials*, page 16046, 2016. ISSN 2058-8437. doi: 10.1038/natrevmats.2016.46. URL http://e-citations.ethbib.ethz.ch/view/pub:179879.

[2] N. A. Spaldin and R. Ramesh. Advances in magnetoelectric multiferroics. *Nature Materials*, 18(3):203–212, March 2019. ISSN 1476-4660. doi: 10.1038/s41563-018-0275-2. URL https://doi.org/10.1038/s41563-018-0275-2.

[3] Silvia Picozzi. Ferroelectric rashba semiconductors as a novel class of multifunctional materials. *Frontiers in Physics*, 2:10, 2014. ISSN 2296-424X. doi: 10.3389/fphy.2014.00010. URL https://www.frontiersin.org/article/10.3389/fphy.2014.00010.

[4] Hania Djani, Andres Camilo Garcia-Castro, Wen-Yi Tong, Paolo Barone, Eric Bousquet, Silvia Picozzi, and Philippe Ghosez. Rationalizing and engineering Rashba spin-splitting in ferroelectric oxides. *npj Quantum Materials*, 4(1):51, September 2019. ISSN 2397-4648. doi: 10.1038/s41535-019-0190-z. URL https://doi.org/10.1038/s41535-019-0190-z.

[5] T. Goto, T. Kimura, G. Lawes, A. P. Ramirez, and Y. Tokura. Ferroelectricity and giant magnetocapacitance in perovskite rare-earth manganites. *Phys. Rev. Lett.*, 92:257201, Jun 2004. doi: 10.1103/PhysRevLett.92.257201. URL https://link.aps.org/doi/10.1103/PhysRevLett.92.257201.

[6] Claude Ederer and Nicola A. Spaldin. Origin of ferroelectricity in the multiferroic barium fluorides Bamf_4: A first principles study. *Phys. Rev. B*, 74:024102, Jul 2006. doi: 10.1103/PhysRevB.74.024102. URL http://link.aps.org/doi/10.1103/PhysRevB.74.024102.

[7] Claude Ederer and Nicola A. Spaldin. Electric-field-switchable magnets: The case of banif$_4$. *Phys. Rev. B*, 74:020401, Jul 2006. doi: 10.1103/PhysRevB.74.020401. URL http://link.aps.org/doi/10.1103/PhysRevB.74.020401.

[8] A. Scaramucci, E. Bousquet, M. Fechner, M. Mostovoy, and N. A. Spaldin. Linear magnetoelectric effect by orbital magnetism. *Phys. Rev. Lett.*, 109:197203, Nov 2012. doi: 10.1103/PhysRevLett.109.197203. URL https://link.aps.org/doi/10.1103/PhysRevLett.109.197203.

[9] Eric Bousquet, Nicola A. Spaldin, and Kris T. Delaney. Unexpectedly large electronic contribution to linear magnetoelectricity. *Phys. Rev. Lett.*, 106:107202, Mar 2011. doi: 10.1103/PhysRevLett.106.107202. URL https://link.aps.org/doi/10.1103/PhysRevLett.106.107202.

[10] David Ayuso, Ofer Neufeld, Andres F. Ordonez, Piero Decleva, Gavriel Lerner, Oren Cohen, Misha Ivanov, and Olga Smirnova. Synthetic chiral light for efficient control of chiral light–matter interaction. *Nature Photonics*, 13(12):866–871, December 2019. ISSN 1749-4893. doi: 10.1038/s41566-019-0531-2. URL https://doi.org/10.1038/s41566-019-0531-2.

[11] Z. Q. Liu, H. Chen, J. M. Wang, J. H. Liu, K. Wang, Z. X. Feng, H. Yan, X. R. Wang, C. B. Jiang, J. M. D. Coey, and A. H. MacDonald. Electrical switching of the topological anomalous Hall effect in a non-collinear antiferromagnet above room temperature. *Nature Electronics*, 1(3):172–177, March 2018. ISSN 2520-1131. doi: 10.1038/s41928-018-0040-1. URL https://doi.org/10.1038/s41928-018-0040-1.

[12] Xiaodong Zhou, Jan-Philipp Hanke, Wanxiang Feng, Fei Li, Guang-Yu Guo, Yugui Yao, Stefan Blügel, and Yuriy Mokrousov. Spin-order dependent anomalous hall effect and magneto-optical effect in the noncollinear antiferromagnets mn$_3x$N with x = Ga, zn, ag, or ni. *Phys. Rev. B*, 99:104428, Mar 2019. doi: 10.1103/PhysRevB.99.104428. URL https://link.aps.org/doi/10.1103/PhysRevB.99.104428.

[13] Harish K. Singh, Ilias Samathrakis, Nuno M. Fortunato, Jan Zemen, Chen Shen, Oliver Gutfleisch, and Hongbin Zhang. Multifunctional antiperovskites driven by strong magnetostructural coupling. *npj Computational Materials*, 7(1):98, June 2021. ISSN 2057-3960. doi: 10.1038/s41524-021-00566-w. URL https://doi.org/10.1038/s41524-021-00566-w.

[14] Ajaya K. Nayak, Julia Erika Fischer, Yan Sun, Binghai Yan, Julie Karel, Alexander C. Komarek, Chandra Shekhar, Nitesh Kumar, Walter Schnelle, Jürgen Kübler, Claudia Felser, and Stuart S. P. Parkin. Large anomalous hall effect driven by a nonvanishing berry curvature in the noncolinear antiferromagnet mn¡sub¿3¡/sub¿ge. *Science Advances*, 2(4):e1501870, 2016. doi: 10.1126/sciadv.1501870. URL https://www.science.org/doi/abs/10.1126/sciadv.1501870.

[15] Tuhin Kumar Maji, Kumar Vaibhav, Samir Kumar Pal, and Debjani Karmakar. Broken symmetries and the related interface-induced effects at Weyl-system TaAs in proximity of noble metals. *Scientific Reports*, 10(1):14438, September 2020. ISSN 2045-2322. doi: 10.1038/s41598-020-71494-w. URL https://doi.org/10.1038/s41598-020-71494-w.

[16] Stefanos Kourtis. Bulk spectroscopic measurement of the topological charge of weyl nodes with resonant x rays. *Phys. Rev. B*, 94:125132, Sep 2016. doi: 10.1103/PhysRevB.94.125132. URL https://link.aps.org/doi/10.1103/PhysRevB.94.125132.

[17] Sobhit Singh, A. C. Garcia-Castro, Irais Valencia-Jaime, Francisco Muñoz, and Aldo H. Romero. Prediction and control of spin polarization in a weyl semimetallic phase of bisb. *Phys. Rev. B*, 94:161116, Oct 2016. doi: 10.1103/PhysRevB.94.161116. URL https://link.aps.org/doi/10.1103/PhysRevB.94.161116.

[18] Libor Šmejkal, Yuriy Mokrousov, Binghai Yan, and Allan H. MacDonald. Topological antiferromagnetic spintronics. *Nature Physics*, 14(3):242–251, March 2018. ISSN 1745-2481. doi: 10.1038/s41567-018-0064-5. URL https://doi.org/10.1038/s41567-018-0064-5.

[19] Stanislav Chadov, Xiaoliang Qi, Jürgen Kübler, Gerhard H. Fecher, Claudia Felser, and Shou Cheng Zhang. Tunable multifunctional topological insulators in ternary Heusler compounds. *Nature Materials*, 9(7):541–545, July 2010. ISSN 1476-4660. doi: 10.1038/nmat2770. URL https://doi.org/10.1038/nmat2770.

[20] M Zahid Hasan, Su-Yang Xu, and Guang Bian. Topological insulators, topological superconductors and weyl fermion semimetals: discoveries, perspectives and outlooks. *Physica Scripta*, 2015(T164):014001, sep 2015. doi: 10.1088/0031-8949/2015/T164/014001. URL https://dx.doi.org/10.1088/0031-8949/2015/T164/014001.

[21] Shinichi Itoh, Yasuo Endoh, Tetsuya Yokoo, Soshi Ibuka, Je-Geun Park, Yoshio Kaneko, Kei S. Takahashi, Yoshinori Tokura, and Naoto Nagaosa. Weyl fermions and spin dynamics of metallic ferromagnet SrRuO3. *Nature Communications*, 7(1):11788, June 2016. ISSN 2041-1723. doi: 10.1038/ncomms11788. URL https://doi.org/10.1038/ncomms11788.

[22] A. B. Harris, Randall D. Kamien, and T. C. Lubensky. Molecular chirality and chiral parameters. *Rev. Mod. Phys.*, 71:1745–1757, Oct 1999. doi: 10.1103/RevModPhys.71.1745. URL https://link.aps.org/doi/10.1103/RevModPhys.71.1745.

[23] G. Gatti, D. Gosálbez-Martínez, S. S. Tsirkin, M. Fanciulli, M. Puppin, S. Polishchuk, S. Moser, L. Testa, E. Martino, S. Roth, Ph. Bugnon, L. Moreschini, A. Bostwick, C. Jozwiak, E. Rotenberg, G. Di Santo, L. Petaccia, I. Vobornik, J. Fujii, J. Wong, D. Jariwala, H. A. Atwater, H. M. Rønnow, M. Chergui, O. V. Yazyev, M. Grioni, and A. Crepaldi. Radial spin texture of the weyl fermions in chiral tellurium. *Phys. Rev. Lett.*, 125:216402, Nov 2020. doi: 10.1103/PhysRevLett.125.216402. URL https://link.aps.org/doi/10.1103/PhysRevLett.125.216402.

[24] Roderich Moessner and Arthur P. Ramirez. Geometrical frustration. *Physics Today*, 59(2):24–29, 2006. doi: 10.1063/1.2186278. URL https://doi.org/10.1063/1.2186278.

[25] H Kawamura. Spin- and chirality-orderings of frustrated magnets stacked-triangular anti-ferromagnets and spin glasses. *Canadian Journal of Physics*, 79 (11-12):1447–1458, 2001. doi: 10.1139/p01-111. URL https://doi.org/10.1139/p01-111.

[26] Wen Fong Goh and Warren E. Pickett. Coemergence of dirac and multi-weyl topological excitations in pnictide antiperovskites. *Phys. Rev. B*, 98:125147, Sep 2018. doi: 10.1103/PhysRevB.98.125147. URL https://link.aps.org/doi/10.1103/PhysRevB.98.125147.

[27] Sergey V. Krivovichev. Minerals with antiperovskite structure: a review. *Zeitschrift für Kristallographie - Crystalline Materials*, 223(1-2):109–113, 2008. doi: doi:10.1524/zkri.2008.0008. URL https://doi.org/10.1524/zkri.2008.0008.

[28] Yonggang Wang, Hao Zhang, Jinlong Zhu, Xujie Lü, Shuai Li, Ruqiang Zou, and Yusheng Zhao. Antiperovskites with exceptional functionalities. *Advanced Materials*, 32(7):1905007, 2020. doi: https://doi.org/10.1002/adma.201905007. URL https://onlinelibrary.wiley.com/doi/abs/10.1002/adma.201905007.

[29] Yusheng Zhao and Luke L. Daemen. Superionic conductivity in lithium-rich anti-perovskites. *Journal of the American Chemical Society*, 134(36):15042–15047, 2012. doi: 10.1021/ja305709z. URL https://doi.org/10.1021/ja305709z. PMID: 22849550.

[30] K. Takenaka, T. Hamada, D. Kasugai, and N. Sugimoto. Tailoring thermal expansion in metal matrix composites blended by antiperovskite manganese nitrides exhibiting giant negative thermal expansion. *Journal of Applied Physics*, 112(8):083517, 2012. doi: 10.1063/1.4759121. URL https://doi.org/10.1063/1.4759121.

[31] A. C. Garcia-Castro, R. Ospina, and J. H. Quintero. Octahedral distortion and electronic properties of the antiperovskite oxide Ba_3SiO: First principles study. *Journal of Physics and Chemistry of Solids*, 136(April 2019):109126, 2020. ISSN 00223697. doi: 10.1016/j.jpcs.2019.109126. URL https://doi.org/10.1016/j.jpcs.2019.109126.

[32] Andrés Camilo Garcia-Castro, Jorge Hernan Quintero Orozco, and Carlos José Paez Gonzalez. Hybrid-improper ferroelectric behavior in Ba3SiO/Ba3GeO oxide antiperovskite superlattices. *The European Physical Journal B*, 92(9):203, September 2019. ISSN 1434-6036. doi: 10.1140/epjb/e2019-100175-1. URL https://doi.org/10.1140/epjb/e2019-100175-1.

[33] L. L. Boyer and P. J. Edwardson. Perovskite to antiperovskite in abf3 compounds. *Ferroelectrics*, 104(1):417–422, 1990. doi: 10.1080/00150199008223849. URL https://doi.org/10.1080/00150199008223849.

[34] Pavel Lukashev, Renat F. Sabirianov, and Kirill Belashchenko. Theory of the piezomagnetic effect in mn-based antiperovskites. *Phys. Rev. B*, 78:184414, Nov 2008. doi: 10.1103/PhysRevB.78.184414. URL https://link.aps.org/doi/10.1103/PhysRevB.78.184414.

[35] Hongbo Liu and Xue Yang. A brief review on perovskite multiferroics. *Ferroelectrics*, 507(1):69–85, 2017. doi: 10.1080/00150193.2017.1283171. URL https://doi.org/10.1080/00150193.2017.1283171.

[36] Nicola A. Spaldin, Sang-Wook Cheong, and Ramamoorthy Ramesh. Multiferroics: Past, present, and future. *Physics Today*, 63(10):38–43, 2010. doi: 10.1063/1.3502547. URL https://doi.org/10.1063/1.3502547.

[37] Tianhao Wu, Zhenzhen Qin, Yanbo Wang, Yongzhen Wu, Wei Chen, Shufang Zhang, Molang Cai, Songyuan Dai, Jing Zhang, Jian Liu, Zhongmin Zhou, Xiao Liu, Hiroshi Segawa, Hairen Tan, Qunwei Tang, Junfeng Fang, Yaowen Li, Liming Ding, Zhijun Ning, Yabing Qi, Yiqiang Zhang, and Liyuan Han. The Main Progress of Perovskite Solar Cells in 2020–2021. *Nano-Micro Letters*, 13(1):152, July 2021. ISSN 2150-5551. doi: 10.1007/s40820-021-00672-w. URL https://doi.org/10.1007/s40820-021-00672-w.

[38] Jin Young Kim, Jin-Wook Lee, Hyun Suk Jung, Hyunjung Shin, and Nam-Gyu Park. High-Efficiency Perovskite Solar Cells. *Chemical Reviews*, 120(15): 7867–7918, August 2020. ISSN 0009-2665. doi: 10.1021/acs.chemrev.0c00107. URL https://doi.org/10.1021/acs.chemrev.0c00107. Publisher: American Chemical Society.

[39] David Boldrin, Ilias Samathrakis, Jan Zemen, Andrei Mihai, Bin Zou, Freya Johnson, Bryan D. Esser, David W. McComb, Peter K. Petrov, Hongbin Zhang, and Lesley F. Cohen. Anomalous hall effect in noncollinear antiferromagnetic Mn_3NiN thin films. *Phys. Rev. Materials*, 3:094409, Sep 2019. doi: 10.1103/PhysRevMaterials.3.094409. URL https://link.aps.org/doi/10.1103/PhysRevMaterials.3.094409.

[40] Gautam Gurung, Ding-Fu Shao, Tula R. Paudel, and Evgeny Y. Tsymbal. Anomalous hall conductivity of noncollinear magnetic antiperovskites. *Phys.*

Rev. Materials, 3:044409, Apr 2019. doi: 10.1103/PhysRevMaterials.3.044409. URL https://link.aps.org/doi/10.1103/PhysRevMaterials.3.044409.

[41] Tong Peng, Wang Bo-Sen, and Sun Yu-Ping. Mn-based antiperovskite functional materials: Review of research. *Chinese Physics B*, 22(6):067501, 2013. doi: 10.1088/1674-1056/22/6/067501. URL http://cpb.iphy.ac.cn/EN/abstract/article_114986.shtml.

[42] David Boldrin, Andrei P. Mihai, Bin Zou, Jan Zemen, Ryan Thompson, Ecaterina Ware, Bogdan V. Neamtu, Luis Ghivelder, Bryan Esser, David W. McComb, Peter Petrov, and Lesley F. Cohen. Giant piezomagnetism in mn3nin. *ACS Applied Materials & Interfaces*, 10(22):18863–18868, 2018. doi: 10.1021/acsami.8b03112. URL https://doi.org/10.1021/acsami.8b03112. PMID: 29726252.

[43] D. Fruchart and E. F. Bertaut. Magnetic studies of the metallic perovskite-type compounds of manganese. *Journal of the Physical Society of Japan*, 44(3):781–791, 1978. doi: 10.1143/JPSJ.44.781. URL https://doi.org/10.1143/JPSJ.44.781.

[44] J. Zemen, E. Mendive-Tapia, Z. Gercsi, R. Banerjee, J. B. Staunton, and K. G. Sandeman. Frustrated magnetism and caloric effects in mn-based antiperovskite nitrides: Ab initio theory. *Phys. Rev. B*, 95:184438, May 2017. doi: 10.1103/PhysRevB.95.184438. URL https://link.aps.org/doi/10.1103/PhysRevB.95.184438.

[45] G. Kresse and J. Furthmüller. Efficient iterative schemes for *ab initio* total-energy calculations using a plane-wave basis set. *Phys. Rev. B*, 54:11169–11186, Oct 1996. doi: 10.1103/PhysRevB.54.11169. URL http://link.aps.org/doi/10.1103/PhysRevB.54.11169.

[46] G. Kresse and D. Joubert. From ultrasoft pseudopotentials to the projector augmented-wave method. *Phys. Rev. B*, 59:1758–1775, Jan 1999. doi: 10.1103/

PhysRevB.59.1758. URL http://link.aps.org/doi/10.1103/PhysRevB.59.1758.

[47] Nicole A. Benedek, James M. Rondinelli, Hania Djani, Philippe Ghosez, and Philip Lightfoot. Understanding ferroelectricity in layered perovskites: new ideas and insights from theory and experiments. *Dalton Trans.*, 44:10543–10558, 2015. doi: 10.1039/C5DT00010F. URL http://dx.doi.org/10.1039/C5DT00010F.

[48] Nicole A. Benedek, Andrew T. Mulder, and Craig J. Fennie. Polar octahedral rotations: A path to new multifunctional materials. *Journal of Solid State Chemistry*, 195:11 – 20, 2012. ISSN 0022-4596. doi: http://dx.doi.org/10.1016/j.jssc.2012.04.012. URL http://www.sciencedirect.com/science/article/pii/S0022459612002599. Polar Inorganic Materials: Design Strategies and Functional Properties.

[49] Shugang Tan, Chenhao Gao, Hao Yuan, Jinpeng Wu, Cao Wang, Rui Cao, and Yuping Sun. An antiperovskite compound with multifunctional properties: Mn3pdn. *Journal of Solid State Chemistry*, 302:122389, 2021. ISSN 0022-4596. doi: https://doi.org/10.1016/j.jssc.2021.122389. URL https://www.sciencedirect.com/science/article/pii/S0022459621004345.

[50] Roger Hegstrom and Dilip Kondepudi. The handedness of the universe. *Scientific American*, 262, 01 1990. doi: 10.1038/scientificamerican0190-108.

[51] Dilip K. Kondepudi and Daniel J. Durand. Chiral asymmetry in spiral galaxies? *Chirality*, 13(7):351–356, 2001. doi: https://doi.org/10.1002/chir.1044. URL https://onlinelibrary.wiley.com/doi/abs/10.1002/chir.1044.

[52] L. PASTEUR. Sur les relations qui peuvent exister entre la forme crystalline, la composition chimique et le sens de la polarization rotatoire. *Annales Chimie Phys.*, 24:442–459, 1848. URL https://ci.nii.ac.jp/naid/10009487760/en/.

[53] Jean-Baptiste Biot. *Sur la polarisation circulaire et sur ses applications à la chimie organique*. 1835.

[54] Louis Pasteur. *Recherches sur les propriétés spécifiques des deux acides qui composent l'acide racémique*. impr. Bachelier, 1850.

[55] Louis Pasteur. *Researches on the molecular asymmetry of natural organic products*. Number 14. WF Clay, 1897.

[56] Guoqing Chang, Benjamin J. Wieder, Frank Schindler, Daniel S. Sanchez, Ilya Belopolski, Shin-Ming Huang, Bahadur Singh, Di Wu, Tay-Rong Chang, Titus Neupert, Su-Yang Xu, Hsin Lin, and M. Zahid Hasan. Topological quantum properties of chiral crystals. *Nature Materials*, 17(11):978–985, November 2018. ISSN 1476-4660. doi: 10.1038/s41563-018-0169-3. URL https://doi.org/10.1038/s41563-018-0169-3.

[57] Chandra Shekhar. Chirality meets topology. *Nature Materials*, 17(11):953–954, November 2018. ISSN 1476-4660. doi: 10.1038/s41563-018-0210-6. URL https://doi.org/10.1038/s41563-018-0210-6.

[58] Dina Yogev-Einot and David Avnir. Quantitative symmetry and chirality of the molecular building blocks of quartz. *Chemistry of Materials*, 15(2):464–472, 2003. doi: 10.1021/cm0207806. URL https://doi.org/10.1021/cm0207806.

[59] S. M. L. Teicher, I. K. Svenningsson, L. M. Schoop, and R. Seshadri. Weyl nodes and magnetostructural instability in antiperovskite mn3znc. *APL Materials*, 7 (12):121104, 2019. doi: 10.1063/1.5129689. URL https://doi.org/10.1063/1.5129689.

[60] R.G. Butters and H.P. Myers. Xvii. the structure and properties of some ternary alloys of manganese, zinc and carbon. *The London, Edinburgh, and Dublin Philosophical Magazine and Journal of Science*, 46(373):132–143, 1955. doi: 10.1080/14786440208520557. URL https://doi.org/10.1080/14786440208520557.

[61] B. N. Brockhouse and H. P. Myers. New type of magnetic transition in mn3znc. *Canadian Journal of Physics*, 35(3):313–323, 1957. doi: 10.1139/p57-035. URL https://doi.org/10.1139/p57-035.

[62] Takejiro Kaneko, Takeshi Kanomata, and Kiwamu Shirakawa. Pressure effect on the magnetic transition temperatures in the intermetallic compounds mn3mc (m=ga, zn and sn). *Journal of the Physical Society of Japan*, 56(11):4047–4055, 1987. doi: 10.1143/JPSJ.56.4047. URL https://doi.org/10.1143/JPSJ.56.4047.

[63] AR Fert. Magnetic and transport properties of metallic multilayers. In *Materials Science Forum*, volume 59, pages 439–480. Trans Tech Publ, 1990.

[64] M. Bode, M. Heide, K. von Bergmann, P. Ferriani, S. Heinze, G. Bihlmayer, A. Kubetzka, O. Pietzsch, S. Blügel, and R. Wiesendanger. Chiral magnetic order at surfaces driven by inversion asymmetry. *Nature*, 447(7141):190–193, May 2007. ISSN 1476-4687. doi: 10.1038/nature05802. URL https://doi.org/10.1038/nature05802.

[65] Masaya Uchida, Yoshinori Onose, Yoshio Matsui, and Yoshinori Tokura. Real-space observation of helical spin order. *Science*, 311(5759):359–361, 2006. doi: 10.1126/science.1120639. URL https://www.science.org/doi/abs/10.1126/science.1120639.

[66] Takumi Ogawa, Kazuki Uematsu, and Hikaru Kawamura. Monte carlo studies of the spin-chirality decoupling in the three-dimensional heisenberg spin glass. *Phys. Rev. B*, 101:014434, Jan 2020. doi: 10.1103/PhysRevB.101.014434. URL https://link.aps.org/doi/10.1103/PhysRevB.101.014434.

[67] Ian A. Campbell and Dorothée C. M. C. Petit. Heisenberg spin glass experiments and the chiral ordering scenario. *Journal of the Physical Society of Japan*, 79(1):011006, 2010. doi: 10.1143/JPSJ.79.011006. URL https://doi.org/10.1143/JPSJ.79.011006.

[68] Hikaru Kawamura. Chiral ordering in heisenberg spin glasses in two and three dimensions. *Phys. Rev. Lett.*, 68:3785–3788, Jun 1992. doi: 10.1103/PhysRevLett.68.3785. URL https://link.aps.org/doi/10.1103/PhysRevLett.68.3785.

[69] Laurence D. Barron. Chirality and magnetism shake hands. *Nature Materials*, 7(9):691–692, September 2008. ISSN 1476-4660. doi: 10.1038/nmat2263. URL https://doi.org/10.1038/nmat2263.

[70] Barbara Goss Levi. New candidate emerges for a quantum spin liquid. *Physics Today*, 60(2):16–19, 2007. doi: 10.1063/1.2711623. URL https://doi.org/10.1063/1.2711623.

[71] Alexander Mook, Jürgen Henk, and Ingrid Mertig. Magnon hall effect and topology in kagome lattices: A theoretical investigation. *Phys. Rev. B*, 89:134409, Apr 2014. doi: 10.1103/PhysRevB.89.134409. URL https://link.aps.org/doi/10.1103/PhysRevB.89.134409.

[72] D. F. Liu, A. J. Liang, E. K. Liu, Q. N. Xu, Y. W. Li, C. Chen, D. Pei, W. J. Shi, S. K. Mo, P. Dudin, T. Kim, C. Cacho, G. Li, Y. Sun, L. X. Yang, Z. K. Liu, S. S. P. Parkin, C. Felser, and Y. L. Chen. Magnetic weyl semimetal phase in a kagome crystal. *Science*, 365(6459):1282–1285, 2019. doi: 10.1126/science.aav2873. URL https://www.science.org/doi/abs/10.1126/science.aav2873.

[73] Noam Morali, Rajib Batabyal, Pranab Kumar Nag, Enke Liu, Qiunan Xu, Yan Sun, Binghai Yan, Claudia Felser, Nurit Avraham, and Haim Beidenkopf. Fermi-arc diversity on surface terminations of the magnetic weyl semimetal Co3Sn2S2. *Science*, 365(6459):1286–1291, 2019. doi: 10.1126/science.aav2334. URL https://www.science.org/doi/abs/10.1126/science.aav2334.

[74] Domenico Di Sante, Paolo Barone, Alessandro Stroppa, Kevin F. Garrity, David Vanderbilt, and Silvia Picozzi. Intertwined rashba, dirac, and weyl fermions

in hexagonal hyperferroelectrics. *Phys. Rev. Lett.*, 117:076401, Aug 2016. doi: 10.1103/PhysRevLett.117.076401. URL https://link.aps.org/doi/10.1103/PhysRevLett.117.076401.

[75] Jianpeng Liu and David Vanderbilt. Weyl semimetals from noncentrosymmetric topological insulators. *Phys. Rev. B*, 90:155316, Oct 2014. doi: 10.1103/PhysRevB.90.155316. URL https://link.aps.org/doi/10.1103/PhysRevB.90.155316.

[76] J.-Y. Chauleau, T. Chirac, S. Fusil, V. Garcia, W. Akhtar, J. Tranchida, P. Thibaudeau, I. Gross, C. Blouzon, A. Finco, M. Bibes, B. Dkhil, D. D. Khalyavin, P. Manuel, V. Jacques, N. Jaouen, and M. Viret. Electric and antiferromagnetic chiral textures at multiferroic domain walls. *Nature Materials*, 19 (4):386–390, April 2020. ISSN 1476-4660. doi: 10.1038/s41563-019-0516-z. URL https://doi.org/10.1038/s41563-019-0516-z.

[77] Sergey Borisenko, Daniil Evtushinsky, Quinn Gibson, Alexander Yaresko, Klaus Koepernik, Timur Kim, Mazhar Ali, Jeroen van den Brink, Moritz Hoesch, Alexander Fedorov, Erik Haubold, Yevhen Kushnirenko, Ivan Soldatov, Rudolf Schäfer, and Robert J. Cava. Time-reversal symmetry breaking type-II Weyl state in YbMnBi2. *Nature Communications*, 10(1):3424, July 2019. ISSN 2041-1723. doi: 10.1038/s41467-019-11393-5. URL https://doi.org/10.1038/s41467-019-11393-5.

[78] Cyrille Train, Ruxandra Gheorghe, Vojislav Krstic, Lise-Marie Chamoreau, Nikolai S. Ovanesyan, Geert L. J. A. Rikken, Michel Gruselle, and Michel Verdaguer. Strong magneto-chiral dichroism in enantiopure chiral ferromagnets. *Nature Materials*, 7(9):729–734, September 2008. ISSN 1476-4660. doi: 10.1038/nmat2256. URL https://doi.org/10.1038/nmat2256.

[79] Tobias Meng and Leon Balents. Weyl superconductors. *Phys. Rev. B*, 86:054504,

Aug 2012. doi: 10.1103/PhysRevB.86.054504. URL https://link.aps.org/doi/10.1103/PhysRevB.86.054504.

[80] Yanpeng Qi, Pavel G. Naumov, Mazhar N. Ali, Catherine R. Rajamathi, Walter Schnelle, Oleg Barkalov, Michael Hanfland, Shu-Chun Wu, Chandra Shekhar, Yan Sun, Vicky Süß, Marcus Schmidt, Ulrich Schwarz, Eckhard Pippel, Peter Werner, Reinald Hillebrand, Tobias Förster, Erik Kampert, Stuart Parkin, R. J. Cava, Claudia Felser, Binghai Yan, and Sergey A. Medvedev. Superconductivity in Weyl semimetal candidate MoTe2. *Nature Communications*, 7(1):11038, March 2016. ISSN 2041-1723. doi: 10.1038/ncomms11038. URL https://doi.org/10.1038/ncomms11038.

[81] S. Pancharatnam. Generalized theory of interference, and its applications. *Proceedings of the Indian Academy of Sciences - Section A*, 44(5):247–262, November 1956. ISSN 0370-0089. doi: 10.1007/BF03046050. URL https://doi.org/10.1007/BF03046050.

[82] Michael Victor Berry. Quantal phase factors accompanying adiabatic changes. *Proceedings of the Royal Society of London. A. Mathematical and Physical Sciences*, 392(1802):45–57, 1984. doi: 10.1098/rspa.1984.0023. URL https://royalsocietypublishing.org/doi/abs/10.1098/rspa.1984.0023.

[83] Xinjie Wang, David Vanderbilt, Jonathan R. Yates, and Ivo Souza. Fermi-surface calculation of the anomalous hall conductivity. *Phys. Rev. B*, 76:195109, Nov 2007. doi: 10.1103/PhysRevB.76.195109. URL https://link.aps.org/doi/10.1103/PhysRevB.76.195109.

[84] D. Torres-Amaris, A. Bautista-Hernandez, Rafael González-Hernández, Aldo H. Romero, and A. C. Garcia-Castro. Anomalous hall conductivity control in Mn3NiN antiperovskite by epitaxial strain along the kagome plane. *Phys. Rev. B*, 106:195113, Nov 2022. doi: 10.1103/PhysRevB.106.195113. URL https://link.aps.org/doi/10.1103/PhysRevB.106.195113.

[85] David Boldrin, Freya Johnson, Ryan Thompson, Andrei P. Mihai, Bin Zou, Jan Zemen, Jack Griffiths, Patrik Gubeljak, Kristian L. Ormandy, Pascal Manuel, Dmitry D. Khalyavin, Bachir Ouladdiaf, Navid Qureshi, Peter Petrov, Will Branford, and Lesley F. Cohen. The Biaxial Strain Dependence of Magnetic Order in Spin Frustrated Mn_3NiN Thin Films. *Advanced Functional Materials*, 29(40): 2–7, 2019. ISSN 16163028. doi: 10.1002/adfm.201902502.

[86] R. D. Gonzalez Betancourt, J. Zubáč, R. Gonzalez-Hernandez, K. Geishendorf, Z. Šobáň, G. Springholz, K. Olejník, L. Šmejkal, J. Sinova, T. Jungwirth, S. T. B. Goennenwein, A. Thomas, H. Reichlová, J. Železný, and D. Kriegner. Spontaneous anomalous hall effect arising from an unconventional compensated magnetic phase in a semiconductor. *Phys. Rev. Lett.*, 130:036702, Jan 2023. doi: 10.1103/PhysRevLett.130.036702. URL https://link.aps.org/doi/10.1103/PhysRevLett.130.036702.

[87] Monika Stanke and Ludwik Adamowicz. Molecular relativistic corrections determined in the framework where the born–oppenheimer approximation is not assumed. *The Journal of Physical Chemistry A*, 117(39):10129–10137, 2013. doi: 10.1021/jp4020492. URL https://doi.org/10.1021/jp4020492. PMID: 23679131.

[88] P. Hohenberg and W. Kohn. Inhomogeneous electron gas. *Phys. Rev.*, 136: B864–B871, Nov 1964. doi: 10.1103/PhysRev.136.B864. URL https://link.aps.org/doi/10.1103/PhysRev.136.B864.

[89] W. Kohn and L. J. Sham. Self-consistent equations including exchange and correlation effects. *Phys. Rev.*, 140:A1133–A1138, Nov 1965. doi: 10.1103/PhysRev.140.A1133. URL https://link.aps.org/doi/10.1103/PhysRev.140.A1133.

[90] Christoph R. Jacob and Markus Reiher. Spin in density-functional theory. *International Journal of Quantum Chemistry*, 112(23):3661–3684, 2012. doi:

https://doi.org/10.1002/qua.24309. URL https://onlinelibrary.wiley.com/doi/abs/10.1002/qua.24309.

[91] Feliciano Giustino. *Materials modelling using density functional theory: properties and predictions*. Oxford University Press, 2014.

[92] Richard M Martin and Richard Milton Martin. *Electronic structure: basic theory and practical methods*. Cambridge university press, 2004.

[93] John P. Perdew, Kieron Burke, and Matthias Ernzerhof. Generalized gradient approximation made simple. *Phys. Rev. Lett.*, 77:3865–3868, Oct 1996. doi: 10.1103/PhysRevLett.77.3865. URL https://link.aps.org/doi/10.1103/PhysRevLett.77.3865.

[94] John P. Perdew, Adrienn Ruzsinszky, Gábor I. Csonka, Oleg A. Vydrov, Gustavo E. Scuseria, Lucian A. Constantin, Xiaolan Zhou, and Kieron Burke. Restoring the density-gradient expansion for exchange in solids and surfaces. *Phys. Rev. Lett.*, 100:136406, Apr 2008. doi: 10.1103/PhysRevLett.100.136406. URL http://link.aps.org/doi/10.1103/PhysRevLett.100.136406.

[95] Jianwei Sun, Adrienn Ruzsinszky, and John P. Perdew. Strongly constrained and appropriately normed semilocal density functional. *Phys. Rev. Lett.*, 115:036402, Jul 2015. doi: 10.1103/PhysRevLett.115.036402. URL https://link.aps.org/doi/10.1103/PhysRevLett.115.036402.

[96] Jochen Heyd, Gustavo E. Scuseria, and Matthias Ernzerhof. Hybrid functionals based on a screened coulomb potential. *The Journal of Chemical Physics*, 118(18):8207–8215, 2003. doi: 10.1063/1.1564060. URL https://doi.org/10.1063/1.1564060.

[97] Aliaksandr V. Krukau, Oleg A. Vydrov, Artur F. Izmaylov, and Gustavo E. Scuseria. Influence of the exchange screening parameter on the performance of

screened hybrid functionals. *The Journal of Chemical Physics*, 125(22):224106, 2006. doi: 10.1063/1.2404663. URL https://doi.org/10.1063/1.2404663.

[98] John P. Perdew, Adrienn Ruzsinszky, Jianmin Tao, Viktor N. Staroverov, Gustavo E. Scuseria, and Gábor I. Csonka. Prescription for the design and selection of density functional approximations: More constraint satisfaction with fewer fits. *The Journal of Chemical Physics*, 123(6):062201, 2005. doi: 10.1063/1.1904565. URL https://doi.org/10.1063/1.1904565.

[99] Gregory H. Wannier. The structure of electronic excitation levels in insulating crystals. *Phys. Rev.*, 52:191–197, Aug 1937. doi: 10.1103/PhysRev.52.191. URL https://link.aps.org/doi/10.1103/PhysRev.52.191.

[100] Gregory H. Wannier. Dynamics of band electrons in electric and magnetic fields. *Rev. Mod. Phys.*, 34:645–655, Oct 1962. doi: 10.1103/RevModPhys.34.645. URL https://link.aps.org/doi/10.1103/RevModPhys.34.645.

[101] Giovanni Pizzi, Valerio Vitale, Ryotaro Arita, Stefan Blügel, Frank Freimuth, Guillaume Géranton, Marco Gibertini, Dominik Gresch, Charles Johnson, Takashi Koretsune, Julen Ibañez-Azpiroz, Hyungjun Lee, Jae-Mo Lihm, Daniel Marchand, Antimo Marrazzo, Yuriy Mokrousov, Jamal I Mustafa, Yoshiro Nohara, Yusuke Nomura, Lorenzo Paulatto, Samuel Poncé, Thomas Ponweiser, Junfeng Qiao, Florian Thöle, Stepan S Tsirkin, Małgorzata Wierzbowska, Nicola Marzari, David Vanderbilt, Ivo Souza, Arash A Mostofi, and Jonathan R Yates. Wannier90 as a community code: new features and applications. *Journal of Physics: Condensed Matter*, 32(16):165902, jan 2020. doi: 10.1088/1361-648x/ab51ff. URL https://doi.org/10.1088%2F1361-648x%2Fab51ff.

[102] Stepan S. Tsirkin. High performance Wannier interpolation of Berry curvature and related quantities with WannierBerri code. *npj Computational Materials*, 7 (1):33, February 2021. ISSN 2057-3960. doi: 10.1038/s41524-021-00498-5. URL https://doi.org/10.1038/s41524-021-00498-5.

[103] Mats Johnsson and Peter Lemmens. *Crystallography and Chemistry of Perovskites*. John Wiley Sons, Ltd, 2007. ISBN 9780470022184. doi: https://doi.org/10.1002/9780470022184.hmm411. URL https://onlinelibrary.wiley.com/doi/abs/10.1002/9780470022184.hmm411.

[104] Tadao Kasuya. A Theory of Metallic Ferro- and Antiferromagnetism on Zener's Model. *Progress of Theoretical Physics*, 16(1):45–57, 07 1956. ISSN 0033-068X. doi: 10.1143/PTP.16.45. URL https://doi.org/10.1143/PTP.16.45.

[105] John B. Goodenough. Theory of the role of covalence in the perovskite-type manganites $[\mathrm{La}, m(\mathrm{II})]\mathrm{Mno}_3$. *Phys. Rev.*, 100:564–573, Oct 1955. doi: 10.1103/PhysRev.100.564. URL https://link.aps.org/doi/10.1103/PhysRev.100.564.

[106] Junjiro Kanamori. Superexchange interaction and symmetry properties of electron orbitals. *Journal of Physics and Chemistry of Solids*, 10(2):87–98, 1959. ISSN 0022-3697. doi: https://doi.org/10.1016/0022-3697(59)90061-7. URL https://www.sciencedirect.com/science/article/pii/0022369759900617.

[107] K. Matan, B. M. Bartlett, J. S. Helton, V. Sikolenko, S. Mat'aš, K. Prokeš, Y. Chen, J. W. Lynn, D. Grohol, T. J. Sato, M. Tokunaga, D. G. Nocera, and Y. S. Lee. Dzyaloshinskii-moriya interaction and spin reorientation transition in the frustrated kagome lattice antiferromagnet. *Phys. Rev. B*, 83:214406, Jun 2011. doi: 10.1103/PhysRevB.83.214406. URL https://link.aps.org/doi/10.1103/PhysRevB.83.214406.

[108] Daniel Grohol, Kittiwit Matan, Jin-Hyung Cho, Seung-Hun Lee, Jeffrey W. Lynn, Daniel G. Nocera, and Young S. Lee. Spin chirality on a two-dimensional frustrated lattice. *Nature Materials*, 4(4):323–328, April 2005. ISSN 1476-4660. doi: 10.1038/nmat1353. URL https://doi.org/10.1038/nmat1353.

[109] Toshiya Hikihara, Lars Kecke, Tsutomu Momoi, and Akira Furusaki. Vector chiral and multipolar orders in the spin-$\frac{1}{2}$ frustrated ferromagnetic chain in magnetic

field. *Phys. Rev. B*, 78:144404, Oct 2008. doi: 10.1103/PhysRevB.78.144404. URL https://link.aps.org/doi/10.1103/PhysRevB.78.144404.

[110] Naoki Kiyohara, Takahiro Tomita, and Satoru Nakatsuji. Giant anomalous hall effect in the chiral antiferromagnet mn_3Ge. *Phys. Rev. Applied*, 5:064009, Jun 2016. doi: 10.1103/PhysRevApplied.5.064009. URL https://link.aps.org/doi/10.1103/PhysRevApplied.5.064009.

[111] Satoru Nakatsuji, Naoki Kiyohara, and Tomoya Higo. Large anomalous Hall effect in a non-collinear antiferromagnet at room temperature. *Nature*, 527(7577): 212–215, November 2015. ISSN 1476-4687. doi: 10.1038/nature15723. URL https://doi.org/10.1038/nature15723.

[112] Aki Pulkkinen, Bernardo Barbiellini, Johannes Nokelainen, Vladimir Sokolovskiy, Danil Baigutlin, Olga Miroshkina, Mikhail Zagrebin, Vasiliy Buchelnikov, Christopher Lane, Robert S. Markiewicz, Arun Bansil, Jianwei Sun, Katariina Pussi, and Erkki Lähderanta. Coulomb correlation in noncollinear antiferromagnetic α-mn. *Phys. Rev. B*, 101:075115, Feb 2020. doi: 10.1103/PhysRevB.101.075115. URL https://link.aps.org/doi/10.1103/PhysRevB.101.075115.

[113] D. Hobbs, J. Hafner, and D. Spišák. Understanding the complex metallic element mn. i. crystalline and noncollinear magnetic structure of α-mn. *Phys. Rev. B*, 68: 014407, Jul 2003. doi: 10.1103/PhysRevB.68.014407. URL https://link.aps.org/doi/10.1103/PhysRevB.68.014407.

[114] L. Flórez-Gómez, W. Ibarra-Hernández, and A.C. Garcia-Castro. Lattice dynamics and spin–phonon coupling in the noncollinear antiferromagnetic antiperovskite Mn3NiN. *Journal of Magnetism and Magnetic Materials*, 562: 169813, 2022. ISSN 0304-8853. doi: https://doi.org/10.1016/j.jmmm.2022.169813. URL https://www.sciencedirect.com/science/article/pii/S0304885322007065.

[115] Haijun Zhang and Shou-Cheng Zhang. Topological insulators from the perspective of first-principles calculations. *physica status solidi (RRL) – Rapid Research Letters*, 7(1-2):72–81, 2013. doi: https://doi.org/10.1002/pssr.201206414. URL https://onlinelibrary.wiley.com/doi/abs/10.1002/pssr.201206414.

[116] Thomas Olsen, Erik Andersen, Takuya Okugawa, Daniele Torelli, Thorsten Deilmann, and Kristian S. Thygesen. Discovering two-dimensional topological insulators from high-throughput computations. *Phys. Rev. Materials*, 3: 024005, Feb 2019. doi: 10.1103/PhysRevMaterials.3.024005. URL https://link.aps.org/doi/10.1103/PhysRevMaterials.3.024005.

[117] Taifeng Liu, Xingfan Zhang, Jingcheng Guan, C. Richard A. Catlow, Aron Walsh, Alexey A. Sokol, and John Buckeridge. Insight into the fergusonite–scheelite phase transition of abo4-type oxides by density functional theory: A case study of the subtleties of the ground state of bivo4. *Chemistry of Materials*, 34(12): 5334–5343, 2022. doi: 10.1021/acs.chemmater.1c04417. URL https://doi.org/10.1021/acs.chemmater.1c04417.

[118] Qingsong Zhang, Tahir Cagin, and William A. Goddard. The ferroelectric and cubic phases in batio¡sub¿3¡/sub¿ ferroelectrics are also antiferroelectric. *Proceedings of the National Academy of Sciences*, 103(40):14695–14700, 2006. doi: 10.1073/pnas.0606612103. URL https://www.pnas.org/doi/abs/10.1073/pnas.0606612103.

[119] Eric Bousquet. *First-principles study of ferroelectric oxide nanostructures.* PhD thesis, 01 2008.

[120] Ronald E. Cohen. Origin of ferroelectricity in perovskite oxides. *Nature*, 358 (6382):136–138, July 1992. ISSN 1476-4687. doi: 10.1038/358136a0. URL https://doi.org/10.1038/358136a0.

[121] P. Hohenberg and W. Kohn. Inhomogeneous electron gas. *Phys. Rev.*, 136:

B864–B871, Nov 1964. doi: 10.1103/PhysRev.136.B864. URL https://link.aps.org/doi/10.1103/PhysRev.136.B864.

[122] P. E. Blöchl. Projector augmented-wave method. *Phys. Rev. B*, 50:17953–17979, Dec 1994. doi: 10.1103/PhysRevB.50.17953. URL http://link.aps.org/doi/10.1103/PhysRevB.50.17953.

[123] A. I. Liechtenstein, V. I. Anisimov, and J. Zaanen. Density-functional theory and strong interactions: Orbital ordering in mott-hubbard insulators. *Phys. Rev. B*, 52:R5467–R5470, Aug 1995. doi: 10.1103/PhysRevB.52.R5467. URL http://link.aps.org/doi/10.1103/PhysRevB.52.R5467.

[124] Gopalakrishnan Sai Gautam and Emily A. Carter. Evaluating transition metal oxides within dft-scan and SCAN + u frameworks for solar thermochemical applications. *Phys. Rev. Materials*, 2:095401, Sep 2018. doi: 10.1103/PhysRevMaterials.2.095401. URL https://link.aps.org/doi/10.1103/PhysRevMaterials.2.095401.

[125] I. G. Buda, C. Lane, B. Barbiellini, A. Ruzsinszky, J. Sun, and A. Bansil. Characterization of Thin Film Materials using SCAN meta-GGA, an Accurate Nonempirical Density Functional. *Scientific Reports*, 7(1):44766, March 2017. ISSN 2045-2322. doi: 10.1038/srep44766. URL https://doi.org/10.1038/srep44766.

[126] Bernardo Barbiellini, Aki Pulkkinen, Johannes Nokelainen, Vasiliy Buchelnikov, Vladimir Sokolovskiy, Olga N. Miroshkina, Mikhail Zagrebin, Katarina Pussi, Erkki Lähderanta, and Alexander Granovsky. Correlation effects in the ground state of Ni-(Co)-Mn-Sn Heusler compounds. *MRS Advances*, 4(8): 441–446, February 2019. ISSN 2059-8521. doi: 10.1557/adv.2019.134. URL https://doi.org/10.1557/adv.2019.134.

[127] Hendrik J. Monkhorst and James D. Pack. Special points for brillouin-zone

integrations. *Phys. Rev. B*, 13:5188–5192, Jun 1976. doi: 10.1103/PhysRevB.13.5188. URL https://link.aps.org/doi/10.1103/PhysRevB.13.5188.

[128] D. Hobbs, G. Kresse, and J. Hafner. Fully unconstrained noncollinear magnetism within the projector augmented-wave method. *Phys. Rev. B*, 62:11556–11570, Nov 2000. doi: 10.1103/PhysRevB.62.11556. URL http://link.aps.org/doi/10.1103/PhysRevB.62.11556.

[129] Koichi Momma and Fujio Izumi. *VESTA3* for three-dimensional visualization of crystal, volumetric and morphology data. *Journal of Applied Crystallography*, 44 (6):1272–1276, Dec 2011. doi: 10.1107/S0021889811038970. URL https://doi.org/10.1107/S0021889811038970.

[130] Uthpala Herath, Pedram Tavadze, Xu He, Eric Bousquet, Sobhit Singh, Francisco Muñoz, and Aldo H. Romero. Pyprocar: A python library for electronic structure pre/post-processing. *Computer Physics Communications*, 251:107080, 2020. ISSN 0010-4655. doi: https://doi.org/10.1016/j.cpc.2019.107080. URL http://www.sciencedirect.com/science/article/pii/S0010465519303935.

[131] David Boldrin, Eduardo Mendive-Tapia, Jan Zemen, Julie B. Staunton, Thomas Hansen, Araceli Aznar, Josep-Lluís Tamarit, Maria Barrio, Pol Lloveras, Jiyeob Kim, Xavier Moya, and Lesley F. Cohen. Multisite exchange-enhanced barocaloric response in Mn_3NiN. *Phys. Rev. X*, 8:041035, Nov 2018. doi: 10.1103/PhysRevX.8.041035. URL https://link.aps.org/doi/10.1103/PhysRevX.8.041035.

[132] Xiaodong Zhou, Jan-Philipp Hanke, Wanxiang Feng, Stefan Blügel, Yuriy Mokrousov, and Yugui Yao. Giant anomalous nernst effect in noncollinear antiferromagnetic mn-based antiperovskite nitrides. *Phys. Rev. Materials*, 4:024408, Feb 2020. doi: 10.1103/PhysRevMaterials.4.024408. URL https://link.aps.org/doi/10.1103/PhysRevMaterials.4.024408.

[133] K. Zhao, T. Hajiri, H. Chen, R. Miki, H. Asano, and P. Gegenwart. Anomalous hall effect in the noncollinear antiferromagnetic antiperovskite $mn_3ni_{1-x}cu_xN$. *Phys. Rev. B*, 100:045109, Jul 2019. doi: 10.1103/PhysRevB.100.045109. URL https://link.aps.org/doi/10.1103/PhysRevB.100.045109.

[134] T. Hajiri, K. Matsuura, K. Sonoda, E. Tanaka, K. Ueda, and H. Asano. Spin-orbit-torque switching of noncollinear antiferromagnetic antiperovskite manganese nitride mn_3GaN. *Phys. Rev. Applied*, 16:024003, Aug 2021. doi: 10.1103/PhysRevApplied.16.024003. URL https://link.aps.org/doi/10.1103/PhysRevApplied.16.024003.

[135] Ruihua Chou, Ying Sun, Huiqing Lu, and Guang-Hong Lu. Structure, magnetic properties and thermal expansion of mn3ptnx ($0 \leq x \leq 1.0$) compounds. *International Journal of Modern Physics B*, 32(28):1850314, 2018. doi: 10.1142/S0217979218503149. URL https://doi.org/10.1142/S0217979218503149.

[136] E. Krén, É. Zsoldos, M. Barberon, and R. Fruchart. Magnetic properties of the mn3ptnx system. *Solid State Communications*, 9(1):27–31, 1971. ISSN 0038-1098. doi: https://doi.org/10.1016/0038-1098(71)90046-9. URL https://www.sciencedirect.com/science/article/pii/0038109871900469.

[137] Meimei Wu, Cong Wang, Ying Sun, Lihua Chu, Jun Yan, Dongfeng Chen, Qingzhen Huang, and Jeffrey W. Lynn. Magnetic structure and lattice contraction in mn3nin. *Journal of Applied Physics*, 114(12):123902, 2013. doi: 10.1063/1.4822023. URL https://doi.org/10.1063/1.4822023.

[138] Aliaksandr V. Krukau, Oleg A. Vydrov, Artur F. Izmaylov, and Gustavo E. Scuseria. Influence of the exchange screening parameter on the performance of screened hybrid functionals. *The Journal of Chemical Physics*, 125(22):224106, 2006. doi: 10.1063/1.2404663. URL http://scitation.aip.org/content/aip/journal/jcp/125/22/10.1063/1.2404663.

[139] John P. Perdew, Stefan Kurth, Ale š Zupan, and Peter Blaha. Accurate density functional with correct formal properties: A step beyond the generalized gradient approximation. *Phys. Rev. Lett.*, 82:2544–2547, Mar 1999. doi: 10.1103/PhysRevLett.82.2544. URL https://link.aps.org/doi/10.1103/PhysRevLett.82.2544.

[140] John P. Perdew, Kieron Burke, and Yue Wang. Generalized gradient approximation for the exchange-correlation hole of a many-electron system. *Phys. Rev. B*, 54:16533–16539, Dec 1996. doi: 10.1103/PhysRevB.54.16533. URL https://link.aps.org/doi/10.1103/PhysRevB.54.16533.

[141] K. Kadowaki and S.B. Woods. Universal relationship of the resistivity and specific heat in heavy-fermion compounds. *Solid State Communications*, 58(8):507–509, 1986. ISSN 0038-1098. doi: https://doi.org/10.1016/0038-1098(86)90785-4. URL https://www.sciencedirect.com/science/article/pii/0038109886907854.

[142] J. Hubbard and Brian Hilton Flowers. Electron correlations in narrow energy bands. *Proceedings of the Royal Society of London. Series A. Mathematical and Physical Sciences*, 276(1365):238–257, 1963. doi: 10.1098/rspa.1963.0204. URL https://royalsocietypublishing.org/doi/abs/10.1098/rspa.1963.0204.

[143] Viraht Sahni, K. P. Bohnen, and Manoj K. Harbola. Analysis of the local-density approximation of density-functional theory. *Phys. Rev. A*, 37:1895–1907, Mar 1988. doi: 10.1103/PhysRevA.37.1895. URL https://link.aps.org/doi/10.1103/PhysRevA.37.1895.

[144] J. C. Slater. Atomic shielding constants. *Phys. Rev.*, 36:57–64, Jul 1930. doi: 10.1103/PhysRev.36.57. URL https://link.aps.org/doi/10.1103/PhysRev.36.57.

[145] Artur Born, Fredrik O. L. Johansson, Torsten Leitner, Ieva Bidermane, Danilo Kühn, Nils Mårtensson, and Alexander Föhlisch. The degree of electron itinerancy and shell closing in the core-ionized state of transition metals probed by

auger-photoelectron coincidence spectroscopy. *Phys. Chem. Chem. Phys.*, 24: 19218–19222, 2022. doi: 10.1039/D2CP02477B. URL http://dx.doi.org/10.1039/D2CP02477B.

[146] Naoto Nagaosa, Jairo Sinova, Shigeki Onoda, A. H. MacDonald, and N. P. Ong. Anomalous hall effect. *Rev. Mod. Phys.*, 82:1539–1592, May 2010. doi: 10.1103/RevModPhys.82.1539. URL https://link.aps.org/doi/10.1103/RevModPhys.82.1539.

[147] Ivo Souza, Nicola Marzari, and David Vanderbilt. Maximally localized wannier functions for entangled energy bands. *Phys. Rev. B*, 65:035109, Dec 2001. doi: 10.1103/PhysRevB.65.035109. URL https://link.aps.org/doi/10.1103/PhysRevB.65.035109.

[148] Xinjie Wang, Jonathan R. Yates, Ivo Souza, and David Vanderbilt. Ab initio calculation of the anomalous hall conductivity by wannier interpolation. *Phys. Rev. B*, 74:195118, Nov 2006. doi: 10.1103/PhysRevB.74.195118. URL https://link.aps.org/doi/10.1103/PhysRevB.74.195118.

[149] Matthias Ernzerhof, Kieron Burke, and John P. Perdew. *Density functional theory, the exchange hole, and the molecular bond.* Elsevier, Amsterdam, 1996. URL https://www.elsevier.com/books/recent-developments-and-applications-of-modern-density-functional-theory/seminario/978-0-444-82404-2.

[150] Sihao Deng, Ying Sun, Lei Wang, Zaixing Shi, Hui Wu, Qingzhen Huang, Jun Yan, Kewen Shi, Pengwei Hu, Ali Zaoui, and Cong Wang. Frustrated triangular magnetic structures of mn3znn: Applications in thermal expansion. *The Journal of Physical Chemistry C*, 119(44):24983–24990, 2015. doi: 10.1021/acs.jpcc.5b07225. URL https://doi.org/10.1021/acs.jpcc.5b07225.

[151] Vu Thi Ngoc Huyen, Michi-To Suzuki, Kunihiko Yamauchi, and Tamio Oguchi. Topology analysis for anomalous hall effect in the noncollinear antiferromagnetic

states of mn_3aN (a = Ni, Cu, Zn, Ga, Ge, Pd, In, Sn, Ir, Pt). *Phys. Rev. B*, 100: 094426, Sep 2019. doi: 10.1103/PhysRevB.100.094426. URL https://link.aps.org/doi/10.1103/PhysRevB.100.094426.

[152] Camilo X. Quintela, Kyung Song, Ding-Fu Shao, Lin Xie, Tianxiang Nan, Tula R. Paudel, Neil Campbell, Xiaoqing Pan, Thomas Tybell, Mark S. Rzchowski, Evgeny Y. Tsymbal, Si-Young Choi, and Chang-Beom Eom. Epitaxial antiperovskite/perovskite heterostructures for materials design. *Science Advances*, 6(30):eaba4017, 2020. doi: 10.1126/sciadv.aba4017. URL https://www.science.org/doi/abs/10.1126/sciadv.aba4017.

[153] C. X. Quintela, N. Campbell, D. F. Shao, J. Irwin, D. T. Harris, L. Xie, T. J. Anderson, N. Reiser, X. Q. Pan, E. Y. Tsymbal, M. S. Rzchowski, and C. B. Eom. Epitaxial thin films of dirac semimetal antiperovskite cu3pdn. *APL Materials*, 5 (9):096103, 2017. doi: 10.1063/1.4992006. URL https://doi.org/10.1063/1.4992006.

[154] F. Johnson, D. Boldrin, J. Zemen, D. Pesquera, J. Kim, X. Moya, H. Zhang, H. K. Singh, I. Samathrakis, and L. F. Cohen. Strain dependence of berry-phase-induced anomalous hall effect in the non-collinear antiferromagnet mn3nin. *Applied Physics Letters*, 119(22):222401, 2021. doi: 10.1063/5.0072783. URL https://doi.org/10.1063/5.0072783.

[155] QuanSheng Wu, ShengNan Zhang, Hai-Feng Song, Matthias Troyer, and Alexey A. Soluyanov. Wanniertools: An open-source software package for novel topological materials. *Computer Physics Communications*, 224:405–416, 2018. ISSN 0010-4655. doi: https://doi.org/10.1016/j.cpc.2017.09.033. URL https://www.sciencedirect.com/science/article/pii/S0010465517303442.

[156] Harold T. Stokes and Dorian M. Hatch. *FINDSYM*: program for identifying the space-group symmetry of a crystal. *Journal of Applied Crystallography*, 38(1):

237–238, Feb 2005. doi: 10.1107/S0021889804031528. URL https://doi.org/10.1107/S0021889804031528.

[157] HT Stokes, DM Hatch, and BJ Campbell. Findsym. *ISOTROPY Software Suite, iso. byu. edu*, 2017.

[158] Yuanyuan Na, Cong Wang, Lihua Chu, Lei Ding, Jun Yan, Yafei Xue, Wanfeng Xie, and Xiaolong Chen. Preparation and properties of antiperovskite mn3nin thin film. *Materials Letters*, 65(23):3447–3449, 2011. ISSN 0167-577X. doi: https://doi.org/10.1016/j.matlet.2011.07.085. URL https://www.sciencedirect.com/science/article/pii/S0167577X11008639.

[159] EF Bertaut and D Fruchart. Rotation des moments magnetiques du manganese dans mn3nin. *Intern. J. Magnetism.*, 2:259, 1972.

[160] Fruchart, D., Bertaut, E.F., Sénateur, J.P., and Fruchart, R. Magnetic studies on the metallic perovskite-type compound mn 3snn. *J. Physique Lett.*, 38(1): 21–23, 1977. doi: 10.1051/jphyslet:0197700380102100. URL https://doi.org/10.1051/jphyslet:0197700380102100.

[161] Masahito Mochizuki, Masaya Kobayashi, Reoya Okabe, and Daisuke Yamamoto. Spin model for nontrivial types of magnetic order in inverse-perovskite antiferromagnets. *Phys. Rev. B*, 97:060401, Feb 2018. doi: 10.1103/PhysRevB.97.060401. URL https://link.aps.org/doi/10.1103/PhysRevB.97.060401.

[162] M. Seemann, D. Ködderitzsch, S. Wimmer, and H. Ebert. Symmetry-imposed shape of linear response tensors. *Phys. Rev. B*, 92:155138, Oct 2015. doi: 10.1103/PhysRevB.92.155138. URL https://link.aps.org/doi/10.1103/PhysRevB.92.155138.

[163] J. Zak. Symmetry specification of bands in solids. *Phys. Rev. Lett.*, 45:1025–1028, Sep 1980. doi: 10.1103/PhysRevLett.45.1025. URL https://link.aps.org/doi/10.1103/PhysRevLett.45.1025.

[164] J. Zak. Band representations and symmetry types of bands in solids. *Phys. Rev. B*, 23:2824–2835, Mar 1981. doi: 10.1103/PhysRevB.23.2824. URL https://link.aps.org/doi/10.1103/PhysRevB.23.2824.

[165] Barry Bradlyn, L. Elcoro, Jennifer Cano, M. G. Vergniory, Zhijun Wang, C. Felser, M. I. Aroyo, and B. Andrei Bernevig. Topological quantum chemistry. *Nature*, 547(7663):298–305, July 2017. ISSN 1476-4687. doi: 10.1038/nature23268. URL https://doi.org/10.1038/nature23268.

[166] Mois I. Aroyo, Asen Kirov, Cesar Capillas, J. M. Perez-Mato, and Hans Wondratschek. Bilbao crystallographic server. ii. representations of crystallographic point groups and space groups. *Acta Crystallographica Section A*, 62(2):115–128, 2006. doi: https://doi.org/10.1107/S0108767305040286. URL https://onlinelibrary.wiley.com/doi/abs/10.1107/S0108767305040286.

[167] J. Kübler and C. Felser. Non-collinear antiferromagnets and the anomalous hall effect. *EPL (Europhysics Letters)*, 108(6):67001, dec 2014. doi: 10.1209/0295-5075/108/67001. URL https://doi.org/10.1209/0295-5075/108/67001.

[168] Yugui Yao, Leonard Kleinman, A. H. MacDonald, Jairo Sinova, T. Jungwirth, Ding-sheng Wang, Enge Wang, and Qian Niu. First principles calculation of anomalous hall conductivity in ferromagnetic bcc fe. *Phys. Rev. Lett.*, 92:037204, Jan 2004. doi: 10.1103/PhysRevLett.92.037204. URL https://link.aps.org/doi/10.1103/PhysRevLett.92.037204.

[169] Fernando de Juan, Adolfo G. Grushin, Takahiro Morimoto, and Joel E Moore. Quantized circular photogalvanic effect in Weyl semimetals. *Nature Communications*, 8(1):15995, July 2017. ISSN 2041-1723. doi: 10.1038/ncomms15995. URL https://doi.org/10.1038/ncomms15995.

[170] A. A. Zyuzin, Si Wu, and A. A. Burkov. Weyl semimetal with broken time reversal and inversion symmetries. *Phys. Rev. B*, 85:165110, Apr 2012. doi: 10.1103/

PhysRevB.85.165110. URL https://link.aps.org/doi/10.1103/PhysRevB.85.165110.

[171] Leonhard Sohncke. *Entwickelung einer Theorie der Krystallstruktur*. BG Teubner, 1879.

[172] Massimo Nespolo and Amani Hind Benahsene. Symmetry and chirality in crystals. *Journal of Applied Crystallography*, 54(6):1594–1599, Dec 2021. doi: 10.1107/S1600576721009109. URL https://doi.org/10.1107/S1600576721009109.

[173] Mariette Hellenbrandt. The inorganic crystal structure database (icsd)—present and future. *Crystallography Reviews*, 10(1):17–22, 2004. doi: 10.1080/08893110410001664882. URL https://doi.org/10.1080/08893110410001664882.

[174] Anubhav Jain, Shyue Ping Ong, Geoffroy Hautier, Wei Chen, William Davidson Richards, Stephen Dacek, Shreyas Cholia, Dan Gunter, David Skinner, Gerbrand Ceder, and Kristin A. Persson. Commentary: The materials project: A materials genome approach to accelerating materials innovation. *APL Materials*, 1(1): 011002, 2013. doi: 10.1063/1.4812323. URL https://doi.org/10.1063/1.4812323.

[175] J M Perez-Mato, S V Gallego, L Elcoro, E Tasci, and M I Aroyo. Symmetry conditions for type ii multiferroicity in commensurate magnetic structures. *Journal of Physics: Condensed Matter*, 28(28):286001, may 2016. doi: 10.1088/0953-8984/28/28/286001. URL https://dx.doi.org/10.1088/0953-8984/28/28/286001.

[176] Jonathan Gaudet, Hung-Yu Yang, Santu Baidya, Baozhu Lu, Guangyong Xu, Yang Zhao, Jose A. Rodriguez-Rivera, Christina M. Hoffmann, David E. Graf, Darius H. Torchinsky, Predrag Nikolić, David Vanderbilt, Fazel Tafti, and Collin L. Broholm. Weyl-mediated helical magnetism in NdAlSi. *Nature Ma-*

terials, 20(12):1650–1656, December 2021. ISSN 1476-4660. doi: 10.1038/s41563-021-01062-8. URL https://doi.org/10.1038/s41563-021-01062-8.

[177] Vladimir I Anisimov, F Aryasetiawan, and A I Lichtenstein. First-principles calculations of the electronic structure and spectra of strongly correlated systems: the lda+ u method. *Journal of Physics: Condensed Matter*, 9(4):767, jan 1997. doi: 10.1088/0953-8984/9/4/002. URL https://dx.doi.org/10.1088/0953-8984/9/4/002.

[178] Binghai Yan and Claudia Felser. Topological materials: Weyl semimetals. *Annual Review of Condensed Matter Physics*, 8(1):337–354, 2017. doi: 10.1146/annurev-conmatphys-031016-025458. URL https://doi.org/10.1146/annurev-conmatphys-031016-025458.

[179] O.L Sologub, K Hiebl, and P.S Salamakha. Crystal structure and physical properties of new ternary rpt2b compounds, r=la, pr, nd. *Solid State Communications*, 127(5):379–383, 2003. ISSN 0038-1098. doi: https://doi.org/10.1016/S0038-1098(03)00438-1. URL https://www.sciencedirect.com/science/article/pii/S0038109803004381.

[180] Yoshiki J. Sato, Fuminori Honda, Arvind Maurya, Yusei Shimizu, Ai Nakamura, Yoshiya Homma, Dexin Li, Yoshinori Haga, and Dai Aoki. Single-crystal growth and magnetic phase diagram of the enantiopure crystal of ndpt$_2$B. *Phys. Rev. Materials*, 5:034411, Mar 2021. doi: 10.1103/PhysRevMaterials.5.034411. URL https://link.aps.org/doi/10.1103/PhysRevMaterials.5.034411.

[181] Danel Orobengoa, Cesar Capillas, Mois I. Aroyo, and J. Manuel Perez-Mato. *AMPLIMODES*: symmetry-mode analysis on the Bilbao Crystallographic Server. *Journal of Applied Crystallography*, 42(5):820–833, Oct 2009. doi: 10.1107/S0021889809028064. URL https://doi.org/10.1107/S0021889809028064.

[182] Marilena Ferbinteanu, Alessandro Stroppa, Marco Scarrozza, Ionel Humelnicu, Dan Maftei, Bogdan Frecus, and Fanica Cimpoesu. On the density functional

theory treatment of lanthanide coordination compounds: A comparative study in a series of cu–ln (ln = gd, tb, lu) binuclear complexes. *Inorganic Chemistry*, 56(16):9474–9485, 2017. doi: 10.1021/acs.inorgchem.7b00587. URL https://doi.org/10.1021/acs.inorgchem.7b00587. PMID: 28782949.

[183] Lifang Zhang, Junling Meng, Fen Yao, Xiaojuan Liu, Jian Meng, and Hongjie Zhang. Strong-correlated behavior of 4f electrons and 4f5d hybridization in PrO2. *Scientific Reports*, 8(1):15995, October 2018. ISSN 2045-2322. doi: 10.1038/s41598-018-34336-4. URL https://doi.org/10.1038/s41598-018-34336-4.

[184] David Vanderbilt. *Berry Phases in Electronic Structure Theory: Electric Polarization, Orbital Magnetization and Topological Insulators*. Cambridge University Press, 2018. doi: 10.1017/9781316662205.

[185] Inti Sodemann and Liang Fu. Quantum nonlinear hall effect induced by berry curvature dipole in time-reversal invariant materials. *Phys. Rev. Lett.*, 115:216806, Nov 2015. doi: 10.1103/PhysRevLett.115.216806. URL https://link.aps.org/doi/10.1103/PhysRevLett.115.216806.

[186] Philippe Czaja, Frank Freimuth, Jürgen Weischenberg, Stefan Blügel, and Yuriy Mokrousov. Anomalous hall effect in ferromagnets with gaussian disorder. *Phys. Rev. B*, 89:014411, Jan 2014. doi: 10.1103/PhysRevB.89.014411. URL https://link.aps.org/doi/10.1103/PhysRevB.89.014411.

Publications:

[1] **D. Torres-Amaris**, A. Bautista-Hernandez, R. González-Hernández, Aldo H. Romero, A. C. Garcia-Castro, *Anomalous Hall conductivity control in* Mn_3NiN *antiperovskite by epitaxial strain along the kagome plane*, Phys. Rev. B 106, 195113 (2022).

[2] **D. Torres-Amaris**, R. González-Hernández, A. H. Romero, A. C. Garcia-Castro, *Spin-orbit coupling and Coulomb U correlation effects on the anomalous Hall conductivity in the* Mn_3BN *antiperovskites*, In preparation, (2023).

[3] **D. Torres-Amaris**, R. González-Hernández, A. H. Romero, A. C. Garcia-Castro, *Electronic, magnetic, and topological features of* A_2PtB *(A = La, Nd) chiral symmetry compounds*, In preparation, (2023)

Talks:

[1] **D. Torres-Amaris**, Aldo H. Romero, R. González-Hernández, A. C. Garcia-Castro, *Strain control of the anomalous Hall conductivity in the chiral antiferromagnet* Mn_3NiN *antiperovskite*, E-MRS 2022 Spring Meeting, European Materials Research Society.